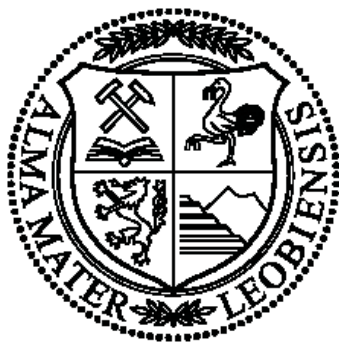# THE GEOTHERMAL WELL ILZ THERMAL 1

Detailed lithological, hydrogeological and geothermal investigations for potential utilization as an alternative source of energy.

WOLFGANG HASENBURGER

MASTER THESIS

Applied Geosciences – Economic and Environmental Geology

Submitted at the Chair of Applied Geophysics of the Montanuniverstaet Leoben.

Supervision:

Ass. Prof. Dipl.-Ing. Dr. mont. Nina Gegenhuber, Chair of Applied Geophysics, Montanuniversitaet Leoben

Hon. Prof. Dr. rer. Nat. habil. Jürgen Schön, Chair of Applied Geophysics, Montanuniversitaet Leoben

Univ.-Prof. Dr. Johann Goldbrunner, Geoteam Ges.m.b.H., Graz

Eidesstattliche Erklärung

Ich erkläre an Eides statt, dass ich diese Arbeit selbständig verfasst, andere als die angegebenen Quellen und Hilfsmittel nicht benutzt und mich auch sonst keiner unerlaubten Hilfsmittel bedient habe.

Affidavit

I declare in lieu of oath, that I wrote this thesis and performed the associated research myself, using only literature cited in this volume.

_____   _____

       Date   Signature

Acknowledgements

2

I LOVE YOU.

Abstract

The well ILZ Thermal 1 was drilled in the year 1998 to a final depth of 1,906.0 m. Located about 15 km west of the town of Fürstenfeld in the Eastern Styrian Neogene Basin, it perforated Miocene sediments until 1,466.0 m comprising Lower Pannonian to Karpatian sequences. Those are underlain by dolomites of the Graz Paleozoic until 1,906.0 m comprising the basement

Formations were investigated regarding their reservoir characteristics including lithological, hydrogeological and geothermal parameters to define the geothermal system in the area of the well. A focus thereby lies on the Paleozoic basement not only because of highest data density from well logs and cuttings but also because of highest expectable temperatures for geothermal energy utilization.

Lower Pannonian and Sarmatian sediments consist of an interlayering of gravels and sands to fine-grained deposits. The Lower Pannonian can be correlated regionally with the "Feldbach-Formation", whereas the Upper Sarmatian corresponds to the "Gleisdorf-Formation". Lower to Middle Sarmatian sediments might be correlated with the "Rollsdorf-" or "Grafendorf-Formation". Major potential aquifers for drinking water supply are formed by several coarse developed horizons, making up a total aquifer net thickness of 153.8 m with an average resistivity-derived porosity of around 20%.

The Badenian series starts with the much finer developed "Bulimina-Bolivina/Rotalia-Cibicides Zone" (BB/RC-Zone). Below, the "Sandschaler Zone" is dominated by coarse sandstones with few shaly to marly intercalations and hence presents major potential for geothermal utilization with temperatures of up to 46.5°C, calculated from a geothermal gradient of 45.5°C/km. Porosities range between 22-25% and transmissivity was calculated to $3.15*10^{-6}$ m²/s. The water of the Sandschaler Zone is a sodium-bicarbonate type with a content of total dissolved solids (TDS) of 5.01 g/l.

The Sandschaler Zone is underlain by the Lower Badenian Lageniden Zone, consisting of the upper fine and impermeable "Tonmergel Series" and the lower much coarser developed Base Conglomerate, which forms, together with the Karpatian Conglomerate-rich Group, the second important geothermal aquifer. Those are characterized by a more or less very homogeneous very coarse conglomeratic development with minor thin shaly and marly intercalations. However, porosities range between 11-15% and transmissivity was determined to $6.61*10^{-5}$ m²/s. The water is typed as a sodium-chloride-bicarbonate water with very high mineralization of 17.9 g/l. This, together with very high CO_2- and [226]Ra-content might cause problems when extracted and for utilization, especially in balneology, unless treated requiring additional costs. Temperatures reach 76.5°C at 1,466.0 m.

Finally, the basement is formed by dolomites of the Graz Paleozoic and can be subdivided into three major zones. The upper light to dark gray dolomites and marls (1) are assigned to the "Flösserkogel" Formation of the "Rannach" Facies (Lower to Middle Devonian) and are developed very heterogeneously. Major geothermal potential lies in the uppermost part and around 1,600 m with permeabilities of > 100 mD and 60 mD, respectively. Temperatures gain 76-83°C, but again a very high water mineralization (TDS = 17.6 g/l) and high CO_2- and [226]Ra-content might lead to problems. The Paleozoic water itself was classified as sodium-bicarbonate type.

The lower dark gray dolomites (3) show a very homogeneous development with abundance of breccias increasing towards depth and therefore can be assigned to the Schöckl Facies through correlation with the lower dolomites of the well Arnwiesen 1. Although temperatures reach 96.5°C at the final depth, those dolomites are not regarded as potential aquifers due to permeabilities of < 50 mD. The upper and the lower zone are separated by a fault zone (2), which represents the major structure for convective heat transport in the geothermal system with a permeability of > 260 mD.

All in all, geothermal resources can be classified as low enthalpy resources and total heat in place was calculated to nearly 10^{10} MJ or $2.8*10^9$ kWh. The temperature range would allow application in agriculture (e.g. green houses), domestic hot water supply, balneology, radiators, for example.

Zusammenfassung

Die Tiefbohrung ILZ Thermal 1 wurde im Jahr 1998 bis auf eine Endtiefe von 1,906.0 m niedergebracht. Sie befindet sich in der Marktgemeinde Ilz, ca. 15 km westlich der Stadt Fürstenfeld im Oststeirischen Neogenbecken. Dabei wurden miozäne Sedimente von Unterpannon bis Karpat durchbohrt, welche von Dolomiten des Grazer Paläozoikums unterlagert werden.

Alle Formationen wurden hinsichtlich ihrer Reservoireigenschaften untersucht. Dabei wurden detaillierte lithologische, hydrogeologische und geothermische Analysen durchgeführt um Aussagen über die Nutzbarkeit der Thermalwässer als alternative Energiequelle treffen zu können.

Die unterpannonischen und sarmatischen Ablagerungen werden von einer Wechsellagerung von Sanden und Kiesen und feinkörnigen Ablagerungen aufgebaut. Das Unterpannon kann aus regional-geologischen Überlegungen der „Feldbach-Formation", das Obersarmat der „Gleisdorf-Formation" zugeordnet werden. Das Unter- bis Mittelsarmat entspricht eventuell der „Rollsdorf-" oder „Grafendorf-Formation". Sand- und Kieshorizonte mit einer gesamten Nettomächtigkeit von 153.8 m und einer durchschnittlichen Widerstandsporosität von 20% bilden die vielversprechendsten Horizonte für eine potenzielle Trinkwassererschließung.

Das Baden beginnt mit der sehr feinkörnig entwickelten Bulimina-Bolivina/Rotalia-Cibicides Zone. Die darunterliegende Sandschalerzone wird von Grobsandsteinen mit wenigen feinkörnigen Ein-schaltungen dominiert und bildet deshalb eine Zone geothermischen Potenzials. Die Temperaturen erreichen 46.5°C, resultierend aus einem berechneten geothermischen Gradienten von 45.5°C/km. Die Porosität liegt bei 22-25% mit einer Transmissivität von $3.15*10^{-6}$ m²/s. Das Thermalwasser wurde als Natrium-Hydrogenkarbonat-Typ mit einer Summe an gelösten Stoffen von 5.01 g/l klassifiziert.

Die Sandschalerzone wird von der unterbadenischen Lagenidenzone unterlagert, bestehend aus der feinkörnigen Tonmergelserie und dem grobkörnien Basiskonglomerat, welches zusammen mit der darunterliegenden karpatischen konglomeratreichen Serie einen zweiten geothermischen Aquifer bildet. Die Porosität variiert zwischen 11-15% mit einer Transmissivität von $6.61*10^{-5}$ m²/s. Temperaturen erreichen max. 76.5°C. Das Thermalwasser wurde als Natrium-Chlorid-Hydrogen-karbonat-Typ klassifiziert mit einer Summe an gelösten Stoffen von 17.9 g/l. Die sehr hohe Mineralisierung und ein sehr hoher CO_2- und [226]Ra-Gehalt würden Probleme bei der Förderung und Nutzung darstellen und zusätzliche teure und technisch aufwendige Maßnahmen erfordern.

Das Grundgebirge wird von Dolomiten des Grazer Paläozoikums aufgebaut, wobei dieses in der Bohrung in drei Zonen gegliedert werden kann. Die Hangendfolge (1) wird von hell- bis dunkelgrauen Dolomiten und Mergeln gebildet und wird der Flösserkogel Formation der Rannach Fazies zugeordnet (Unter- bis Mitteldevon). Das größte geothermische Potenzial liegt dabei im hangendsten Bereich und um 1,600 m mit Permeabilitäten > 100 mD bzw. 60 mD. Die Temperatur liegt bei 76-83°C, wobei jedoch eine sehr hohe Gesamtmineralisierung von 17.6 g/l und ein sehr hoher CO_2- und [226]Ra-Gehalt des Natrium-Hydrogenkarbonat Wassers voraussichtlich dieselben Probleme verursachen würden.

Die Liegendfolge (3) wird von homogenen dunklengrauen, grobkörnigen Dolomiten gebildet, wobei der Anteil an brekziösen Komponenten zur Endteufe zunimmt. Diese werden der Schöckl Fazies zugeordnet, basierend auf einer Korrelation mit Dolomiten der Bohrung Arnwiesen 1. Obwohl Temperaturen von bis zu 96.5°C bei Endteufe erreicht werden, werden diese Dolomite aufgrund niedriger Pemeabilitäten nicht als potenzielle Aquifere angesehen. Die Hangend- und die Liegendfolge werden von einer Störungszone (2) getrennt, welche mit einer Permeabilität von > 260 mD die Hauptstruktur für konvektiven Wärmefluss in diesem geothermischen System bildet.

Die geothermischen Reserven werden als Niedrig-Enthalpie-Reserven klassifiziert mit einem Gesamt-wärmeinhalt von ca. 10^{10} MJ bzw. $2.8*10^9$ kWh. Die Temperaturbereiche würden eine theoretische Nutzung z.B. im Bereich der Landwirtschaft, Warmwasserversorgung, Balneologie, Heizung erlauben.

Table of contents

1   Introduction

In times of climate change and energy revolution, geothermal energy plays an essential role as emission-poor, alternative form of energy. Geothermal energy generally extracts the heat stored in the Earth's interior over the medium water and heat is available in large amounts ($12.6*10^{26}$ MJ after Armstead, 1983). Geothermal energy is also accounted as renewable, especially when the water is reinjected into the subsurface. Another essential advantage is, that geothermal energy practically is available everywhere shallower or deeper depending mainly on the geotectonic position and subsequent geothermal gradient, respectively. Major fields of applications are for example electricity production, space and district heating, agricultural purposes or balneology.

Geothermal energy is used by human kind since thousands of years especially as hot waters for cooking, heating or probably most prominent as curative waters for recreation in spas of the Roman Empire, in the Far East (China, Japan, Tibet), Turkey, Native Americans, etc. First scientific background for geothermal energy was discovered by Agricola (1556), who observed a temperature increase with depth in mines and the first geothermal gradient was measured in 1791 by Alexander von Humboldt in a mine in Freiberg, Germany with 3.8°C per 100 m (Stober & Bucher, 2012).

Industrial utilization of geothermal energy started in 1827 in Larderello, Italy, where Francesco Larderel used the energy for extraction of Boron and for operation of pumps and machines. In 1913 the first power plant with an electrical potential of 250 kW was installed and with development of deeper wells, dry steam with 200°C was used for electricity production. In 1939, the potential already gained 66 MW. In the first half of the 20th century lots of other countries followed Italy and also started with utilization of geothermal energy for different purposes, e.g. USA, Iceland, New Zealand, Mexiko (Stober & Bucher, 2012).

Today, referring to data from the World Geothermal Congress 2015 in Melbourne, Australia, the total installed capacity increased to over 12,000 MW worldwide in terms of electricity production (Bertrani, 2015) and over 70,000 MW for direct utilization (Lund & Boyd, 2015).

Geothermal energy in Austria is mainly used for balneology, especially in the Eastern Styrian Basin, where utilization of geothermal energy started in the 1970s from abandoned oil exploration wells. 2.2 GWh of electricity and about 1,800 GWh for direct purposes were produced in 2015 in Austria (Goldbrunner, 2015). Most prominent examples are Bad Blumau, Bad Waltersdorf or Bad Radkersburg amongst others.

Therefore, the community of Ilz also decided to realize a geothermal project in the 1990s with the main purpose of perforating the dolomitic basement and using those deep geothermal resources for in balneology and agriculture. Due to very high mineralization, CO_2- and ^{226}Ra-content of those waters, which would have led to problems in production and utilization, shallower and subsequently cooler horizons were opened (Goldbrunner et al., 2000). Finally, the project was abandoned due to lack of financial resources.

As a consequence, within this thesis geophysical logging data are reanalyzed with state of the art software solutions and to investigate the waters using methods commonly applied in geothermal energy exploration. Additionally, sediment-petrographic methods (optical microscopy, X-ray diffraction) are used for more detailed lithological descriptions of the basement dolomites. From that, the main objective of this thesis is the investigation of geological and geothermal parameters for potential utilization of those resources and possibly to revive the project. A further aim should be to address directly to responsibilities of the region for even starting explorations for new projects and subsequently promoting the utilization of geothermal energy as a renewable, alternative energy.

In the first chapter, a general introduction to the state of the art of geothermal energy is given including characterization of a geothermal system and their occurrences regarding geotectonic position.

Furthermore, methods for classification of geothermal systems and subsequent fields of applications are treated. Finally, actual numbers and statistics regarding geothermal use worldwide, economic and environmental considerations are given leading to a short overview of geothermal energy utilization in Austria, focusing on the Styrian Neogene Basin.

The second chapter represents a geological overview of the Styrian Neogene Basin comprising tectonic evolution of the basin and lithological and structural characterization of the basement and the Neogene sedimentary infill resulting in a model of basin development presented in literature as it is assumed today.

The third chapter gives a short introduction to the well ILZ Thermal 1 with geographic location, some historical remarks, drilling and completion data. Methodology used for investigations within this thesis finalizes this chapter.

The main part presents all results gained during investigations. The chapter is split into three major parts according to the characteristics defining a geothermal system: Detailed lithological/structural, geothermal and hydrogeological/-geochemical investigations were carried out and results are presented separately. Finally, in the last chapter those results are interpreted and correlated to define the geothermal system of Ilz, to introduce the well into regional geology and to give an overview of most promising sections for geothermal production.

2 Geothermal Energy – State of the Art

This first chapter represents a short introduction to the state of the art of geothermal energy including the characterization of a geothermal system and its components and their occurrences in different geodynamic settings. Furthermore, different classifications of geothermal systems with subsequent economic uses are given leading to some economic and environmental facts and finishing with specific worldwide and central European (especially Austria) uses of geothermal energy.

2.1 Characterization of a Geothermal System

Geothermal systems generally occur everywhere in the Earth's subsurface within different geodynamic settings and therefore can be defined by various combinations of geological, physical and chemical characteristics, creating a variety of different systems (Dickson & Fanelli, 2004). Most favorable zones for geothermal use are zones with high temperature resources such as active or geologically young volcanic zones (Duffield & Sass, 2003) e.g. Pacific "Ring of Fire", Iceland or African rift system. A further definition was given by Hochstein (1990) who described a geothermal system as "convecting water in the upper crust of the Earth, which, in a confined space, transfers heat from a heat source to a heat sink, usually the free surface."

In general, a geothermal system consists of 3 main characteristics (Fig. 2.1; Dickson & Fanelli, 2004):

1. Heat source
2. Reservoir
3. Fluid/Water
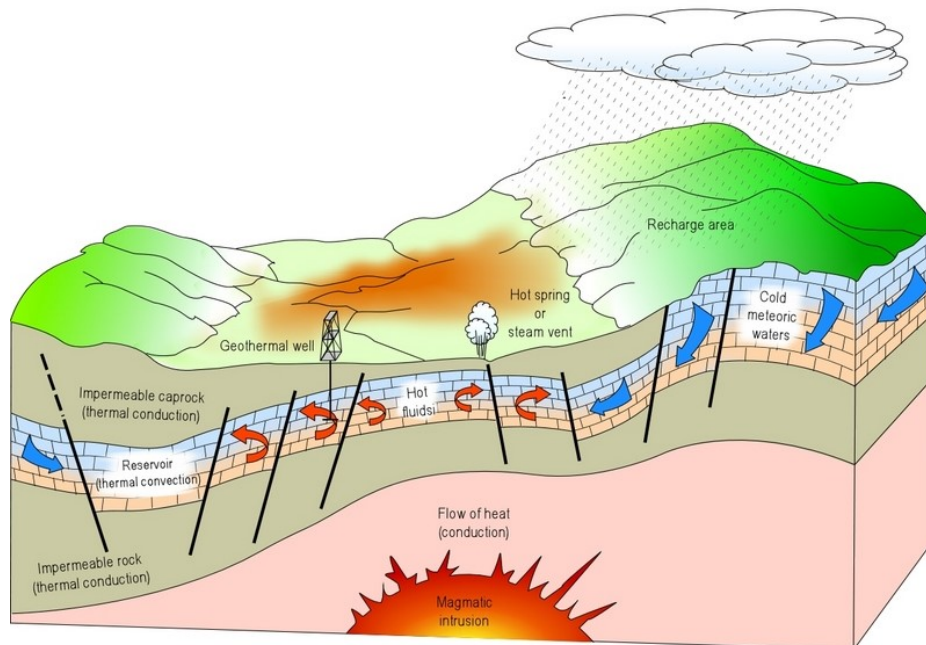
Fig. 2.1: Schematic model of an ideal geothermal system. (Dickson & Fanelli, 2004)

2.1.1 The Thermal Regime of the Earth

Geothermal energy has its origin in the heat produced naturally in the Earth's interior, whereas two principal sources of heat production can be distinguished:

a)   *Residual heat from the Earth's formation*

This type of heat is derived from the fact, that temperatures rise with depth increasing to around 5000 K in the Earth's core in about 6370 km depth (Fig. 2.2; Dziewonski & Anderson, 1981). This residual heat is, with a mean surface temperature of 14°C, continuously transported from inside the Earth to the surface and further to space resulting in a slow but steady cooling of the Earth e.g. cooling of the mantle by 300-350°C within 3 billions of years (Stober & Bucher, 2012).
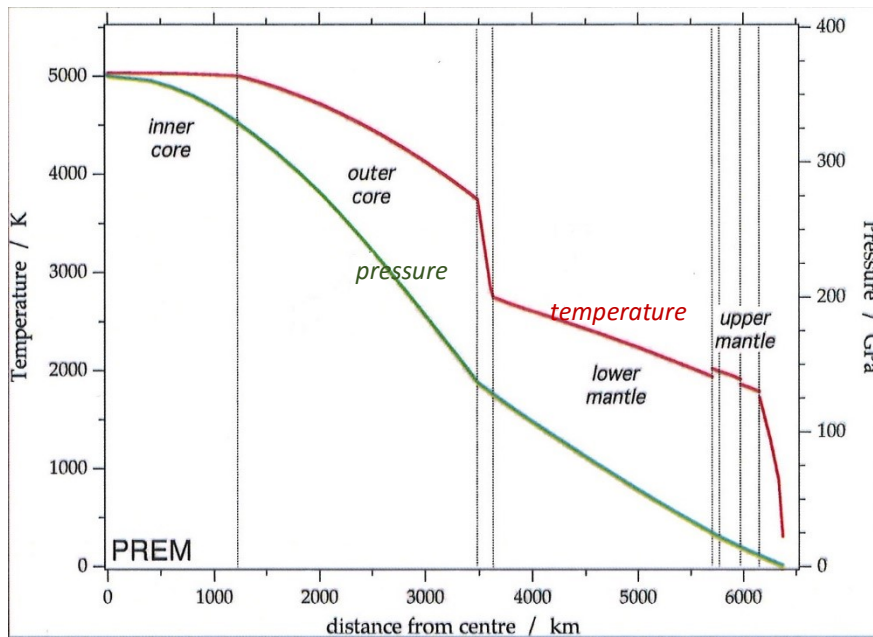
Fig. 2.2: Temperature and pressure distribution in the Earth's interior. (Dziewonski & Anderson, 1981)

The heat flux expressed as the potential per square meter irradiated from the surface has a mean value of about 87 mW/m² but ranging from between 65 mW/m² on continents and 101 mW/m² in oceans (Pollack et al., 1993).

The geothermal gradient, i.e. the increase of temperature with depth, is given with an average value of 25-30°C/km in continental crust (Stober & Bucher, 2012).

b)   *Radiogenic heat production*

Heat is also produced especially in the continental crust due to the decay of the radiogenic elements potassium (^{40}K), uranium (^{238}U, ^{235}U) and thorium (^{232}Th) which contribute about 50% to the total heat flux of 42 TW (Stacey & Loper, 1988) on the Earth's surface. The other 50% are derived from the Earth's interior. (Vacquier, 1991; Turcotte & Schubert, 2002)

This radiogenic heat production depends on the composition of the crust i.e. is higher in felsic rocks (e.g. granite) and is much lower in mafic rocks (e.g. gabbro) and hence can vary greatly along the crust (Stober & Bucher, 2012).

Combining both heat sources, the total heat flux on the surface consists of a more or less constant contribution from the core and mantle and a varying contribution from the crust (Stober and Bucher, 2012). A value for the total heat content of the Earth was given by Armstead (1983) with $12.6*10^{24}$ MJ.

Heat sources for geothermal systems hence can be represented either by this "normal" temperature increase with depth especially in low-temperature areas or by a shallow magmatic intrusion creating an anomalously high geothermal gradient (Dickson & Fanelli, 2004).

Heat transport and thermal properties of rocks

Heat can be transported by either a) convection i.e. with a mass flow (magma, water) through structures (faults, fractures, etc.) or b) by conduction through the rock (Fig. 2.1). This rock specific thermal conductivity λ is together with the radiogenic heat production rate and the specific heat capacity c one essential parameter to be analyzed in geothermal studies. The specific heat capacity is defined as the ability of rocks to store heat per mass unit or in other words how much energy is needed to heat up 1 kg of the specific material by 1 K (Stober & Bucher, 2012).

2.1.2 Reservoir Characterization

A geothermal reservoir is a lithology were the thermal waters can circulate and are stored, whereas the striking parameters determining reservoir quality are effective rock porosity and permeability. The greater the effective porosity and subsequent permeability, the higher is the possible production rate of water and further energy (Duffield & Sass, 2003).

Hence, a geothermal reservoir can be characterized by two main features determining reservoir quality: a) The lithology itself and b) its pore volume/permeability and structures permitting fluid flow.

Major reservoir lithology types are siliciclastic (sandstones) and carbonate (limestone or dolomite) sedimentary rocks whereas the type of lithology itself also has a great influence in pore space structure and distribution. Additionally, metamorphic and igneous rocks, in a minor role, also can represent good reservoirs according to their jointing and other potential cavities.

Siliciclastic rocks

Unconsolidated siliciclastic sediments are classified into clay, silt, sand and gravel by grain size. Generally, they show a well-defined intergranular porosity and hence the fluid flow can be described as laminar but is strongly dependent on clay content and grain sorting (Hölting & Coldewey, 2013).
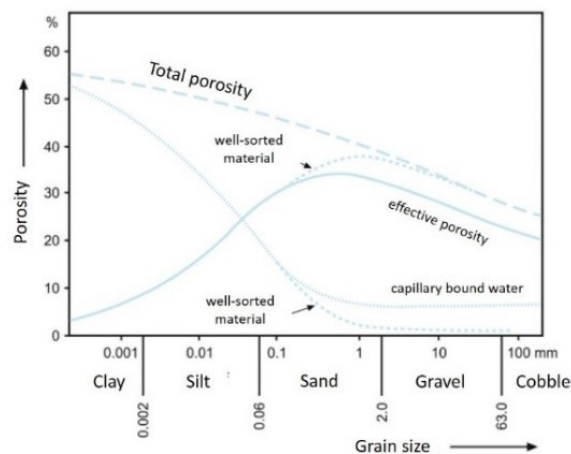

Fig. 2.3: Classification of sediments by grain size and resulting trends for intergranular porosity. (Modified after Hölting & Coldewey, 2013)

The general trends are as shown in Fig. 2.3:

- Total porosity decreases with increasing grain size but most of the pores in clays are occupied by irreducible capillary- or clay-bound water, hence effective porosity is very low
- Effective porosity/permeability increases with decreasing clay content
- Effective porosity/permeability increases with better grain sorting resulting in increasing pore throat radii.

As a conclusion, it can be said that well-sorted sandstones like eolian sands represent a perfect reservoir rock, whereas shales or siltstones due to their low permeability often act as impermeable beds covering or underlying the reservoir (Fig. 2.1; Dickson & Fanelli, 2004).

Carbonate rocks

Carbonate rocks in terms of reservoir rocks include limestones and dolomites and are very sensitive to chemical processes e.g. carstification, dolomitization, dissolution, leaching, etc. which create secondary porosity and hence a very complex and irregular pore and/or fracture system leading to turbulent fluid flow conditions (Tab. 2.1; Lucia, 1999).

Carbonate pore types		
Intergranular Intercrystalline	Moldic Intrafossil Shelter	Cavernous Fracture Solution-enlarged fracture

Tab. 2.1: Petrophysical classification of carbonate pore types. (Adapted from Lucia, 1999)

Those secondary structures are the striking hydraulic spaces for permitting fluid flow in carbonates but also in crystalline rocks, respectively (Hölting & Coldewey, 2013). Similar to siliciclastic rocks, the decisive criterion in terms of reservoir quality is, if the structures are connected to each other and hence contribute to effective porosity and further permeability (Lucia, 1999).

2.1.3 Water Characterization and Fluid Flow

Water in liquid or vapour phase depending on temperature and pressure is the main medium which transfers the heat through convection within a geothermal system. For providing such a convection, not only pore spaces as mentioned under section 2.1.2 but also large-scale structures (e.g. faults) are necessary for connecting a confined reservoir with the surface or with deeper areas. Faults generally act as pathways for meteoric waters which infiltrate from the surface (point A in Fig. 2.4) for recharging the reservoir naturally (B) where the waters are heated up (C), ascend along other faults due to decreased density (upflow area, D) and finally discharge again on the surface as hot springs, geysers, etc. (outflow area, E; Fig. 2.4; Dickson & Fanelli, 2004).
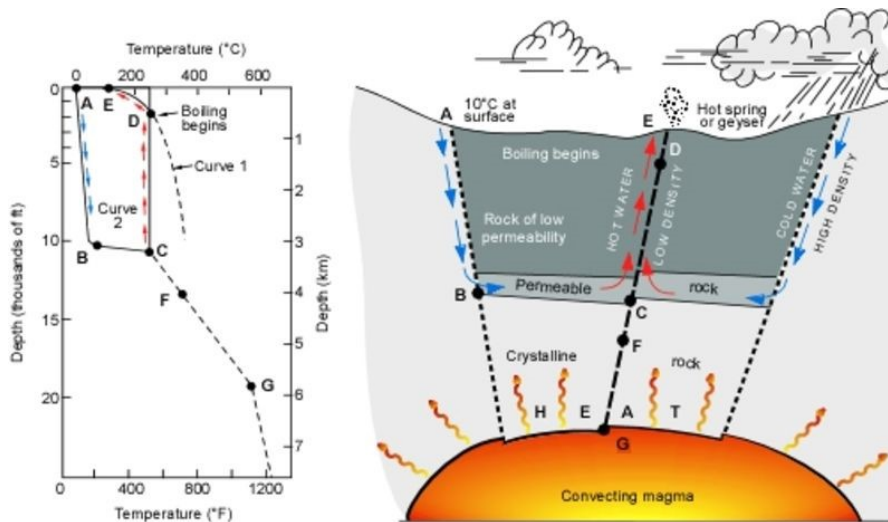
Fig. 2.4: Left: Boiling curve of water (Curve 1) and temperature profile along a typical water circulation route in a geothermal system (Curve 2). Right: Schematic cross-section through a geothermal system showing regional faults acting as pathways for fluid flow (Dickson & Fanelli, 2004).

Water characterization

1. Origin of water – Isotope hydrology

Beside meteoric water (and sea water), which is generally dominating in geothermal systems (Dickson & Fanelli, 2004), water can also have a magmatic (= "juvenile water") origin as well as can be liberated by diagenetic processes and/or metamorphic reactions. Latter ones, together with water bound in mineral structures (e.g. micas or amphiboles) usually do not play a significant role in geothermal systems. For classifying waters in terms of origin and history, isotopic analyses are executed. In the water molecule (H_2O) the most important stable hydrogen isotopes are ^1H and ^2H or D (Deuterium) and for oxygen ^{16}O and ^{18}O.

In isotopic studies, ratios of these isotopes are analyzed because that gives information about the history and origin of the water, e.g. the D isotope is slightly heavier than the ^1H so when water evaporates, the molecules with the lighter isotopes are preferred whereas the heavier ones are enriched in the reservoir (sea, lake, etc.). Processes like this, known as "isotope fractionation" occur at all phase transitions and are strongly temperature dependent (Hölting & Coldewey, 2013). Hence, the isotopic ratios δD and $δ^{18}O$ can be used to classify waters due to their origin (Fig. 2.5):

Fig. 2.5: δD/$δ^{18}O$-values for classification of waters of different origin (Taylor, 1967).

The δD/δ^{18}O – values are calculated from the ratios of the isotopic composition of a water sample which can be measured by simple mass spectrometry (Hölting & Coldewey, 2013):

$$\delta D = \frac{(^{D}/_{^{1}H})_{sample} - (^{D}/_{^{1}H})_{VSMOW}}{(^{D}/_{^{1}H})_{VSMOW}}$$
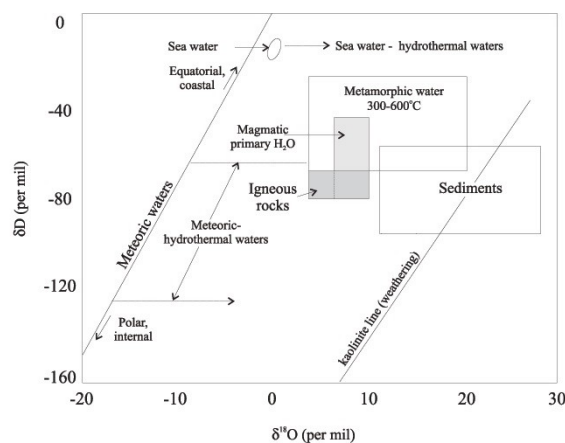
$$\delta^{18}O = \frac{(^{18}O/_{^{16}O})_{sample} - (^{18}O/_{^{16}O})_{VSMOW}}{(^{18}O/_{^{16}O})_{VSMOW}}$$

As already visible from equations 4 and 5, the measured isotopic composition of a sample is compared to an international standard value which is the isotopic composition of sea water (VSMOW = Vienna Standard Mean Ocean Water). Therefore, the VSMOW plots at 0/0 in the isotope diagram (Fig. 2.5). The composition of meteoric waters (rain water) strongly depends on temperature and latitude where they are formed and the fractionation processes affect hydrogen and oxygen analogously resulting in a linear relation between δD and δ^{18}O, the so-called "meteoric water line" (MWL; Hölting & Coldewey, 2013).

$$\delta D = 8 * \delta^{18}O + 10$$

Hydrothermal or in general thermal waters generally plot on the right side of the MWL reflecting an oxygen isotope exchange between bicarbonate dissolved in the water and host rock (Fig. 2.6; Hölting & Coldewey, 2013).
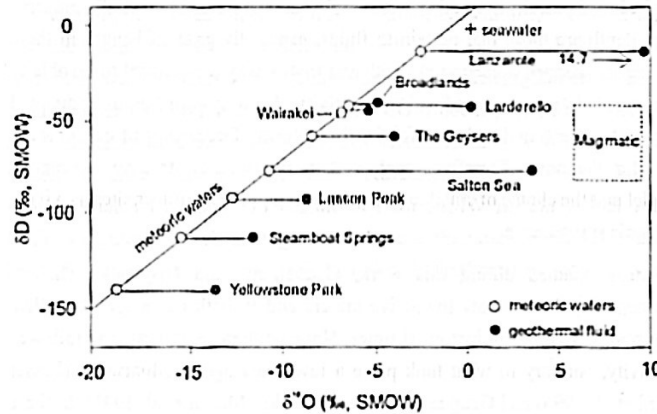
Fig. 2.6: Oxygen isotope exchange of some geothermal waters relative to the MWL (Marini, 2000; after data from Craig, 1963)

2. *Water classification and composition*

Thermal waters are in most cases highly mineralized waters due to water-rock interactions. The solubility of minerals is strongly affected by temperature, pressure, pH-value, redox potential and other species dissolved in the water. Therefore, specific minerals precipitate or dissolve when exposed to specific conditions. This can be used to reconstruct the environment in a deep geothermal system. Dissolved minerals occur in water as cations and anions which gives the water the ability to conduct electricity (electrical conductivity in S/m) depending on temperature and electrical conductivity of the ions (ion charge). The total amount of cations and anions dissolved in a water is known as *"Total Dissolved Solids"* or *TDS* given in mg/l or mg/kg (Stober & Bucher, 2012).

Major solutes are sodium (Na^+), potassium (K^+), calcium (Ca^{2+}), magnesium (Mg^{2+}) and ammonium (NH_4^+) amongst others for cations and chlorine (Cl^-), (bi-)carbonate (CO_3^{2-}, HCO_3^- or H_2CO_3) and sulfate (SO_4^{2-}) amongst others for anions, respectively. Eventually, waters are classified based on their ionic composition.

Because of temperature dependence of dissolution/precipitation, reactive constituents (= species that participate in water-rock reactions) dissolved in the water or on the other side mineral precipitates stable in a specific range of temperature (Fig. 2.7; Reyes, 1990) can be used as geothermometers, i.e. to estimate the temperature in a reservoir if no measurements are available (Stober & Bucher, 2012).
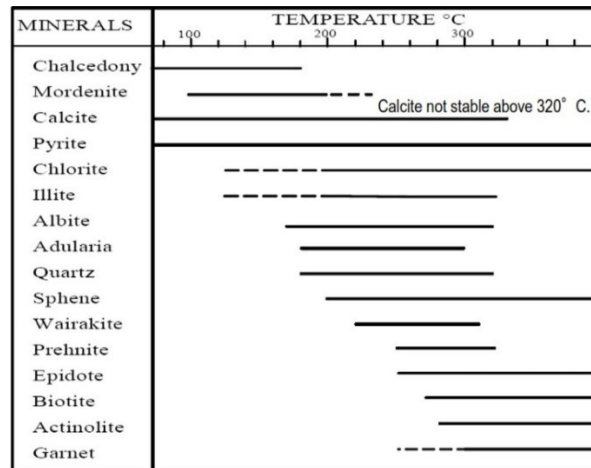
Fig. 2.7: Some hydrothermal alteration minerals commonly used as geothermometers and their temperature stability ranges (Reyes, 1990).

Generally, solubility of monovalent cations is directly proportional to temperature (e.g. halite), whereas solubility of bivalent cations is inversely proportional (e.g. anhydrite, $CaSO_4$; Aguilera, 2014). Basic requirements for the application of geothermometers are a) the assumption that the water resided for a long time in the subsurface, b) thermal equilibrium between water and rock or c) no mixing with surface waters i.e. closed system (Stober & Bucher, 2012; Fournier et al., 1974).

Gases and other constituents

In addition to minerals, gases (e.g. H_2, H_2S, CH_4, CO_2) also act as reactive constituents and hence can also be dissolved in water. Gas solubility (λ) depends on the properties of the gas itself, on water temperature, on TDS and the partial pressure (p) of the gas and can be described by the Henri-Dalton-Equation (Stober & Bucher, 2012):

$$\lambda = K' * p$$

where K' is a temperature-dependent proportionality factor.

At last, inert or non-reactive constituents or tracers such as He, Ar, N_2, Cl, B, Rb, Cs amongst others do not participate in water-rock interactions and therefore indicate possible origin of waters (Aguilera, 2014).

In summary, dissolution of species can give the water properties completely different from those of pure water and to know about those properties but also about behavior of water in a geothermal production process, the analysis and knowledge of dissolved species is inevitable.

2.2   Global Occurrences of Geothermal Systems

Geothermal systems generally occur everywhere in the Earth's subsurface, but most preferred systems for exploitation are those where high temperatures occur in shallow crustal areas, i.e. zones with an anomalously high geothermal gradient. Such zones are recent or young active volcanic zones (e.g. "Pacific Ring of Fire") over subduction zones, spreading/rifting zones (e.g. Iceland, African Rift System) or Hot Spot settings (e.g. Hawaii, Iceland).

Fig. 2.8 shows a map of the Earth's lithospheric plates and locations of active volcanic zones where high temperature resources can be expected and that subsequently the most important geothermal systems occur along plate boundaries (Dickson & Fanelli, 2004).
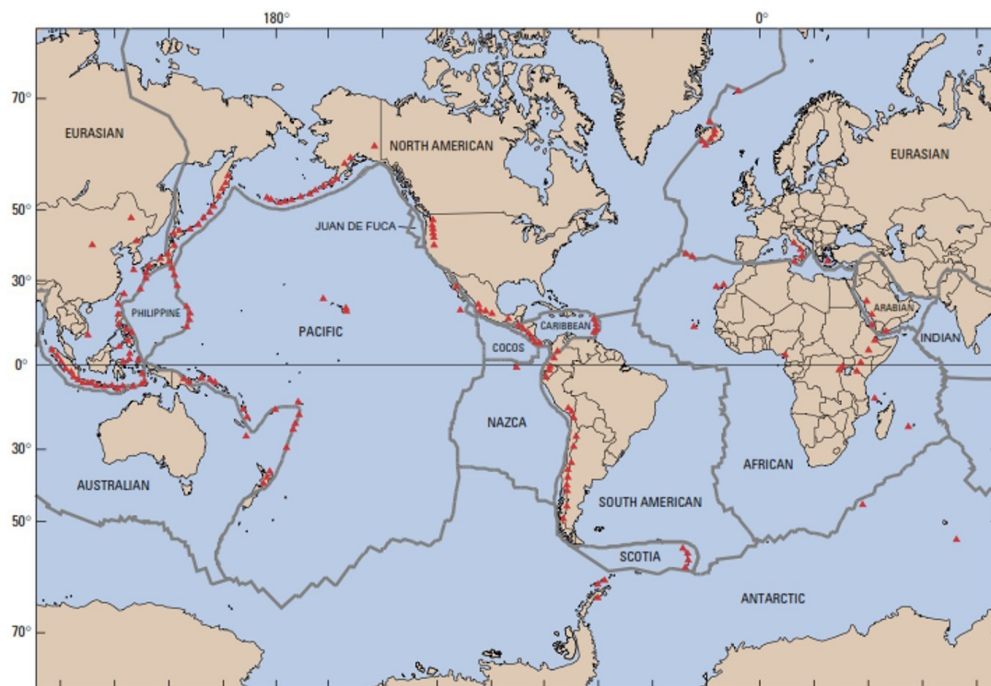
Fig. 2.8: Map showing Earth's main lithospheric plates with recent active volcanic zones (red triangles) in different geodynamic settings coinciding with high temperature resources (Duffield & Sass, 2003).

Apart from those zones, low temperature geothermal systems also occur within plates far away from active volcanic zones. Those are simply based on a normal to slightly raised geothermal gradient and low to medium temperature resources occur in deep crustal regions, e.g. Central Europe.

2.3   Classification of Geothermal Systems

Geothermal systems can be classified according to three different criterions, whereas the most common one is the classification after heat content or enthalpy (Dickson & Fanelli, 2004). The other two criterions are a) after economic feasibility based on the definitions for geothermal resources and reserves and b) after the dominating fluid phase within the system i.e. water, steam or even lack of a fluid.

2.3.1 Classification after Economic Feasibility

Muffler & Cataldi (1978) defined a geothermal resource as "…that part of the accessible resource base that could be extracted economically and legally at some specified time in the future." This simply means all the heat stored in the Earth's subsurface until a specific depth that possibly can be extracted. On the other hand, a geothermal reserve or "identified geothermal resource", according to Dickson & Fanelli (2004), is "that part of the resource of a given area that can be extracted legally at a cost competitive with other commercial energy sources and that are known and characterised by drilling or by geochemical, geophysical and geological evidence."
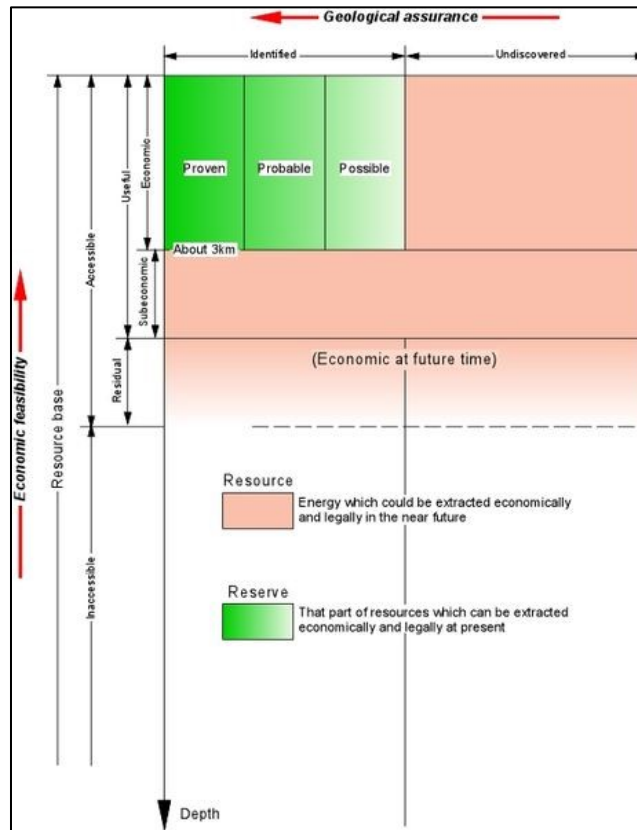
Fig. 2.9: Definition of geothermal resources and reserves and classification of geothermal resources according to economic feasibility and geological assurance (from Muffler & Cataldi, 1978).

Fig. 2.9 illustrates the definitions of geothermal resources and reserves and classifies them according to economic feasibility and geological assurance. It shows that economic feasibility is inversely proportional to the depth of a resource and that the limit between an economic reserve and a "subeconomic" resource generally lies at about 3 km. Deeper resources might be economic in future with the development of new, cheaper technologies in exploration and especially production.

2.3.2 Classification after dominating Fluid Phase Content

The second criterion for classifying geothermal environments is based on the phase in which the geothermal fluid occurs within the system. Possibilities, therefore, if the fluid is water as in most cases are the occurrence as steam, liquid water or a mix of both. The phase in which the fluid occurs majorly depends on temperature and amount of fluid (Duffield & Sass, 2003). If a fluid is completely lacking in

a system, it is called "hot-dry-rock" (HDR). Combining all those possibilities, four types can be distinguished (Fig. 2.10; White, 1973; Duffield & Sass, 2003):

Fig. 2.10: Classification of geothermal systems after dominating fluid phase and temperature (Duffield & Sass, 2003).

1. *Normal to warm temperature systems:*
   Reservoirs containing water between 20°C and 100°C.

2. *High temperature water dominated systems:*
   Reservoirs containing liquid water from < 125°C to > 225°C, which is controlled by reservoir pressure. Those are the most frequently occurring systems in the world.

3. *High temperature steam dominated systems:*
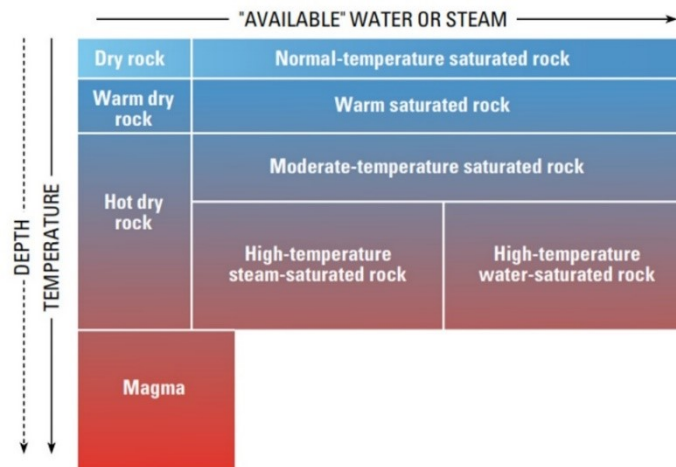   Reservoirs containing steam and liquid water, whereas steam occurs as majorly dry or superheated, steam which is also controlled by reservoir pressure. Examples are Larderello, Italy or The Geysers, California.

4. *Hot-dry-rock systems:*
   Concerning geothermal systems, heat source is the only parameter of the three described under 2.1 which needs to be natural (Dickson & Fanelli, 2004). HDR means hot, low porous/permeable rocks in depth where the fluid and pathways for it are lacking. Therefore, those two are created artificially by pumping cold, high-pressure water over an injection well down into the hot rock (1 in Fig. 2.11), causing its hydraulic fracturing and loading with water. The water then travels through the rock (2), is heated up and then is extracted with a production well (3; Garnish, 1987).

   A first experiment was executed in Los Alamos (New Mexico) but then was terminated because of economic unviability (Duffield & Sass, 2003).

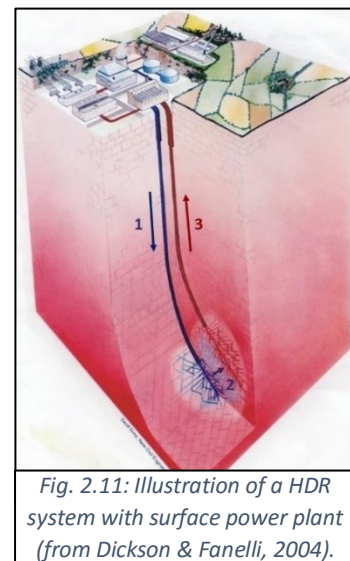*Fig. 2.11: Illustration of a HDR system with surface power plant (from Dickson & Fanelli, 2004).*

Such geothermal systems, where a certain degree of initial natural permeability is further stimulated by hydraulic fracturing or directional drilling, then are called "Enhanced Geothermal Systems" (EGS). Projects are currently running in Japan and especially Europe (Tenzer, 2000; Duffield & Sass, 2003).

2.3.3 Classification after Heat Content or Enthalpy

The classification of geothermal systems based on heat content or enthalpy, what is directly proportional to temperature (Tab. 2.2), is the most common one and therefore already gives a first estimation of how much heat can be extracted from a system (Dickson & Fanelli, 2004). The classification contains 3 subdivisions of geothermal systems but temperature limits vary greatly in literature:

	Temperature (°C)				
	(a)	(b)	(c)	(d)	(e)
Low enthalpy resources	< 90	< 125	< 100	≤ 150	≤ 190
Intermediate enthalpy resources	90-150	125-225	100-200	-	-
High enthalpy resources	> 150	> 225	> 200	> 150	> 190

Tab. 2.2: Classification of geothermal resources after heat content/enthalpy proportional to temperature (°C). (From Dickson & Fanelli, 2004. Sources: (a) Muffler & Cataldi, 1978; (b) Hochstein, 1990; (c) Benderitter & Cormy, 1990; (d) Nicholson, 1993; (e) Axelsson & Gunnlaugsson, 2000)

From this classification, the fields of utilization of geothermal energy can be inferred directly.

2.4   Utilization of Geothermal Energy and worldwide Overview

Application of geothermal energy can be divided into two big groups: a) indirect or electrical or b) direct applications. The field, for which a geothermal resource is suitable for utilization is directly obtained from the classification of geothermal systems after enthalpy/temperature and is summarized in the LINDAL-Diagram (Fig. 2.12).
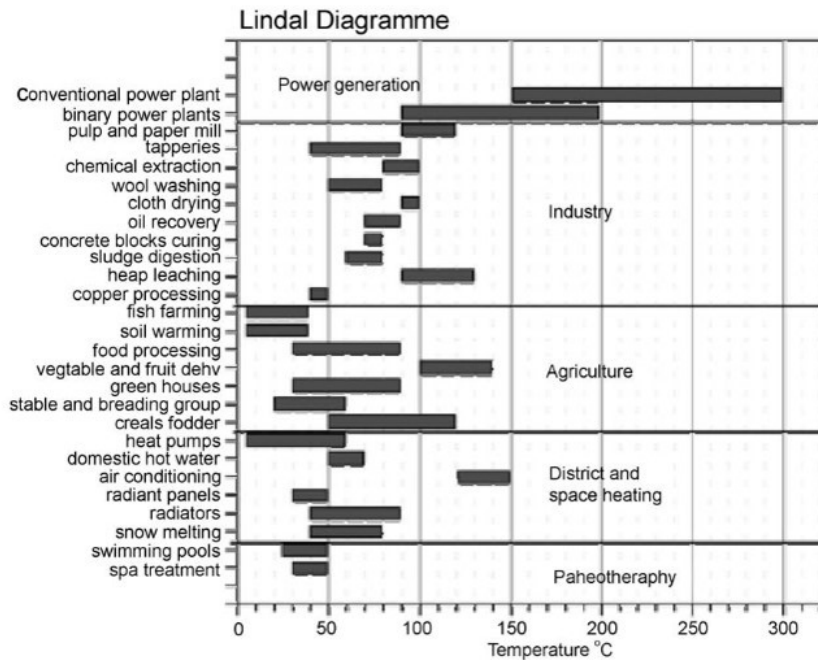
Fig. 2.12: LINDAL-Diagram for illustration of application of geothermal energy according to temperature (From Stefansson & Fridleifsson, 1998; after Lindal, 1973).

The LINDAL-Diagram shows, that for electricity generation only high temperature resources (> 90°C) are applicable, whereas low- to medium graded resources are used for all other direct applications (Mburu, 2010).

2.4.1 Electricity Generation

At the World Geothermal Congress (WGC) in April 2015 in Melbourne, Australia data concerning the actual state of worldwide geothermal power production was presented by Bertrani (2015).

By this date, a total worldwide installed capacity was 12,635 MW and the amount of produced energy was 73,549 GWh. This is an increase of almost 16% in installed capacity compared to the data presented during the previous WGC in 2010. A short forecast, including all currently running projects, was also given by Bertrani (2015), assuming an installed capacity of 21,443 MW until 2020 (Fig. 2.13).
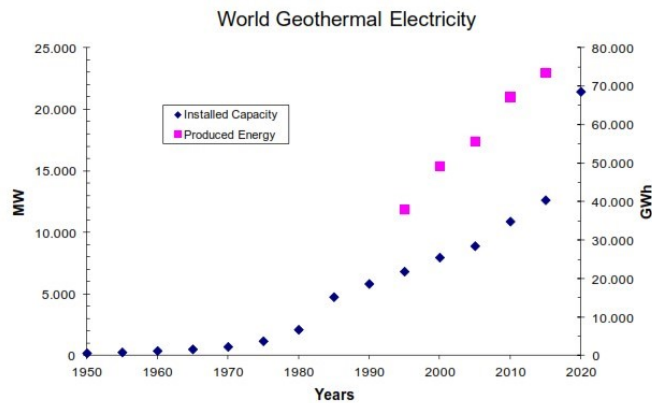
Fig. 2.13: Development of worldwide geothermal power generation from 1950 until 2015 (Bertrani, 2015).

Leading countries for installed capacity are USA, Philippines, Indonesia, Mexico, New Zealand, Iceland, Kenya and Japan (Fig. 2.14), whereas the biggest increases since 2010 were reported from Turkey (+336%) or Kenya (+194%) for example.

Fig. 2.14: Worldwide distribution of geothermal power generation in terms of installed capacity (Bertrani, 2015).

2.4.2 Direct Applications

Direct applications use low- to medium enthalpy resources and therefore are manifold what can be seen in the LINDAL-diagram in Fig. 2.12. Most common and most impor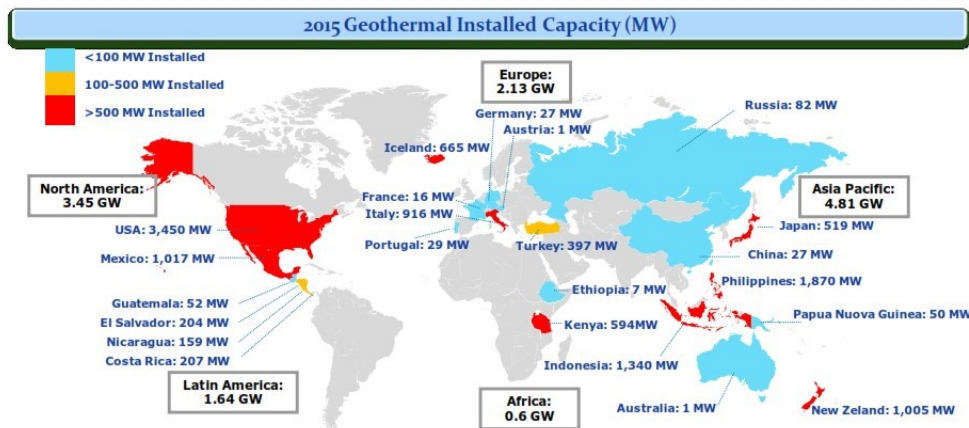tant uses are in heat pumps for air conditioning, urban space and district heating, balneology, agriculture and aquaculture.

Urban space and district heating

Heating of houses by geothermal resources including heat pumps are probably the most important direct application of geothermal energy. The geothermal fluid is extracted over production wells and then is guided either directly or over heat exchangers into the local pipeline network and enters buildings, where another heat exchanger and pipes distribute the warm water within each household. The cold geothermal fluid is either drained or guided back to the plant, in most cases consisting of a geothermal doublet, and reinjected into the reservoir.
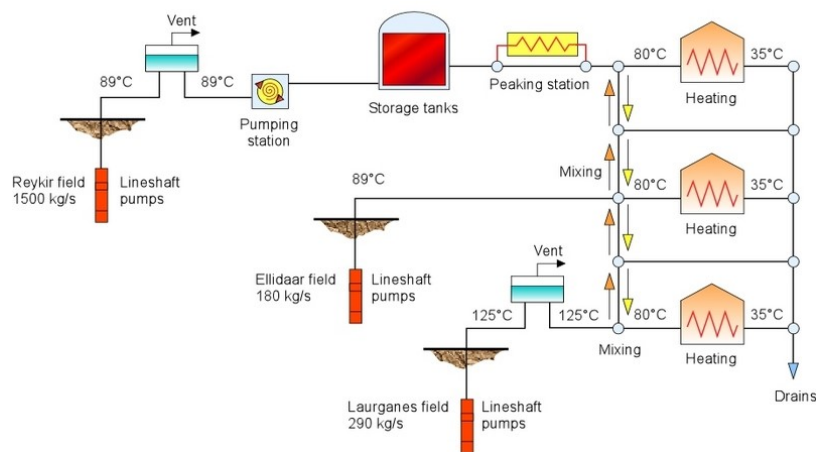
Fig. 2.15: Illustration of an urban space or district heating network exemplified by the Reykjavik district heating system where the water enters the units with a temperature of about 80°C (Gudmundsson, 1988).

Most important examples for this type of direct application are a) the Reykjavik district heating system (Fig. 2.15), Iceland, covering 200,000 people what is about 67% of the total Icelandic population and almost 100% of the city (Lund & Boyd, 2015) or b) in a smaller scale in the region around Paris and the Aquitaine Basin, southwestern France, where 60-80°C warm water is produced from 1.5-2 km deep wells for providing heat to about 200,000 households (Duffield & Sass, 2003).

In addition to large scale district heating systems, ground-coupled heat pump systems for separate units also play a major role in space conditioning.

Agricultural uses

Major agricultural use of geothermal energy is greenhouse heating for cultivation of out-of-season flowers and vegetables and reaching best growth conditions. Greenhouses are heated either by hot water circulating through a pipe system in or on the floor, on the walls or in benches (Fig. 2.16 a-d) or by forced air circulation derived from heat exchangers (Fig. 2.16 e-h; von Zabeltitz, 1986).
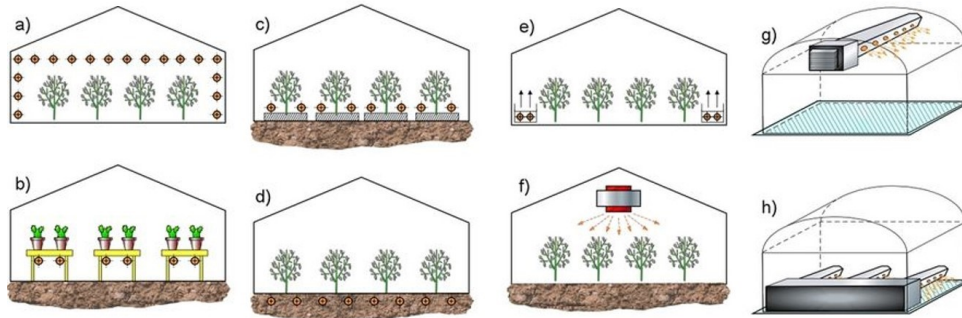
Fig. 2.16: Greenhouse heating systems with natural air movement caused by hot water pipes (a-d) or forced air convection (e-h). (von Zabeltitz, 1986)

Further agricultural applications are seed or wood drying, cultivation of fungi or fruit/vegetable dehydration. Aquacultural applications mainly include establishing perfect growing environment for fish (sturgeon, caviar, carp, catfish,…) or even crocodiles or caimans as tourist attractions in the USA (Dickson & Fanelli, 2004).

Balneology

Geothermal resources are used worldwide for recreation in spas and is even the dominating field of utilization in the Styrian Neogene Basin and is therefore described in more detail below (section 2.6).

Direct uses worldwide

Geothermal heat pump systems are without doubt the major direct use in the world, followed by balneology and urban space heating (Fig. 2.17 a). Fig. 2.17 b shows the development of direct geothermal energy utilization since 1995 and illustrates a steadily increasing installed capacity as well as energy used. Leading countries in terms of direct-use installed capacity are China, USA, Sweden, Turkey, Germany, France, Japan and Iceland making up 75.6% of total worldwide direct utilization (Lund & Boyd, 2015).

Fig. 2.17: Worldwide direct uses of geothermal resources in terms of installed capacity in MWt (a) and development with total numbers of capacity in MWt and utilization in TJ/yr from 1995-2015 (b; Lund & Boyd, 2015).

2.5 Economic Considerations and Environmental Impacts

2.5.1 Economic Considerations

When talking of economic investment for using a geothermal resource, two general types of costs must be considered: a) Initial installation costs, when setting up a geothermal project/plant including wells (about 55%; WEC, 2013), pipeline/electricity network, u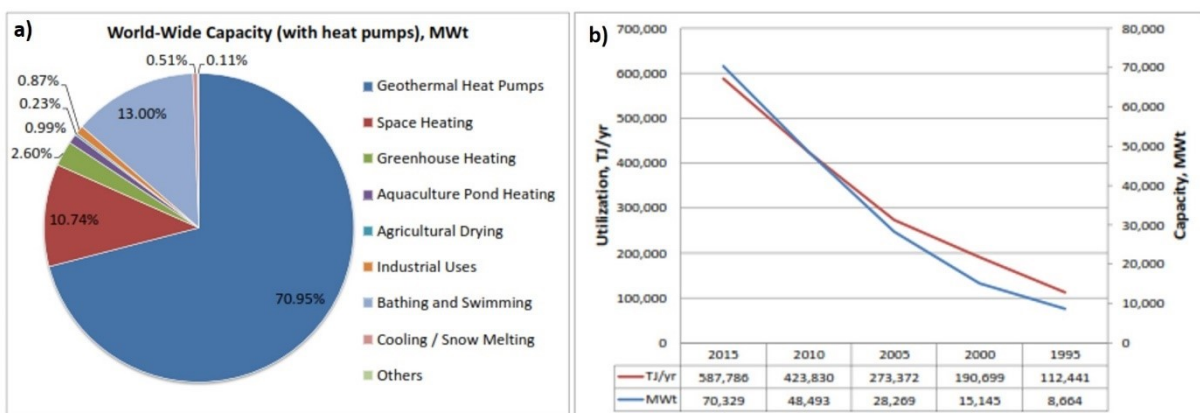tilization plant amongst others and b) operation or maintenance costs when the project/plant already runs. Generally, while installation costs are very high, even higher than for conventional fossil energy sources, operational costs, i.e. energy that is needed for running a geothermal plant, are lower than those for fossil ones or other renewables. Therefore, energy efficiency of geothermal energy is given by the savings gained from low operational costs, i.e. the shorter amortization time than for fossil energy (Dickson & Fanelli, 2004).

The costs for producing electricity from different energy sources are expressed as "Levelised costs of electricity" or LCOE and are defined as "the price that must be received per unit of output as payment for producing power in order to reach a specified financial return – or simply, the price that a project must earn per MWh to break even" (WEC, 2013). In the following, data concerning costs of different energy sources compared to geothermal energy are derived from the World Energy Council (WEC, 2013) in cooperation with Bloomberg New Energy Finance:

Fig. 2.18: LCOE development of geothermal electricity production in Flash- and Binary Cycle Power Plants (WEC, 2013).

LCOE for geothermal electricity production currently varies between 50 and 100 US$/MWh, depending on production type (flash vs. binary plants, Fig. 2.18). Compared to other sources of energy, geothermal electricity production shows quite low LCOE in the range of coal or Combined Cycle Gas Turbine (CCGT), whereas additional costs for CO_2 emissions for fossils are not included in Fig. 2.19. Furthermore, a very high capacity factor (up to 95%) makes geothermal energy much more efficient compared to other renewables. The capacity factor of an electric power plant is defined as the ratio between the energy really produced within a period of time and the energy which could have been produced if the plant would have run on full load.
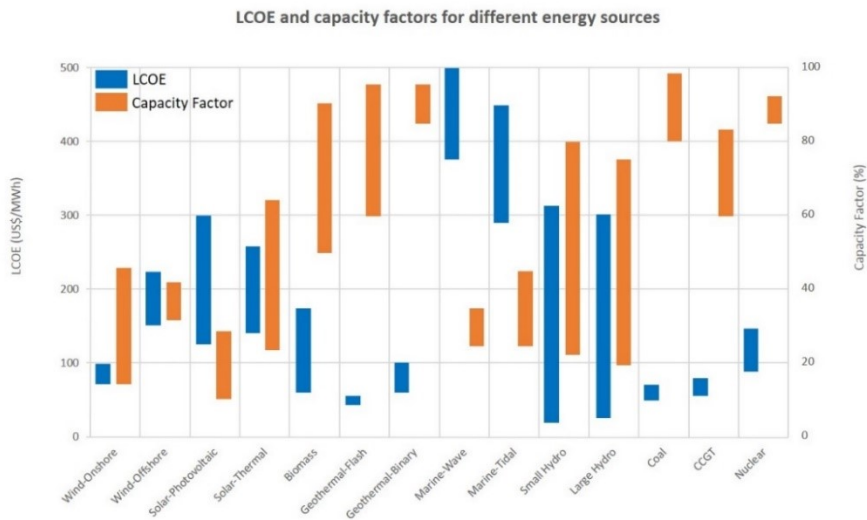
Fig. 2.19: Diagram showing the LCOE (blue) and capacity factors (orange) for different types of both, renewable and fossil energy sources. Data from WEC (2013).

For conclusion, geothermal energy is the only renewable energy which can cope with the efficiency (LCOE vs. capacity factor) of fossil energy sources or nuclear power.

2.5.2 Environmental Impacts

In general, direct as well as electric utilization of geothermal energy is free of emissions of CO_2, NO_x, SO_x, other harmful gases or dust particles, whereas installation of a geothermal plant (from exploration over drilling until construction of a pipeline network and the plant itself) is combined with a certain amount of emissions due to raw material production and transportation and other services (Stober & Bucher, 2012).

During production, environmental impacts increase significantly if the geothermal fluids containing CO_2, H_2S, NH_3, CH_4 and other dissolved substances (e.g. B, As, Hg) are released to the environment instead of being reinjected (Dickson & Fanelli, 2004). But as shown in Fig. 2.20 for CO_2, emissions are far below those of fossil energy sources, especially oil and coal.

Fig. 2.20: CO_2 emissions in kg per MWh for different geothermal power plants compared to fossil energy sources. Data from Fridleifsson, 2001.

Further possible environmental impacts are shown in Tab. 2.3 with probability of occurrence and severity of consequences (Lunis & Breckenridge, 1991):

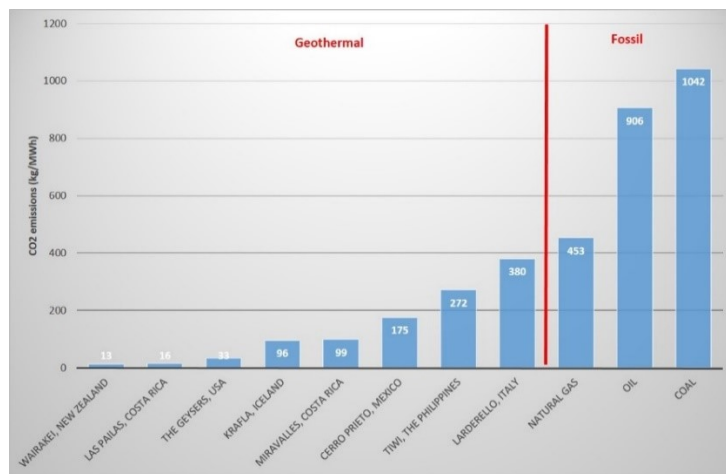| Impact	Probability of occurrence	Severity of consequences
Air quality pollution	L	M
Surface water pollution	M	M
Underground pollution	L	M
Land subsidence	L	L – M
High noise level	H	L – M
Well blow-out	L	L – M
Conflicts with cultural and archaeological features	L – M	M – H
Social-economic problems	L	L
Chemical or thermal pollution	L	M – H
Solid waste disposal	M	M – H

Tab. 2.3: Possible environmental impacts of geothermal energy utilization with concerning probability of occurrence and severity of consequences. L=Low, M=Middle, H=High, from Lunis & Breckenridge, 1991.

2.6   Geothermal Energy in Austria

A short overview of geothermal energy utilization in Austria and especially in the Styrian Neogene basin should finalize this first introductory chapter to geothermal energy.

Geothermal energy utilization in Austria is mainly occurring in the Upper Austrian Molasse Basin and in the Styrian Neogene Basin (Fig. 2.21), whereas some minor utilization occurs within the Eastern Alps and the Vienna Basin, where warm natural springs are used for balneology (e.g. Villach, Bad Gastein, Bad Vöslau amongst others; Goldbrunner, 2015).
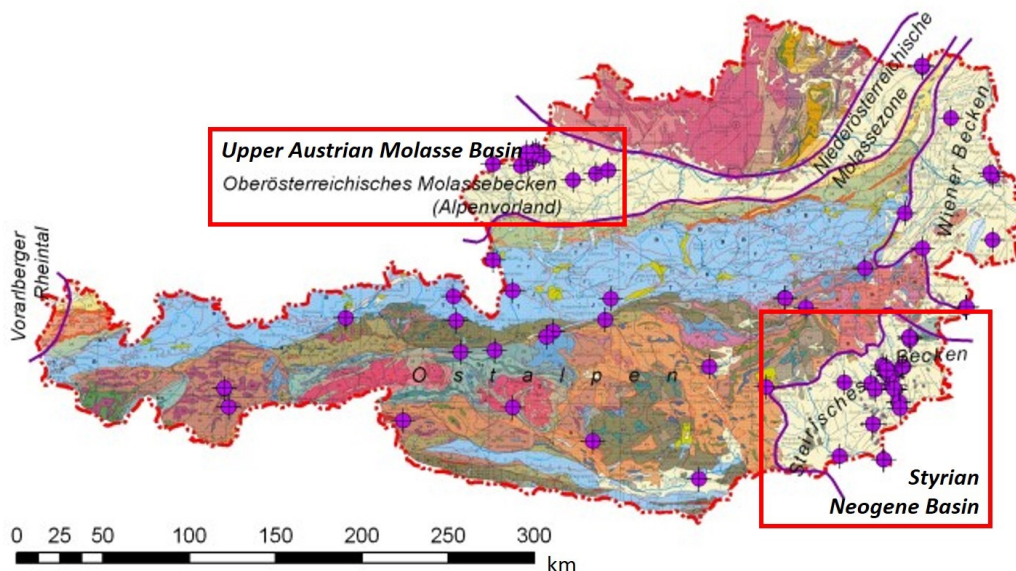

Fig. 2.21: Geothermal activity in Austria, especially in the Upper Austrian Molasse Basin and the Styrian Neogene Basin (red boxes). Modified from Goldbrunner (2015).

Geothermal energy in Austria is exploited from deep reservoirs by wells (in total 75 with a cumulative length of about 130 km; Goldbrunner, 2015) of partially more than 3,000 m depth (e.g. Fürstenfeld, Stegersbach in the Styrian Neogene Basin; Goldbrunner et al., 2010) with temperatures not exceeding 110-130°C (Goldbrunner, 2015) and therefore can be classified as low to medium enthalpy systems. Subsequent major economic applications are ground-coupled heat pump systems (about 70,000 units), balneology (27 spas), district heating (9 systems), greenhouse heating and in medium temperature reservoirs also electricity production (e.g. Simbach-Braunau in Upper Austria (decommissioned) or Bad Blumau in the Styrian Basin; Tab. 2.4; Goldbrunner, 2015).

Project	T (°C)	Utilization
Bad Waltersdorf	63	D, B, G
Bad Blumau	110	E, D, B, CO_2
Loipersdorf	61	B, D
Bad Radkersburg	70	B,D

Tab. 2.4: Examples of geothermal energy utilization with temperatures in the Styrian Neogene Basin. E=Electricity production, D=district heating, B=balneology, G=greenhouse heating, CO_2=substantial use of carbon dioxide. Data from Goldbrunner et al., 2010 and Goldbrunner, 2015.

Electricity generation in Austria declined from 3.8 GWh in 2010 to 2.2 GWh in 2015 because of the closure of the Simbach-Braunau plant in the Upper Austrian Molasse Basin, whereas direct utilization for 2015 is numbered with 1,816.26 GWh for energy production or 903.4 MWt for installed capacity (Goldbrunner, 2015) and is distributed as shown in Fig. 2.22.
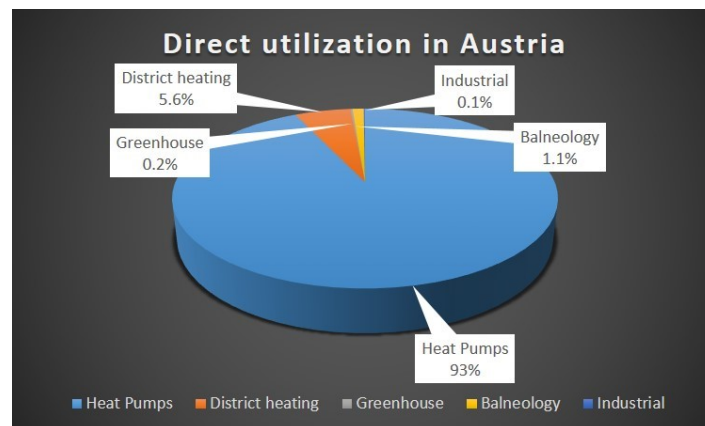
Fig. 2.22: Distribution of direct geothermal energy utilization in Austria in % of installed capacity. Data from Goldbrunner, 2015.

As a conclusion, major applications of deep, low to medium temperature geothermal systems in Austria are district heating systems, especially in the Upper Austrian Molasse Basin and balneological uses in the Styrian Neogene Basin. Ground-coupled heat pumps comprise about 93% of total direct utilization and number of projects is still increasing (+40% since 2010; Goldbrunner, 2015).

3   Regional Geology of the Styrian Neogene Basin

3.1   Introduction

The Styrian Neogene Basin is a sedimentary basin in the southeastern part of Styria, Austria (Fig. 2.25) filled with Miocene, mainly clastic sediments. The Styrian Basin is a subbasin of the Pannonian Basin System and is separated from the Western Pannonian Basin, which opens up towards east to Hungary, by the NE-SW trending South Burgenland Swell. Internally, it is subdivided into a Western and an Eastern Styrian Basin, which again are separated by the N-S trending Middle Styrian Swell. Further smaller subbasins (e.g. Fürstenfeld, Gnas subbasins) and bays are divided by subordinate basement swells (e.g. Auersbach swell; Fig. 3.1; Kollmann, 1965; Kröll, et al., 1988; Gross et al., 2007).
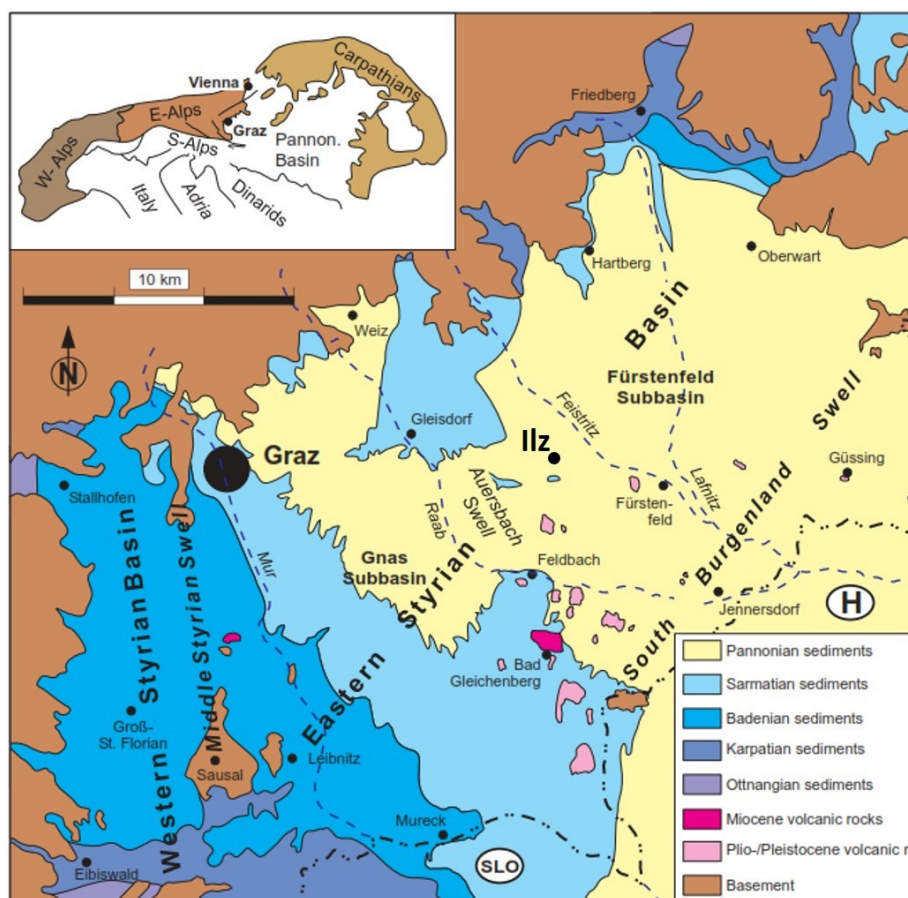
Fig. 3.1: Geological map of the Styrian Neogene Basin with the approximate location of Ilz (modified after Gross et al., 2007).

The extension of the basin is about 100 km in NE-SW direction and 60 km in NW-SE direction (Gross et al., 2007). Central parts of the basin can reach depths of up to 4,000 m as estimated by Sachsenhofer et al. (1996) from gravimetric and seismic studies. Towards N, NW, W and SW the basin overlies crystalline rocks of the Lower and Middle Austroalpine Units and Upper Austroalpine low-grade metamorphic phyllites and carbonates of the Graz Paleozoic, which also comprise the basement rocks underlying the Miocene sediments. Basement rocks also crop out within the basin in the Sausal Mountains. Penninic units of the Köszeg Mountains, Hungary, define the border of the basin towards NE (Gross et al., 2007).

Sedimentation in the Styrian Basin started in Ottnangian times about 18 Ma ago and lasted until Badenian times (about 13 Ma) in the Western Styrian Basin and until Pannonian times (about 8 Ma) in the Eastern Styrian Basin (Fig. 3.2; Piller et al., 2004). This is represented by the distribution of outcropping sediments on the surface today, which is shown in Fig. 3.1. Ottnangian and Karpatian sediments are very restricted to the S-SW and NE margins of the basin whereas Badenian and Sarmatian sediments dominate in the shallower Western Styrian Basin and western part of the Eastern Styrian Basin and Pannonian sediments dominate in the major part of the Eastern Styrian Basin.

Direct information about sedimentary infill and subsurface structure of the Styrian Basin is derived from classical geological mapping and deep drilling projects (currently 28 wells with a total length of about 48,000 m according to Goldbrunner, 2015) which started in the 1970s by the "Rohöl-Aufsuchungs AG" (RAG, Crude Oil Mining Company; Kollmann, 1965) for the purpose of hydrocarbon exploration and then for geothermal production (Goldbrunner, 2015). Indirect information is provided by geophysical borehole measurements, seismic, magnetic and gravimetric studies (e.g. Kröll et al., 1988).
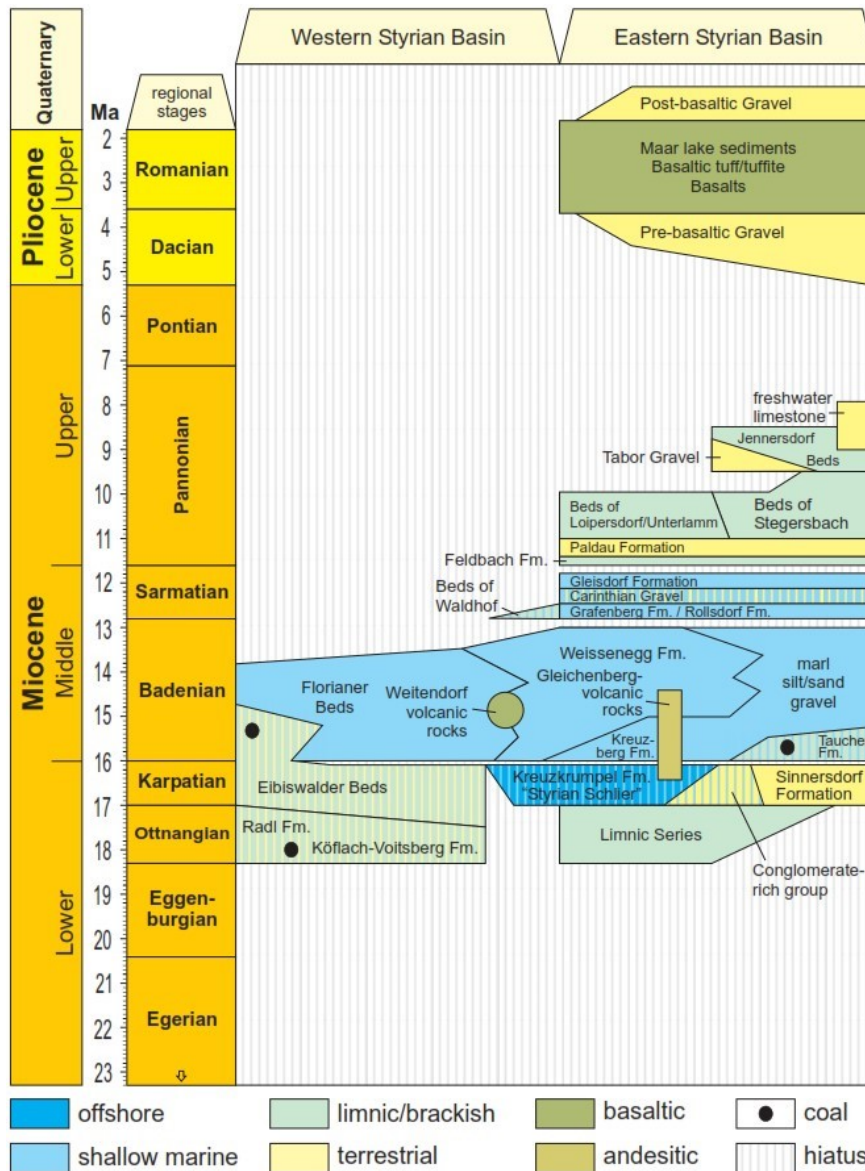

Fig. 3.2: Stratigraphic chart of the sedimentary infill of the Styrian Neogene Basin (Gross et al., 2007, modified after Piller et al., 2004)

3.2   Basin Tectonics

The Styrian Neogene Basin is a result from a lateral eastward extrusion of Alpine nappes and crustal wedges in a late stage of the Alpine orogenesis (Ebner & Sachsenhofer, 1995) starting in the Late Oligocene to Miocene. This so-called "continental escape" movement occurred along E-W trending sinistral strike-slip faults in the N and NW (e.g. Noric Depression) and the dextral Periadriatic Lineament in the S and SW (Fig. 3.3; Genser & Neubauer, 1989; Neubauer & Genser, 1990; Ratschbacher et al., 1991a, b; Ebner & Sachsenhofer, 1991). Those lineaments define the margins of the Alpine crustal wedge on which the Styrian Basin formed as an extension basin (Ebner & Sachsenhofer, 1995), indicated by a synrift horst-graben structure affecting the basement (Fig. 3.5).
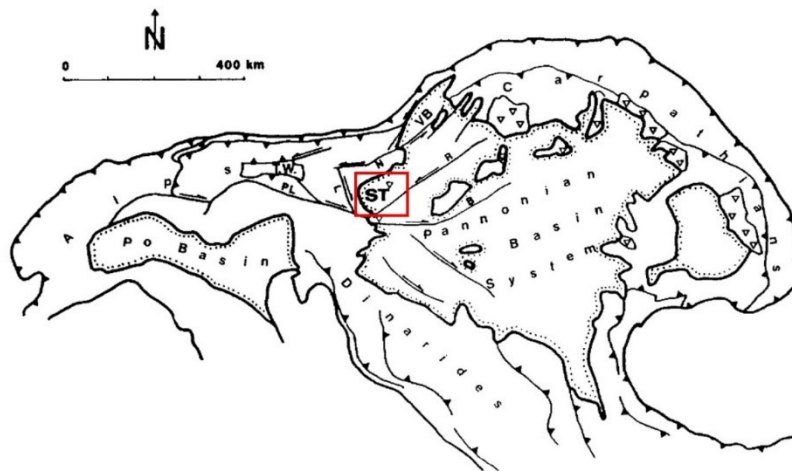

Fig. 3.3: Tectonic map of the Alpine-Carpathian-Dinaride region with location of the Styrian Neogene Basin (ST) within the Pannonian Basin System (modified from Ebner & Sachsenhofer, 1995 after Royden, 1988). N=Noric Depression, PL=Periadriatic Lineament, TW=Tauern Window, L=Lavant Line, B=Balaton Line, R=Raaba Line, VB=Vienna Basin.

Sediments in the Styrian basin can be distinguished in an Ottnangian – Karpatian synrift phase and a subsequent postrift phase (Sachsenhofer et al., 1996). The boundary between Early Miocene synrift and Middle Miocene postrift sediments is formed by the so-called Styrian Unconformity which is thought to be connected to block tilting and erosion at the boundary Early-Middle Miocene (Friebe, 1991).

3.3   Structure and Lithology of the Pre-Neogene Basement

The Pre-Neogene basement of the Styrian Basin comprises five tectonic units, which in different locations, underlie the Neogene sedimentary basin fill (Fig. 3.4). The lowest of the five units are metamorphic rocks of the Penninic "Rechnitz Group", restricted to the NE part of the basin and underlying crystalline rocks of Lower and Middle Austroalpine units, which occupy the major part of the basement. Those again are overlain by Upper Austroalpine Paleozoic phyllites occurring mainly in tectonic heights and basement swells (e.g. Middle Styrian Swell, South Burgenland Swell). Upper Austroalpine limestones and dolomites of the Graz Paleozoic as the fourth tectonic unit build up the major part of the basement in the Fürstenfeld subbasin, where also the thickest Neogene sedimentary infill of 2,747.7 m in the whole Styrian Basin was reached by the well Fürstenfeld Thermal 1 (Fig. 3.5; Goldbrunner, 1988). Those carbonates underwent a brittle deformation and hence represent important thermal aquifers in geothermal exploration (Goldbrunner et al., 2010).
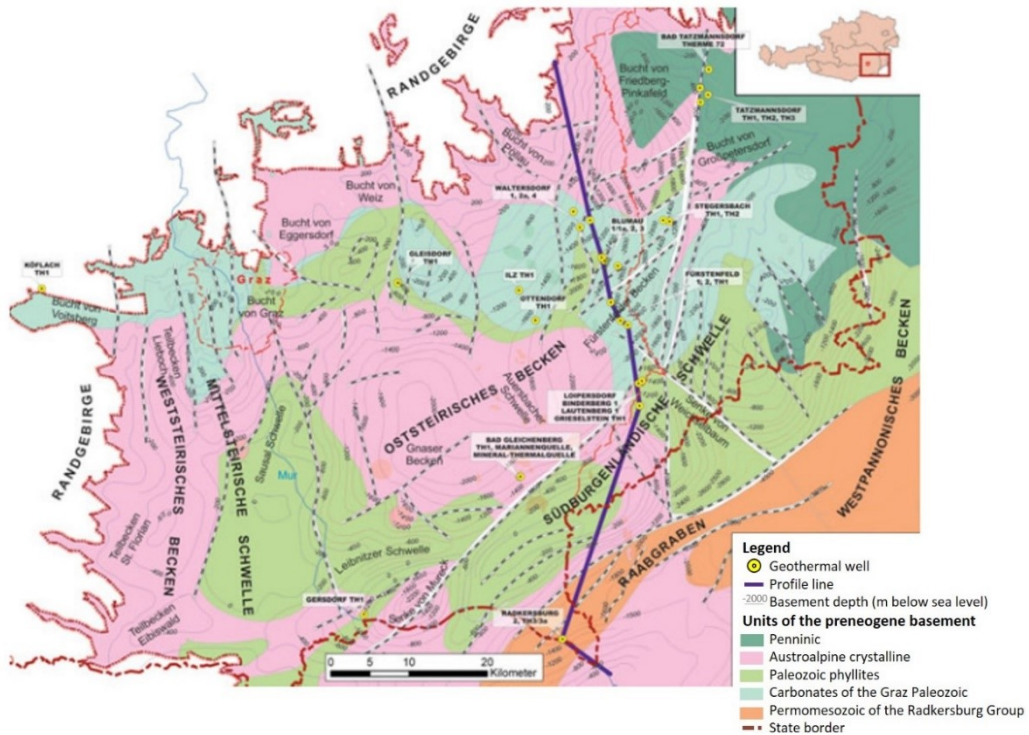
Fig. 3.4: Structural map of the Pre-Neogene basement indicating basement lithologies, depths of basement rocks and geothermal wells. The cross section is shown in Fig. 3.5. (Modified from Goldbrunner et al., 2010)

The fifth tectonic basement unit are Permomesozoic rocks of the Radkersburg Group, which are restricted to the most southeastern part of Styria but actually are not part of the Styrian Basin. Because of their occurrence in the Raabgraben, SE of the South Burgenland Swell, they are already part of the Western Pannonian Basin but are mentioned here because Triassic carbonates also represent important geothermal aquifers in this area (Fig. 3.5; Goldbrunner et al., 2010).
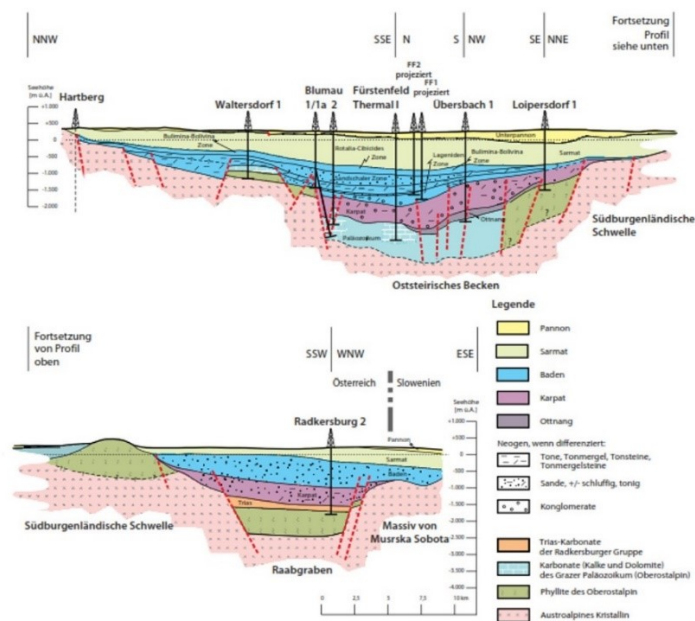
Fig. 3.5: Geological N-S cross section through the Styrian Neogene Basin along the line shown in Fig. 3.4 (Goldbrunner et al., 2010).

3.4   Neogene Basin Evolution

The Neogene sedimentary evolution of the Styrian Basin was mainly affected by ingressions and regressions of the Paratethys Ocean, which developed after the closure of the Tethys Ocean after the collisions of Eurasia, India and Africa around the Eocene/Oligocene boundary. Paleogeographically, the Central Paratethys extended from the Bavarian Molasse Zone in the west to the Carpathians in the east (Gross et al., 2007). Therefore, the Styrian Basin formed an embayment at the southwestern coast of the Ocean and sedimentary provenance is given by the Alps in the hinterland. Due to the location of the well ILZ Thermal 1 in the Fürstenfeld subbasin in the Eastern Styrian Basin, the focus of the subsequent summary of basin evolution lies on this region.

3.4.1 Lower Miocene (18 – 16 Ma)

Sedimentation started during Ottnangian times (about 18 Ma ago) with the deposition of syn-rift limnic-fluviatil sediments including basal red paleosoils and breccias, conglomerates and bituminous marls with thin coal seams derived from fluviatile flooding surfaces, moorlands and coastal areas ("Limnic Series" in Fig. 3.2; Polesny, 2003). Those reach a thickness of up to 300 m in the Fürstenfeld subbasin (Kollmann, 1965; Sachsenhofer & Littke, 1993) as documented from the well Übersbach 1 (RAG). A shallow marine environment with thicknesses reaching 1000 m is proposed for the Gnas subbasin by Sachsenhofer & Ebner (1995) based on seismic data. On the margins of the basin, proximal fan-delta complexes are known from the Bays of Weiz ("Beds of Naas"), Eibiswald (Radl Formation, Lower Eibiswald beds) or Friedberg-Pinkafeld ("Breccia of Zöbern"; Fig. 3.4; Kollmann, 1965).
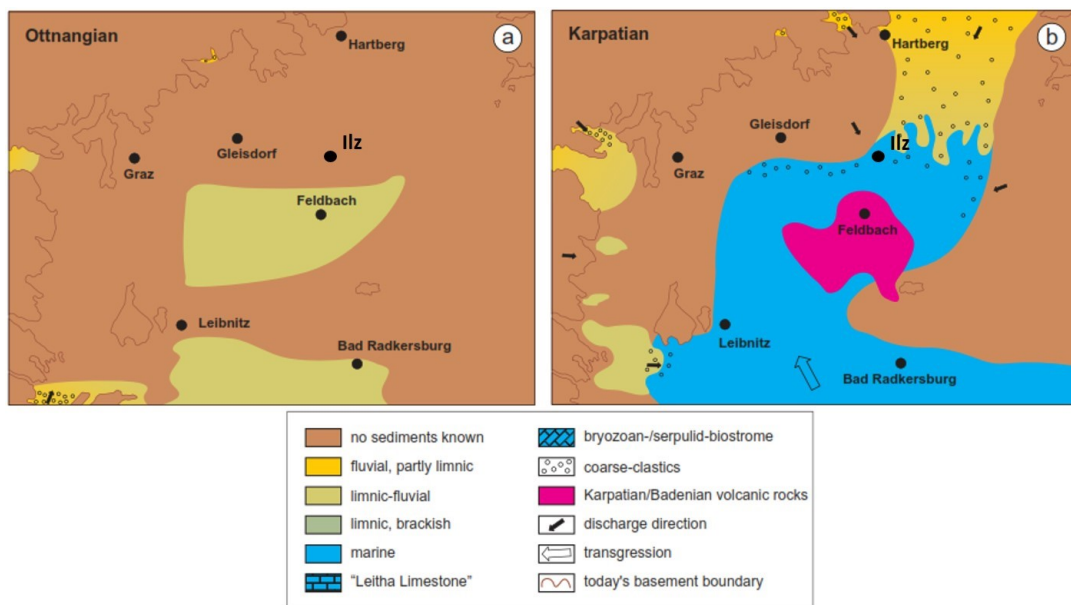
Fig. 3.6: Paleogeographic facies maps for the Lower Miocene (Ottnangian (a) – Karpatian (b); modified after Gross et al., 2007)

Karpatian syn-rift sedimentation was affected by a marine ingression from the S (Fig. 3.6 b), synsedimentary fault tectonics and volcanic activity. Tectonic activity led to the uplift of the Middle Styrian Swell and reached its climax in late Karpatian times. A coeval acid to intermediate volcanic activity occurred in the Eastern Styrian Basin forming huge shield volcanoes (e.g. Gleichenberg) as islands in its southern part (Ebner & Sachsenhofer, 1995) and then shifted northwards (e.g. Walkersdorf-Ilz) in Early Badenian times (16 Ma; Fig. 3.7 a). Shallow location of magma chambers

induced high heat flows of over 300 mW/m² as calculated by Ebner & Sachsenhofer (1995). The calcalkaline character points to a subduction-related magmatism (Ebner & Sachsenhofer, 1991). Petrographically the volcanic rocks are K-rich trachyandesites to rhyolites, which locally represent geothermal reservoirs due to their permeability (e.g. Bad Gleichenberg; Goldbrunner et al., 2010).

The marine ingression led to the deposition of several hundred meters thick calcareous mudstones and siltstones with sandy, turbiditic intercalations in the southern part of the Eastern Styrian Basin ("Styrian Schlier" in Fig. 3.2; e.g. Friebe, 1990) where water depths of 500-600 m are estimated from seismic data for the central Gnas subbasin (RAG). Towards north, to the margin of the basin, the marine environment graded into a fluvial fan environment in the Fürstenfeld subbasin and towards N-NE to the Bay of Friedberg-Pinkafeld with further transgression of the shoreline (Fig. 3.6 b). Subsequent deposition of conglomerates (e.g. Ebner, 1988; Goldbrunner, 1988) led to the formation of the Karpatian Conglomerate-rich Group and the Sinnersdorf Formation (Fig. 3.2), where freshwater conglomerates interfinger with fine-grained sediments containing volcanic ashes altered to bentonites (Ebner & Gräf, 1977, 1982; Ebner, 1981).

After a sea level highstand in the late Karpatian, which correlates with a global highstand (Schreilechner, 2007), a regression led to an eustatic low stand at the end of the Karpatian. Together with the climax of tectonic movements causing block tilting and rotations, erosion commenced to form the "Styrian Unconformity" (Friebe, 1991).

3.4.2 Middle Miocene (16 – 11.5 Ma)

In the Lower Badenian, subsidence rates decreased from about 30 cm/100 yrs in the Karpatian to below 10 cm/100 yrs initiating the post-rift phase (Ebner & Sachsenhofer, 1995). Karpatian volcanic complexes of the southern Eastern Styrian Basin were covered with marine sediments after an eustatic sea level rise (Friebe, 1990; Rögl, 1998; Kovac et al., 2004), whereas andesitic to shoshonitic volcanic activity continued in the north (Walkersdorf-Ilz) and in the area of the Middle Styrian Swell (Weitendorf-Wundschuh; Ebner & Sachsenhofer, 1991). Sea level rise led to the flooding of the entire Styrian Basin and parts of the South Burgenland Swell establishing shallow marine conditions in the major part of the basin. Limnic and fluvial sediments are only known from the Western Styrian Basin (Fig. 3.7 a; Ebner & Gräf, 1979).
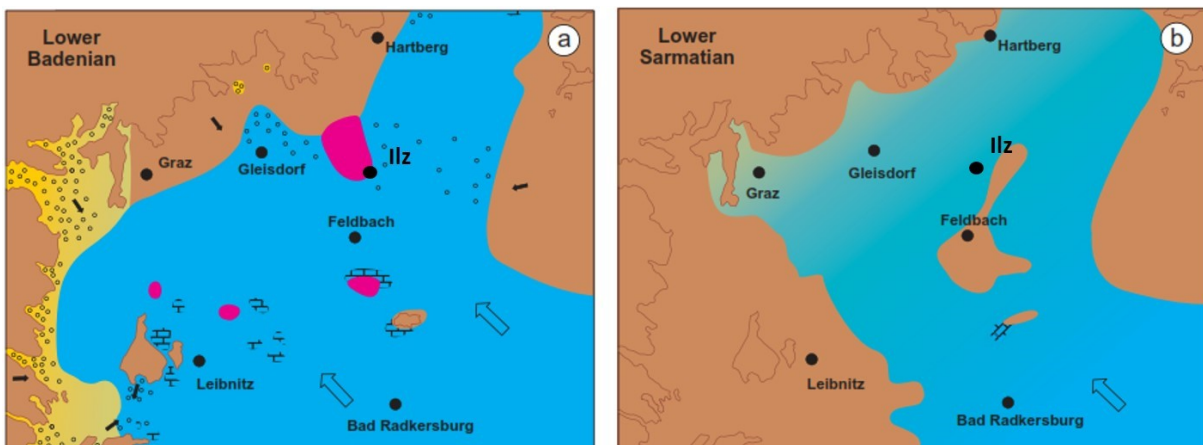

Fig. 3.7: Paleogeographic facies maps for the Middle Miocene (Lower Badenian (a) – Lower Sarmatian (b); legend see Fig. 3.6; modified after Gross et al., 2007)

In the Fürstenfeld subbasin and the Bay of Friedberg-Pinkafeld, sea level fluctuations can be distinguished into three transgressive-regressive sequences of the 3rd order (Schreilechner, 2007) and therefore, together with varying subsidence rates, lead to complex facies shifts in the Badenien (Friebe, 1990). From N to S, a delta system with coal seams developed in the Bay of Friedberg-Pinkafeld (Tauchen Formation in Fig. 3.2), whereas coarse marine conglomerates ("Base Conglomerate") were deposited in the central Fürstenfeld basin and the northern margin of the Gnas subbasin (Ebner, 1988). Towards S, open marine conditions caused pelitic with subordinate turbitic sedimentation (Gross et al., 2007). On basement highs (e.g. Middle Styrian Swell, South Burgenland Swell) and on slopes of Karpatian shield volcanoes coral patch reefs and rodolith-platforms developed (Fig. 3.7 a) forming, together with siliciclastic shallow marine sediments, the Weißenegg Formation (Friebe, 1990), which locally show enhanced permeabilities for geothermal exploration (Goldbrunner et al., 2010).

With sea level transgression and regression cycles during middle and late Badenien times, marine shaly ("Tonmergel Series") and sandy sediments with thicknesses of up to 1,000 m were deposited in the Eastern Styrian Basin. Especially sandy formations of the "Lageniden Zone", the "Sandschaler Zone" and the "Bulimina-Bolivina-Zone" show good aquifer properties in the Fürstenfeld subbasin for geothermal exploration (Goldbrunner et al., 2010).

An eustatic sea level lowstand ended the full marine environment of the Paratethys (Rögl & Steininger, 1984) and caused erosional unconformities at the Badenien/Sarmatian boundary (~13 Ma; Harzhauser & Piller, 2004a, b).

In the Lower Sarmatian, a transgression again led to the establishment of shallow marine conditions with deposition of pelitic sediments intercalating with limestones and permeable sands and gravels in a lagoonal facies at the basin margin and the Eastern Styrian Basin ("Beds of Waldhof", Rollsdorf Formation; Krainer, 1984; 1987a; Goldbrunner et al., 2010). At the boundary to the Upper Sarmatian, sea level regression caused the sedimentation of an about 30 m thick distinct interlayering between gravels and sands with marls ("Carinthian Gravel"; Winkler, 1927a; Skala, 1967; Goldbrunner et al., 2010). Sea level fluctuations in the Upper Sarmatian deposited carbonate siltstones, marls, sands and oolitic carbonaceous sandstones which form the Gleisdorf Formation (Fig. 3.2). Sarmatian sediments can also reach total thicknesses of over 1,000 m (Goldbrunner et al., 2010).

3.4.3 Upper Miocene (11.5 – 7 Ma)

Upper Miocene or Pannonian sediments only occur in the Eastern Styrian Basin, whereas Lower Pannonian sediments dominate. A sea level fall at the Sarmatian/Pannonian boundary caused the se-
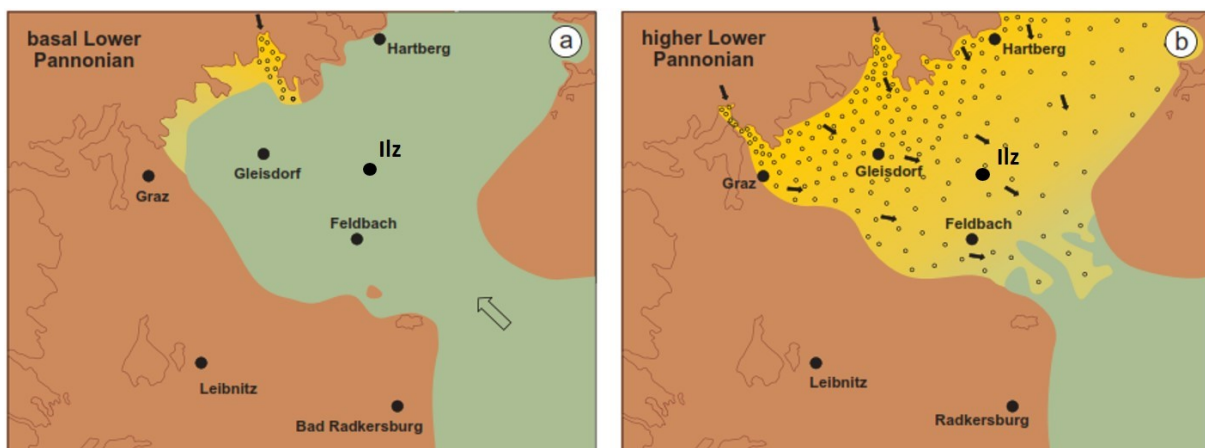

Fig. 3.8: Paleogeographic facies maps for the basal (a) and upper (b) Lower Pannonian (legend see Fig. 3.6; modified after Gross et al., 2007)

paration of the Central from the Eastern Paratethys, which led to the formation of the "Lake Pannon" (Kazmer, 1990; Magyar et al., 1999; Rögl 1999; Sacchi & Horvath, 2002; Kosi et al., 2003; Harzhauser et al., 2004). Basal Pannonian sediments include coal bearing coarse clastics followed by limnic-brackish pelites and limnic-deltaic pelite-sand alternations with coal seams, summarized in the Feldbach Formation (Fig. 3.2; Fig. 3.8 a; Gross, 2000; 2003). A subsequent regression in the upper Lower Pannonian changed conditions into a fluvial regime with development of alluvial fans, meandering and braided rivers (Paldau Formation) and finally delta systems in the SE (Fig. 3.8 b; Winkler, 1927; Krainer 1987 a, b; Gross, 1998).

Middle to Upper Pannonian sediments only occur in areas close to the Styrian border and in Burgenland to the east and include alternations of coal bearing mud, sand and gravel ("Beds of Loipersdorf"/"Beds of Stegersbach").

Total thicknesses of up to 600 m make the Pannonian coarse clastic sediments significant porous aquifers for thermal waters and especially in shallower areas for drinking water (Goldbrunner et al., 2010).

3.4.4 Pliocene and Quaternary

After Pannonian sedimentation ended in the Styrian Basin, erosion started and is active until present times. A second volcanic phase started in the Pliocene and lasted until the Early Pleistocene (3.8 – 1.7 Ma; Stradner Kogel, Klöch; Balogh et al., 1994). Products of this phase are Na-rich nephelinitic to basanitic lava flows and pyroclastic rocks related to pipes, calderas and maar lake deposits (Ebner & Sachsenhofer, 1995). Volcanic rocks are under-/overlain by fluvial "Pre-/Post-basaltic Gravels" and residual soils (Fig. 3.2; Winkler-Hermaden, 1957).

3.5   Summary of Basin Evolution

The Styrian Basin developed as an extensional basin on top of a crustal wedge which was laterally extruded due to continental escape tectonics in a late stage of Alpine orogeny. Sedimentary evolution started with beginning subsidence in Ottnangian times and lasted until the Upper Pannonian, whereas an Ottnangian-Karpatian syn-rift phase is followed by a Badenian-Pannonian post-rift phase. Highest subsidence rates were reached during Karpatian times with about 30 cm/100 yrs reaching total present basin depths of up to 4,000 m (Fig. 3.9; Ebner & Sachsenhofer, 1995). Sedimentation ended in Upper Pannonian due to beginning uplift.
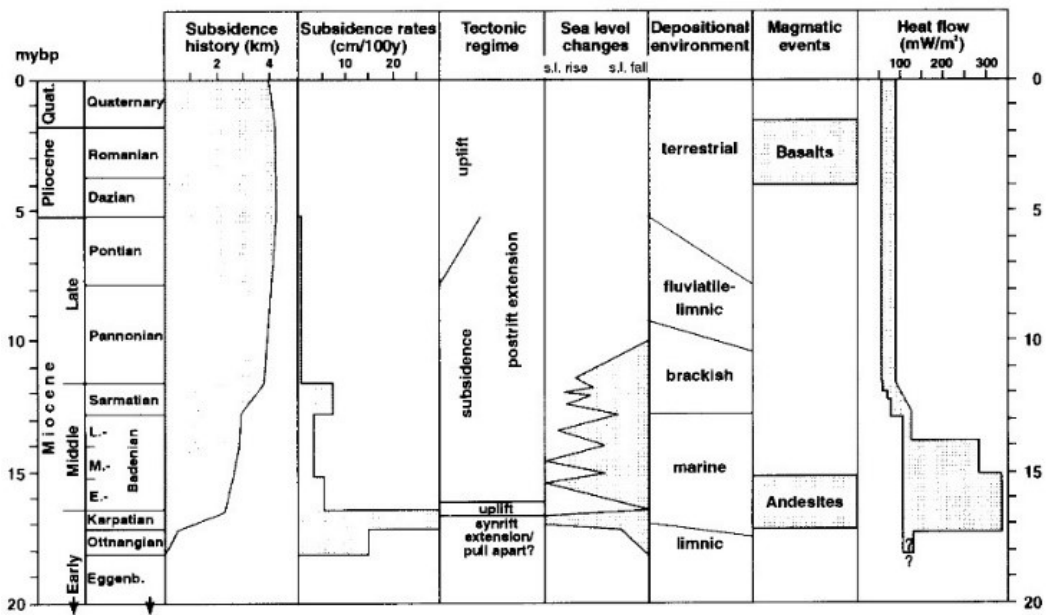

Fig. 3.9: Summary of the Neogene evolution of the Styrian Basin. (Ebner & Sachsenhofer, 1995; Badenian sea level changes according to Friebe, 1993; Sarmatian and Pannonian sea level changes are highly tentative.)

Sedimentation itself is mainly affected by sea level changes establishing different facies conditions from limnic in the Ottnangian over marine during Karpatian and Badenian and back to brackish-limnic in the Sarmatian and Pannonian (Fig. 3.9).

Finally, two major volcanic events took place during basin history, i.e. a first intermediate volcanic phase with heat flow rates of over 300 mW/m² from the Karpatian until Early Badenian and a second basaltic phase from the Pliocene until Pleistocene (Fig. 3.9; Ebner & Sachsenhofer, 1995).

Concerning geothermal exploration, brittle deformed carbonate rocks of the Graz Paleozoic (basement), Karpatian volcanic rocks and coarse clastic rocks of Neogene sedimentary infill, especially Badenian, represent significant aquifers for thermal water resources (Goldbrunner et al., 2010).

4 General Data of the Well ILZ Thermal 1

4.1 Introduction and History

The geothermal well ILZ Thermal 1 (Fig. 4.1) was drilled in the year 1998 by the Austrian drilling company *"Stoffner – Trans Globe Energy GmbH"* in the cadastral community *Dörfl* of the market community Ilz, Styria, Austria. Geological and technical planning and supervision was executed by *"Geoteam – Technisches Büro für Hydrogeologie, Geothermie und Umwelt Ges.m.b.H."* During planning and drilling phases, extensive geoscientific investigations were carried out including deep seismics, geophysical well logging, macro- and microscopic cutting analyses and correlation with vicinal wells (Goldbrunner et al., 2000). First presentation of some data gained through those investigations happened by Scheifinger et al. (1999).

Fig. 4.1: Image showing the well ILZ Thermal 1 (from www.geoteam.at).

Primary goal of the well was the extraction of thermal waters from dolomites of the Paleozoic basement for use in balneology. Drilling began on February 27th, 1998 and was finished on June 27th, 1998 with a final depth of 1,906.0 m. The Paleozoic carbonates were hit at a depth of 1,465 m. First problems arose with a high CO_2 content of waters from the Paleozoic aquifer, which led to carbonate precipitation on the drilling equipment due to pressure drop and degasification (Eisner & Goldbrunner, 1999). A second problem occurred due to enhanced content of ^{226}Ra, reaching the 20 fold of the limit for drinking waters and therefore would have needed to be removed selectively and disposed specially (additional costs) for utilization in balneology. Therefore, the decision to perforate higher horizons with lower mineralization was made (Goldbrunner et al., 2000).

Tab. 4.1 shows an overview of the most important data of the well:

General Data of the Well ILZ Thermal 1	
Location (Fig. 4.2)	
Country	Austria
Province	Styria
Community	Ilz
WGS84-Coordinates	47°5.233' N 15°54.4' E
Altitude	297 m.a.s.l.

Drilling	
Start	27.2.1998
End	27.6.1998
Final Depth	1,906.0 m (Drill bit)
	1,906.8 m (Geophysics)
Company	STOFFNER Trans Globe Energy GmbH
Equipment	IDECO SBS DIR 705 (W 8)
System	Rotary Diesel

Tab. 4.1: Overview of general data of the well ILZ Thermal 1. WGS84 Coordinates according to Google Earth; reference for altitude is the Adriatic sea (modified from Goldbrunner et al., 2000).
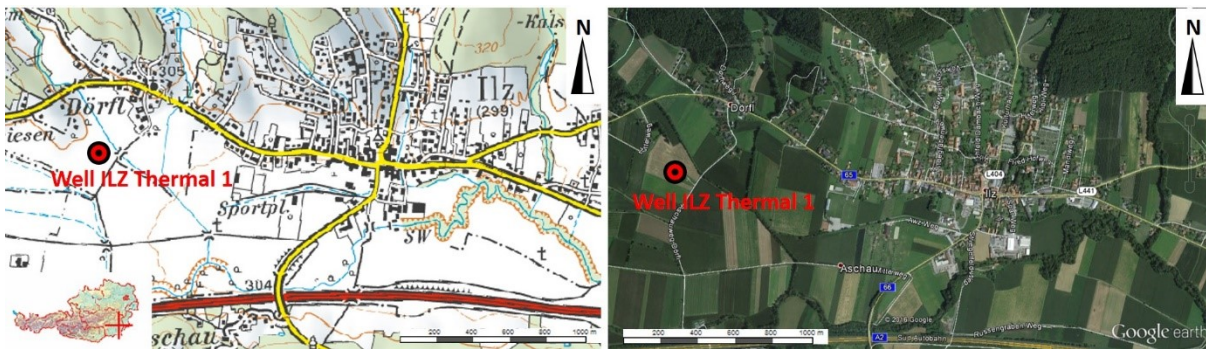

Fig. 4.2: Topographic map (left; www.austrianmap.at) and satellite image (right; Google Earth) with location of the well.

Eventually, due to lack of financial funding, projects for utilization of this geothermal resource were abandoned.

4.2 Technical Drilling Data

The well was drilled after a classical telescoping method in four drilling sections starting from 23'' down to 8 ½'' in the Paleozoic aquifer from 1473.5 – 1,906 m which was left as open hole. The upper three sections were cased with 18 5/8'' – 9 5/8'' pipes, which were cemented in the ring space (Tab. 4.2, Fig. 4.3).

	Depth [m]	Diameter
Drilling	0.0 – 10.0	23''
	10.0 – 392.0	17 ½''
	392.0 – 1,473.5	12 ¼''
	1,473.5 – 1,906.0	8 ½''
Casing	0.0 – 9.5	18 5/8''
	0.0 – 390.6	13 3/8''
	0.0 – 1,469.0	9 5/8''
	1,469.0 – 1,906.0	Open Hole

Tab. 4.2: Compilation of drilling and casing diameters (modified from Eisner & Goldbrunner, 2000).
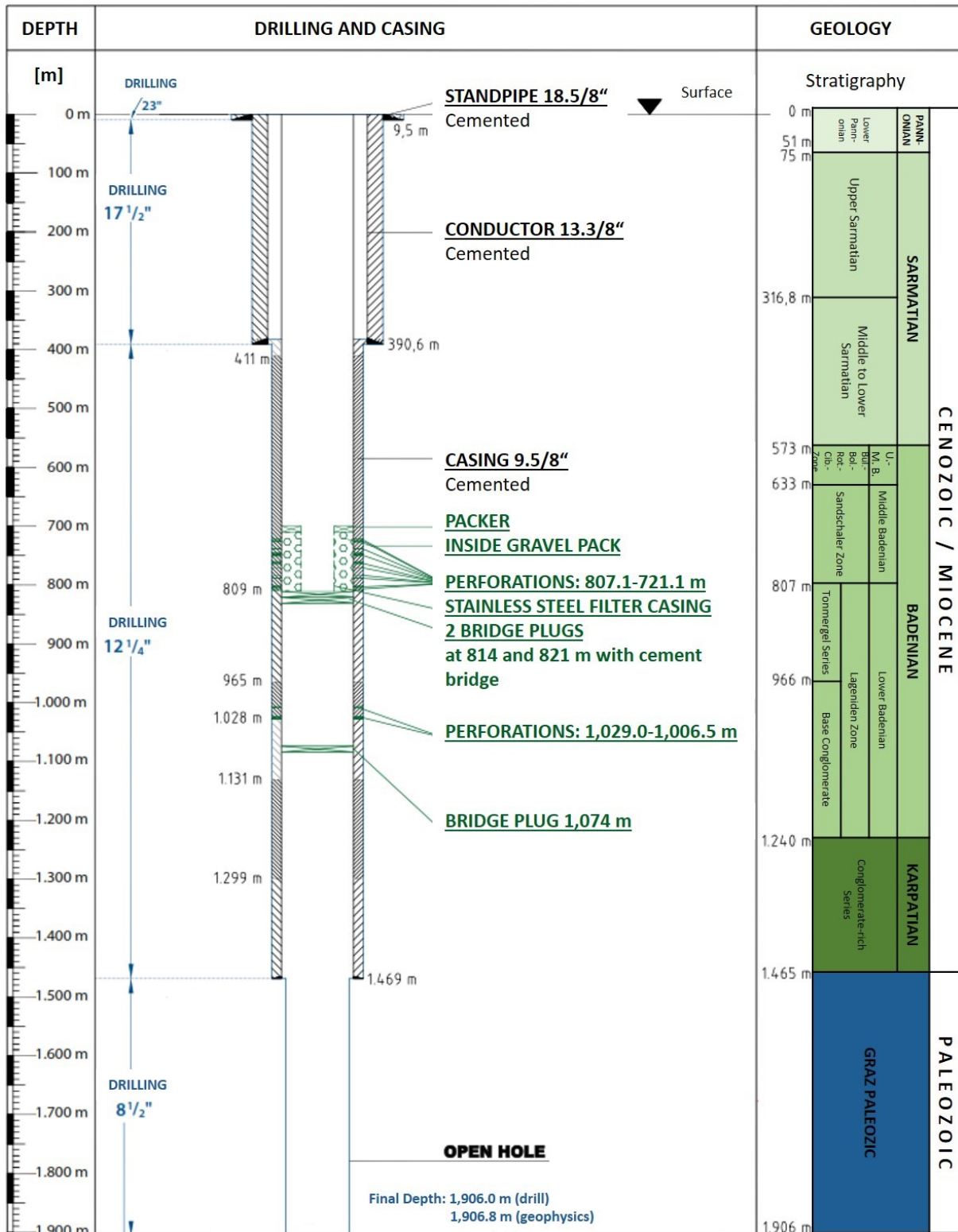
Fig. 4.3: Drilling and development scheme of the well (modified after Goldbrunner et al., 2010).

After the drilling stage, first attempts to recover the water from the Paleozoic aquifer were made but due to the problems described under section 4.1 a bridge plug was set at 1,074 m and potential water-bearing horizons were perforated in the Badenian "Lageniden Zone" between 1,029.0 – 1,006.5 m (cumulative length 9.1 m; Tab. 4.3) with 7'' shots. Due to similar hydrochemistry with the Paleozoic waters, the Lower Badenian waters also were not suitable for utilization and the decision was made to

perforate higher horizons in the Middle Badenian "Sandschaler Zone". Again, a bridge plug was set at 821 m and perforations between 807.1 – 721.1 m with a cumulative perforation length with 23.9 m (Tab. 4.3) were executed with 4 ½" shots (Fig. 4.3; Goldbrunner et al., 2010).

Perforated Horizons	Depth [m]	Perforation Length [m]
Lageniden Zone	1,029.0 – 1,022.9	6.1
	1,009.5 – 1,006.5	3.0
Σ		**9.1**
Sandschaler Zone	807.1 – 806.1	1.0
	804.9 – 801.0	3.9
	789.4 – 787.3	2.1
	784.2 – 783.3	0.9
	770.9 – 770.1	0.8
	763.8 – 760.8	3.0
	750.6 – 745.5	5.1
	739.6 – 737.6	2.0
	727.2 – 724.4	2.8
	723.4 – 721.1	2.3
Σ		**23.9**

Tab. 4.3: Perforation intervals and cumulative perforation lengths for the Lageniden and the Sandschaler Zone (data from Eisner & Goldbrunner, 2000).

The lower mineralized water was confirmed to be suitable for utilization and therefore 4 ½" stainless steel pipes and filter pipes in 5 separate filter lines (F1-F5) with a cumulative length of 63 m (Tab. 4.4) were installed. Additionally, a cement bridge and a second bridge plug at 814 m was placed above the first bridge plug and the ring space along the filter section was filled with an Inside Gravel Pack (grain size: 0.4-0.8 mm). Finally, the section was completed with a stainless steel Packer (Fig. 4.3; Goldbrunner et al., 2010).

Filter Line Nr.	Depth [m]	Filter Length [m]
F1	808.0 – 795.8	12.2
F2	789.7 – 777.5	12.2
F3	771.4 – 759.2	12.2
F4	753.1 – 734.8	18.3
F5	728.6 – 720.5	8.1
Σ		**63**

Tab. 4.4: Filter line intervals for the Sandschaler Zone (data from Eisner & Goldbrunner, 2000).

4.3   Methodology

4.3.1 Geophysical Well Logging

Geophysical well logging measurements were executed in the well ILZ Thermal 1 from March 7th, 1998 until June 28th, 1998 in three separate sections of the well with different logs measured. Tab. 4.5 shows a summary of those measurements representing the base for investigations of this thesis.

SECTION 1	
DEPTH	9.5 – 392 m
LOGGING (7.3.1998)	Gamma Ray Dual Laterolog 4-Arm Caliper Log Deviation/Azimut Log SP Log
SECTION 2	
DEPTH	392 – 1,473.5 m
LOGGING (23.5.1998)	Gamma Ray Dual Laterolog 4-Arm Caliper Log Deviation/Azimut Log
SECTION 3	
DEPTH	1,473.5 – 1,906.0 m
LOGGING (28.6.1998)	Gamma Ray Dual Laterolog 4-Arm Caliperlog Deviation/Azimut Log Compensated Densilog Digital Array Acousticlog Digital Spectralog Simultaneous Acoustic and Resistivity Imaging Log

Tab. 4.5: Compilation of well logging measurements executed in the well ILZ Thermal 1 (modified from Goldbrunner et al., 2000).

Log data were provided by "Geoteam – Technisches Büro für Hydrogeologie, Geothermie und Umwelt Ges.m.b.H.", data preparation was executed with MS Excel and data analysis with the software Interactive Petrophysics 4.2 from LR Senergy.

4.3.2 Cuttings

During drilling, cuttings were taken each 2.5 to 5 m (Goldbrunner et al., 2000). For this thesis, representative cutting samples were only taken from the Paleozoic basement for petrographic analyses including macro- and microscopic description as well as X-ray diffraction. This should give a more detailed insight into lithological features of the basement carbonates for a possible stratigraphic classification and correlation.

Samples were selected according to macroscopic parameters such as color impression, brightness, grain size and grain shape. A more detailed macroscopic description then was made with the help of a 10x magnifying lens and hydrochloric acid (HCl).

Thin sections were produced for 6 samples for a microscopic description, which was executed on an Olympus BX40 microscope in combination with RAMAN spectroscopy at the Department for Resource Mineralogy of the Montanuniversitaet Leoben.

X-ray diffraction was executed on the same 6 samples with a X'Pert³ Powder Diffractometer from Panalytical at the Department for Petroleum Geology at the Montanuniversitaet Leoben. The diffractometer works with a Cu-radiation source and two detectors, i.e. a sealed Xe proportional detector and a X'celerated Scientific RTMS silicon-based detector. For data processing and qualitative as well as quantitative analyses the software package ADEM V6 by Wassermann X-ray analytical equipment was used (http://erdoelgeologie.unileoben.ac.at/).

4.3.3 Hydrogeological/-geochemical Investigations

Data of analyses of the thermal waters from the Paleozoic basement and the Lageniden Zone were provided by Geoteam Ges.m.b.H (Goldbrunner, 2000; Goldbrunner et al., 2010) including main element and isotope analyses, whereas data from the water of the Sandschaler Zone were taken from Arsenal Research (2000). Those include, beside main element and isotopes, also trace element, radioactive and gas analyses.

Data processing and analysis was executed with MS Excel.

5   The Geothermal Environment of the Well ILZ Thermal 1

This chapter presents the results of the investigations executed on the well ILZ Thermal 1 and is subdivided according to the main parameters determining a geothermal system, i.e. reservoir characterization including lithological, pore space and structural analyses, heat conditions with potential heat source and transport and finally characterization of the thermal waters.

The focus of investigations lies on the Paleozoic basement, from which major log data are available and cutting samples were taken for a detailed description. The Neogene sedimentary infill is described only based on log data.

Finally, results are compared with data already available from previous investigations executed by e.g. Scheifinger et al. (1999) or Goldbrunner et al. (2000) and are compiled for a complete characterization of the geothermal environment.

5.1   Reservoir Characterization

For the characterization of reservoir parameters i.e. lithology, porosity, permeability several methods were applied reaching from available borehole geophysical measurements to macro- and microscopic analysis of cuttings and X-ray diffraction. A short overview of important reservoir parameters with analyses executed are given in Tab. 5.1.

Parameter	Logs/Methods
Lithology	Macro- and microscopic description of cuttings Laboratory: X-ray diffraction (XRD) Logs: GammaRay (GR), Photoelectric Factor (PE), Sonic, Density, Spectral GammaRay
Porosity	Logs: Sonic, Density, PE, Dual Laterolog
Permeability/Transmissivity	Logs: Spontaneous Potential (SP), Dual Laterolog Field: Pumping tests

Tab. 5.1: Compilation of logs and methods used for characterization of reservoir parameters.

5.1.1 Neogene Basin Fill (0 – 1,466.0 m)

For lithological characterization of the Neogene sedimentary infill (Karpatian – Pannonian) available GR-, Resistivity- and SP-logs were used in combination of already executed macroscopic cutting analyses from Goldbrunner et al., 2000.

A completion log of the well ILZ Thermal 1 showing GR and resistivity logs with lithological, stratigraphic and hydrogeological results can be found in the appendix (Appendix A). To avoid multiple references in the text this completion log represents the major supplement for this chapter.

For an interpretation and stratigraphic correlation, results were compared with investigations and descriptions derived from literature (e.g. Ebner & Sachsenhofer, 1995; Piller et al., 2004; Gross et al., 2007).

5.1.1.1 General Observations and Calculations

It is known from previous work and from literature, that the Neogene sedimentary infill consists mainly of siliciclastic sediments ranging from shales to gravels/conglomerates with some marly intercalations (Goldbrunner et al., 2000). Therefore, a model was developed, which describes this succession according to two parameters: a) shale content (V_{sh}) derived from the GR-log and b) content of coarse siliciclastics ($1-V_{sh}$).

V_{sh} was calculated from the GR-log according to three different models (Asquith & Krygowski, 2004):

   a. Larionov (1969) for Tertiary rocks:
$$V_{sh} = 0.083 * (2^{3.7*I_{GR}} - 1)$$

   b. Stieber (1970):
$$V_{sh} = \frac{I_{GR}}{3 - 2 * I_{GR}}$$

   c. Clavier et al. (1971):
$$V_{sh} = 1.7 - [3.38 - (I_{GR} - 0.7)^2]^{1/2}$$

Where the Gamma Ray Index (I_{GR}) has to be calculated previously directly from the log:
$$I_{GR} = \frac{GR_{log} - GR_{min}}{GR_{max} - GR_{min}}$$

With: GR_{log} = GammaRay value of the formation from the log
GR_{min} = Minimum GammaRay (of clean sands) from the log

GR_{max} = Maximum GammaRay (of shale) from the log

The final value for V_{sh} used for lithological characterization then was derived from the mean value of $V_{sh, Larionov}$ and $V_{sh, Stieber}$. Lithologies were then classified as shales ($V_{sh} > 0.4$-0.5), sandy shales (0.05-$0.1 < V_{sh} < 0.4$-0.5) and sands/conglomerates ($V_{sh} < 0.05$-0.1).

The value from Clavier et al. (1971) responds only to low GR-values and therefore to low shale content and stays constant at about 0.17 when GR-values exceed about 125 API. Hence, together with the SP-log this was used to identify beds with low shale content and furthermore potential permeable water-bearing horizons.

Porosities (Ø) for those clean sand/gravel beds were calculated from the Dual Laterolog using the Archie (1942) equation (Asquith & Krygowski, 2004):
$$\text{Ø} = (\frac{a * R_w}{R_D})^{1/m}$$

Where: a = tortuosity factor = 0.62 for unconsolidated sands (Humble formula) of Pannonian and Sarmatian sands/gravels; = 0.81 for consolidated sandstones/conglomerates of Badenian to Karpatian;
m = cementation exponent = 2.15 for unconsolidated sands (Humble formula); = 2.0 for consolidated sandstones
R_w = formation water resistivity (Ohmm; section 5.3.4.1)
R_D = deep resistivity reading from Dual Laterolog

Another immediate observation was made concerning the Dual Laterolog compared with the GR-log. Both show an inverse trend, i.e. high GR-values coincide with low resistivity or high conductivity values, respectively. This leads to the assumption, that formation conductivity is mainly controlled by clay minerals/shale content rather than by formation water. This is confirmed especially until the Upper Badenian *"Bolivina-Bulimina/Rotalia-Cibicides Zone"* (571.6 – 637.4m)*,* where deep resistivity (RD) is higher than shallow resistivity (RS) throughout indicating low mineralized waters compared to the drilling mud. Below this zone, RD decreases below RS throughout the rest of the well pointing to higher

mineralization with depth. Exceptions occur in shale-rich zones, where RD and RS become similar due to unability of the drilling mud to infiltrate into the formation.

5.1.1.2 Pannonian (2.5 – 79.0 m)

Lower Pannonian sediments are those which lie on top of the Neogene sedimentary infill and more or less crop out on surface just below 2.5 m thick Quarternary sediments (Goldbrunner et al., 2000). They reach a total thickness of 76.5 m. The dominating lithology in the upper part are shaly sands with a mean shale content of 15% and ranging between 5-23%, whereas several thin (< 1 m) sandy to gravelly intercalations (e.g. at 17.5 m) with potential of drinking water are indicated by the Clavier-value and the SP-log, but are not assigned in the lithology log because of low thickness.

An about 2 m thick shale horizon (V_{sh} = 40-50%) with coal seams occurs at 45 m and is followed by an about 4.5 m thick clean sand/gravel with a shale content even below 1% and hence a great potential for water with a calculated mean porosity of 22.3%.

The lower part again is dominated by shaly sands showing the same characteristics as those in the upper part, whereas shale content increases slightly (fining downward) from around 10% to over 20% and is terminated by a coal bearing horizon. The only interruptions of this trend again are some thin sand to gravel intercalations (e.g. at 63 or 70 m).

The base of the Pannonian and simultaneously the transition to the Sarmatian is formed by an about 3 m thick, clean ($V_{sh} \approx 1\%$), coarse siliciclastic gravel, stratigraphically assigned to the "Mühldorf Gravel" (Stiny, 1918; Winkler, 1927; Winkler-Hermaden & Ritter, 1949). With a mean porosity of 21.7%, this gravel also represents a significant potential aquifer.

5.1.1.3 Sarmatian (79.0 – 571.6 m)

Sarmatian sediments with a total thickness of 492.6 m can be subdivided into an Upper Sarmatian and a Lower to Middle Sarmatian succession. Dominating lithologies as well as sedimentation trends continue from the Pannonian and get even more distinct.

Upper Sarmatian (76.0 – 362.7 m)

Below the "Mühldorf Gravel", Upper Sarmatian deposits start with a 21 m thick succession of shaly sand intercalated with subordinate sandy to gravelly horizons, which can be compared to those of the Pannonian in terms of shale content. This again is terminated by a 1.5 m thick shale with a shale content of nearly 50%.

Those cycles i.e. sand/gravel – shaly sand (± with coarse intercalations) – shale, each with a thickness of approximately 25-30 m continue throughout the Upper Sarmatian and reach their climax in a large cycle starting from about 185-190 m and terminating with the top of the *"Carinthian Gravel"* (Winkler, 1927; Skala, 1967) at 330 m. Major difference between the Upper Sarmatian and Pannonian cycles are the presence of fossils and some low-shale interlayered oolites, especially between 110-130 m and 195-210 m. Coal seams occur in shale-rich zones at 145, 180, 195 and 230 m (Goldbrunner et al., 2000).

Porosities in clean sand/gravel beds also continue from the Pannonian reaching values of 21-22%. Exceptions are formed by the oolitic layers which are similar to the clean sands/gravels in terms of shale content but show a higher resistivity resulting in lower porosities of 13-17%.

Between the small cycles and the large cycle, two sequences with egg-shaped patterns of the GR-log occur from 135-185 m indicating transgressive-regressive cycles and confirming an intensely oscillating

Sarmatian sea level. Those are characterized by a fining downward followed by a coarsening downward succession, i.e. a sand/gravel – shaly sand – shale – shaly sand – sand/gravel.

All those cycles show a distinctive bell-shaped pattern of the GR-log indicating fining downward sequences and also pointing to sea level fluctuations. The large cycle with a total thickness of nearly 150 m mentioned above, as a representative, starts with a 27 m thick, fossil-bearing, succession of coarse sands and gravels with two shaly interlayers. Shale content in those clean sands are in the range of < 1% to max. 5%. This succession is followed by an about 60 m thick shaly sand package with steadily increasing shale content and passes over to a shale with V_{sh} exceeding 50% at 260-275 m and reaching maximum values of 75-77% at 294-300 m. The whole cycle terminates with an abrupt decrease of the shale content to below 10% indicating the 32 m thick basal *"Carinthian Gravel"* of the Upper Sarmatian deposits. This formation is characterized by two about 15 m thick clean sands/gravels with a ± constant shale content ranging between 5-10% separated by a 2 m thin shale layer (V_{sh} up to 61%). The cylinder shaped pattern of the GR-log indicates a fluviatile to beach sand depositional environment. Porosities range between 19 and 21% and hence, those gravels also represent major potential water-bearing horizons.

Further aquifers occur at the top of the large cycle between 185-212 m as well as the sands/gravels separating the two egg-shaped successions at 150-155 m with a cumulative thickness of 62 m.

Lower to Middle Sarmatian (362.7 – 571.6 m)

Lower to Middle Sarmatian deposits start with a silty to sandy dominated succession ($V_{sh} \approx$ 10%) with some interlayered shaly and coaly horizons. Due to high shale content, calculated porosities are not representative but are assumed to be in the same range as Upper Sarmatian deposits and therefore could represent potential aquifers. From a depth of 422.5 m shale content increases steadily to over 40% in another fining downward pattern with coarse intercalations to be terminated by a 10 m thick silty to sandy bed.

From that downward, Lower Sarmatian sediments are characterized by an interlayering of shales and fine sands. At the base between 546 and 571.6 m a package of four sandy/gravelly beds with thicknesses of 2.5-5 m each separated by thin shales is indicated by the cylinder shaped pattern of the GR-log and hence point to a fluviatile or beach sand depositional environment and therefore a sea level low stand. They already show an advanced degree of consolidation to sandstones/conglomerates and could represent horizons with good aquifer properties.

5.1.1.4 Badenian (571.6 – 1,240.0 m)

Badenian sediments reach a total thickness of nearly 670 m and can be subdivided into an Upper, Middle and Lower Badenian succession. The Upper Badenian shale-rich *"Bulimina-Bolivina/Rotalia-Cibicides Zone"* can be seen as a major impermeable separating horizon between the overlying Sarmatian and Pannonian sediments and all underlying formations in terms of water mineralization, what can be observed in the Dual Laterolog. This zone is followed by the Middle Badenian coarse clastic *"Sandschaler Zone"* representing a major aquifer for geothermal exploration (see section 4.2). The Lower Badenian *"Lageniden Zone"* is subdivided into the upper shale dominated *"Tonmergel Series"*, which separates the aquifers of the overlying *"Sandschaler Zone"* from the aquifers of the lower *"Base Conglomerate"*.

The Styrian Unconformity, which separates the Badenian and Karpatian sediments cannot be identified from the logs and only poorly from cuttings but is revealed by seismics.

Upper Badenian

Bulimina-Bolivina/Rotalia-Cibicides Zone (571.6 – 637.4 m)

This zone is lithologically dominated by shaly to fine sandy marls with a mean shale content of 30-40% throughout. One major coarser intercalation occurs from 605-608 m, where shale content decreases to about 10% in a fining upward pattern indicating a marine transgression. Further minor intercalations also occur in the upper part but are not indicated in the log because of low significance. Those intercalations are composed of mainly quartz sand/gravel with minor dark siltstone and pyrite (Goldbrunner et al., 2000). In the lower part coarse intercalations decrease and shaly to fine sandy marls are developed throughout.

Middle Badenian

Sandschaler Zone (637.4 – 807.3 m)

Compared to the Upper Badenian, the Middle Badenian *"Sandschaler Zone"* shows a much coarser development comprising mainly silty to fine gravelly sandstones with some thin shaly to marly intercalations.

The succession starts with two egg-shaped transgressive-regressive cycles from 650-702 m with transitions from coarse sandstones ($V_{sh} \approx$ 5-10%) representing potential water bearing horizons to shales and marls (V_{sh} up to 50%) which form the major fine intercalations in the whole Middle Badenian.

Below those two cycles, the *"Sandschaler Zone"* is dominated by an interlayering between mainly coarse and minor fine silty to shaly sandstones and marls. Minimum shale contents are about 5-10% in the coarse sandstones and reach average maximal values of 30-40% in the shaly sands. In the upper part, between 702 and 750 m, of the succession several potential aquifers with thicknesses of up to 10 m and porosities of around 22-25% occur, whereas the lower part, from 750-807.3 m the shale content increases resulting in a dominance of shaly sands with thin coarse intercalations.

The potential aquifers identified between 702 and 807.3 m by log analysis are those, which were perforated for geothermal production when the well was completed (see section 4.2).

Lower Badenian – Lageniden Zone

„Tonmergel" Series (807.3 – 966.1 m)

The *"Tonmergel Series",* as the name already proposes, is dominated by highly consolidated shaly to silty marls with few intercalations of coarse sandstones to conglomerates (e.g. at 807 or 847.5 m), especially in the upper shale rich part (807.3 – 868.0 m), where the mean shale content is about 43% but maximal values of over 80% are reached.

This upper part is followed by an about 35 m thick package of shaly sand, where average V_{sh} decreases to 31%. Few coarse intercalations are indicated by lower GR values and spikes in the Dual Laterolog.

In the lower part, mean shale content increases again to 40%, whereas coarse intercalations cannot be observed largely.

In conclusion, the *"Tonmergel Series"*, similar to the Upper Badenian *"Bulimina-Bolivina/Rotalia-Cibicides Zone"*, can be seen as an impermeable separating horizon between the waters of the overlying *"Sandschaler Zone"* and the underlying *"Base Conglomerate"*.

Base Conglomerate (966.1 – 1,240.0 m)

The start of the *"Base Conglomerate"* is indicated by a sharp increase in resistivity and an immediate decrease of the GR and therefore shale content to 5-7% at a depth of 975 m. From that downward, the upper part of the succession consists of mainly shaly to silty sands and marls with coarse sandy to conglomeratic intercalations. A first major 29 m thick coarse horizon with water potential occurs from 1,018 – 1,037 m, which was also perforated for geothermal production during completion of the well (see section 4.2). With an average shale content in this horizon of 6.2% and even dropping below 5%, an average porosity of 11.4% was calculated using the Archie equation. Probably the real porosity is a little bit lower because of overestimation due to the shale content. Major components of the partly well rounded conglomerates are grey dolomite and quartz gravels (Goldbrunner et al., 2000).

This aquifer is underlain by an about 2 m thin shaly marl acting as an impermeable bottom layer and is followed by a thicker shaly sand. Below this package from approximately 1,057 m downward, the rest of the *"Base Conglomerate"* is dominated by coarse sandstones to conglomerates with some intercalating silty to shaly marls with thicknesses of a few meters. Those even get less towards the base. Major intercalations with shale contents above 60% and higher are indicated by peaks in the GR-log and occur at 1,100, 1,113 and around 1,150 m.

The conglomerates of this lower part show more or less constant shale content with a mean value of 12.2% and an average porosity of 15.7%, what again is thought to be slightly overestimated. Nevertheless, they represent extensive potential aquifers. Cuttings reveal, that dolomitic components decrease in those conglomerates and are replaced by crystalline parts such as mica and sericite schists and gneiss, apart from quartz (Goldbrunner et al., 2000).

5.1.1.5 Karpatian (1,240.0 – 1,466.0 m)

The transition from the Badenian "Base Conglomerate" to the Karpatian "Conglomerate-rich Series" cannot be identified from the logs but slightly from an increase of carbonate components and the occurrence of red sandstones from the cuttings (Goldbrunner et al., 2000). Furthermore, a N-S reflection seismic section (IL9301) reveals the location of the Styrian Unconformity, which separates the Karpatian from the Badenian.

The development of the Karpatian succession is dominated by coarse conglomerates with slightly varying shale content indicated by variations in the GR-log. Based on this variations, the whole Karpatian can be subdivided into 4 sub-successions:

a)   *Upper shaly conglomerates (1,240.0 – 1,300.0 m)*

Those slightly silty to shaly conglomerates show a constant average shale content of 12.4% and a calculated porosity of 17.2%.

A thin shale horizon with very high gamma radiation occurs at 1,273.0 – 1,274.5 m, which can be correlated with a bentonite bed of the adjacent well Blumau 2 (Goldbrunner et al., 2000).

b)   *Upper clean conglomerates (1,300.0 – 1,353.0 m)*

At a depth of about 1,300.0 m, gamma radiation decreases slightly resulting in a constant lower shale content until a depth of about 1,353.0 m. V_{sh} decreases to an average of 8.5% with a porosity of 16.0%.

c)   *Shaly sands succession (1,353.0 – 1,395.0 m)*

This succession is characterized by an intensely varying gamma radiation. A first thick shaly sand (V_{sh} = 15-20%) package is terminated by an approximately 2 m thin shale horizon with high radiation and shale content at 1,372-1,374 m.

Below this shale, an alternating sequence of 2 clean ($V_{sh} \approx$ 5-10%) and shaly ($V_{sh} \approx$ 15-20%) sandstones/ conglomerates is indicated by the oscillating GR-log. Porosity in the clean sand horizons is about 15%.

d) *Lower clean conglomerates (1,395.0 – 1,457.0 m)*

From 1,395.0 m downward a more or less constant low gamma radiation indicates clean conglomerates throughout. Average shale content is with 5.7% even lower than in the upper clean conglomerates and porosity was calculated to be 15.1%.

Those lower conglomerates are distinctively characterized by a red coloration (Tab. 5.4) due to a very fine grained matrix. Main components are grey, white and pink carbonates with subordinate quartz and mica. Towards the base the red coloration decreases and the amount of grey dolomitic components increases already indicating the Paleozoic basement.

As a conclusion, the whole Karpatian *"Conglomerate-rich Series"*, with few exceptions in the shaly sands succession, represents a major potential aquifer with porosities ranging around 15%.

5.1.2 Paleozoic Basement (1,466.0 – 1,906.0 m/Final Depth)

The basement of the well ILZ Thermal 1 starts at 1,466.0 m and can be followed until the final depth of the well to 1,906.0 m, making a total thickness of 440 m. It consists mainly of carbonates, which can be accounted stratigraphically to the Graz Paleozoic.

For first lithological characterizations, well logs including GR, spectral GR, PE, density, sonic and resistivity logs were used (Appendix A, B). Based on well logs and on cutting analyses, the basement can be subdivided into three large units:

  I.   Upper light to dark grey dolomites and marls (1,466.0 – 1,666.0 m)
  II.   Phyllitic and faulted zone (1,666.0 – 1,702.3 m)
  III. Lower dark grey dolomites (1,702.3 – 1,906.0 m)

For a more detailed description of the lithologies, representative cutting samples were taken for the lower Karpatian and for the whole Paleozoic basement and described macroscopically as well as microscopically and with XRD, especially for the separating phyllitic/faulted zone.

Concerning pore structure (total and fracture porosity) and hydraulic conductivity with transmissivity analyses of the zones, again well logs and cuttings in combination with models derived from literature were used.

5.1.2.1 Separate Analyses of PE-, Density- and (spectral) GR-log

The PE-, density-, and (spectral) GR-log were considered separately to get an overview of present and dominating lithologies. For comparison, literature values of significant minerals and water are given in Tab. 5.3.

i.   *PE – log:*

Especially the PE-log gives representative indications, because it is more or less not influenced by porosity but strongly influenced by mineralogy. Values vary between a minimum of about 2.1 b/e and a maximum of about 4.2 b/e, whereas the mean value lies at about 3.1 b/e. The distribution is shown in the histogram in Fig. 5.1 and shows that the majority of all values ranges around the mean value indicating dolomite as the dominating lithology.
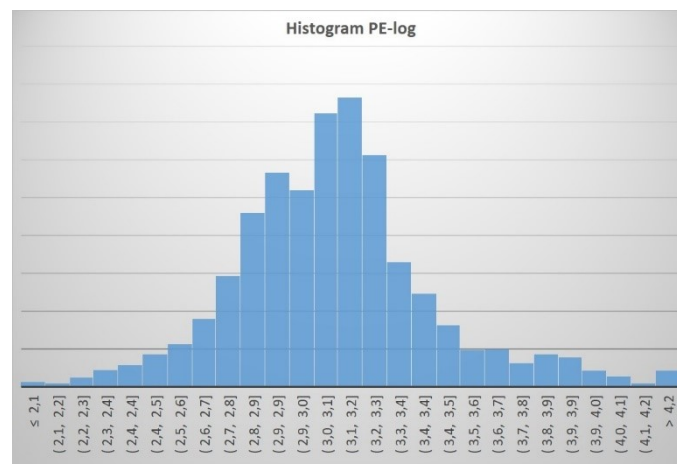
Fig. 5.1: Histogram of the whole PE-log (b/e) showing majority of the values between 3.0 b/e and 3.2 b/e.

A second high value around 2.9 b/e points to an abundance of alkali-feldspars or a mixture of dolomite with phases of a lower Photoelectric Factor (PEF) such as quartz, mica or even water. Considering the distributions for the three units mentioned before separately, it is confirmed that dolomite is the dominating lithology for the upper and the lower unit, whereas for the phyllitic/faulted zone higher PEFs are reached (Fig. 5.2).
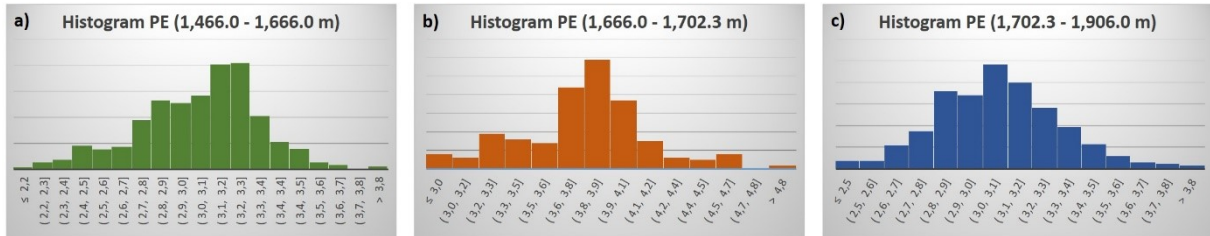
Fig. 5.2: Separate PE-log (b/e) histograms for a) upper light to dark grey dolomites and marls, b) phyllitic/faulted zone and c) lower dark grey dolomites.

The higher PEFs in the phyllitic/faulted zone again point to an abundance of minerals with PEFs around 3.6 b/e – 4.0 b/e or a mixture of phases. However, it is obvious that lithology changes significantly between 1,666.0 and 1,702.3 m.

ii.   Density – log:

The same trends are observed considering the distribution of the density-log (Fig. 5.3). The majority of values range between 2.78 g/cm³ and 2.82 g/cm³, which again indicates a dominance of dolomite. Because of the higher sensitivity of the density to porosity, the presence of water results in slightly lower values than the 2.87 g/cm³ indicated in literature (Tab. 5.3).
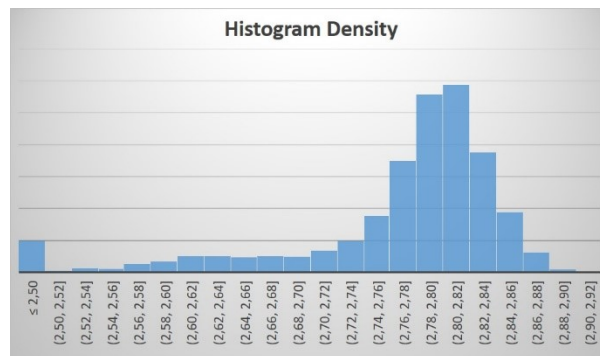
Fig. 5.3: Frequency distribution of density values (g/cm³) for the whole basement.

If the three units are analyzed separately again, the lithology change from the PE-log is confirmed and even gives a more concrete idea of the lithology dominating. In the upper and lower units again values range around 2.80 g/cm³, whereas in the phyllitic/faulted zone the density decreases to 2.62 – 2.66 g/cm³, indicating the abundance of minerals like quartz, feldspars or illite. A second high at 2.72 – 2.74 g/cm³ points to higher ratio of calcite (Fig. 5.4).
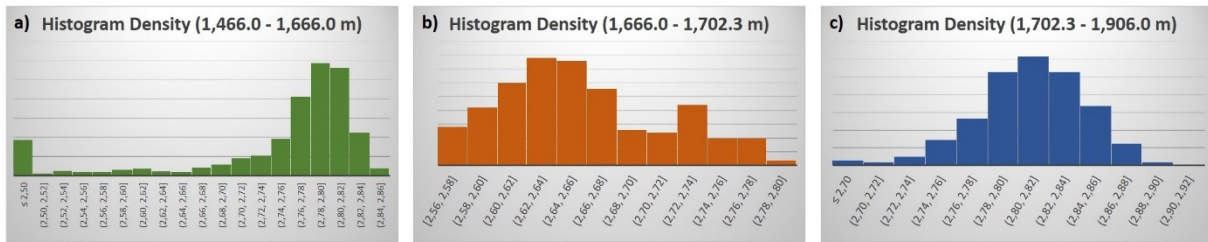
Fig. 5.4: Density (g/cm³) histograms for a) light to dark grey dolomites and marls, b) phyllitc/faulted zone and c) lower dark grey dolomites.

Low values (≤ 2.50 g/cm³) only occur in the upper light to dark grey dolomites and can be referred to the low density/high porosity zone from 1,510 – 1,540 m.

iii.   *GR – log:*

A further hint for lithological characterization especially for the phyllitic/faulted zone gives the GR-log.

In the upper light to dark grey dolomites and marls, GR-radiation in general stays constantly low with a mean value of 44 API-units. Zones with slightly higher radiation (≈ 80 API) can only be observed between 1,520 and 1,540 m and at an about 2 m thin horizon at 1,582 – 1,584 m (Fig. 5.5 a). Towards the base radiation also increases slightly with values reaching 60 API-units. The result of this trend is a low shale content below 10%, with an average of 5.6%. In the zones with higher radiation shale content increases to about 12-14% and therefore were interpreted as marls (Fig. 5.5 d).
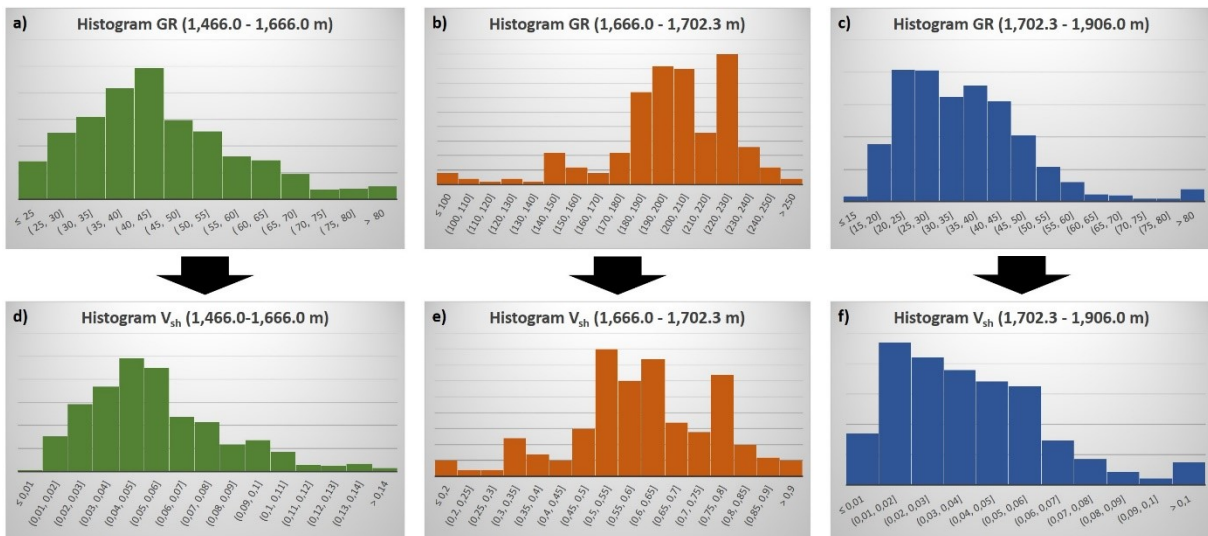
Fig. 5.5: Frequency distribution of GR-values (API-units, a-c) and shale content (V_{sh}, d-f) for the upper light to dark grey dolomites and marls (a, d), phyllitic/faulted zone (b, e) and the lower dark grey dolomites (c, f).

At about 1,666 m a sudden strong increase in GR-radiation to over 200 API-units and indicates the lithological change to a zone with very high shale content or a zone with high abundance of K-, Th- and U-bearing phases. The high in the distribution of GR-values between 220 and 230 API-units points to an abundance of K-feldspar, whereas slightly lower values between 180-210 API-units probably again indicates a mixture of phases including dominance of high GR-minerals like feldspar, illite, mica with some low GR-minerals like dolomite, calcite and quartz (Fig. 5.5 b). The high gamma radiation results

in very high shale contents of even more than 90% in some sections but with an average of 60% (Fig. 5.5 e).

For the lower dark grey dolomites, gamma radiation decreases again suddenly at about 1,702.5 m to values even below those of the upper dolomites ranging between 20 to 40 API-units (Fig. 5.5 c). This also indicates a very low shale content throughout the whole lower zone. The average shale content was calculated to 3.9%. The only exceptions form two thin beds with elevated shale content at a) 1,727-1,732 m with V_{sh} reaching 18% and b) 1,811-1,813 m with V_{sh} reaching 26%. Beside those two marly intercalations, the lower zone therefore is thought to be formed of more or less clean dolomites.

iv.   *Spectral GR – log:*

The spectral GR-log was then used for a more accurate lithological description in terms of mineralogy and depositional environment, especially of the phyllitic/faulted zone. The spectral GR-log measures the contributions of radiation coming from potassium (K in %), thorium (Th in ppm) and uranium (U in ppm) decays to total gamma radiation separately. Therefore, lithologies and especially minerals containing those can be identified. Furthermore, they can be indicators of the depositional environment of sedimentary rocks.

K typically is incorporated in clay minerals, K-feldspars, mica and evaporates (Tab. 5.2; Schön, 2015) and is thought to originate from erosion and further can be reworked and transported for long distances (Baker Atlas, 1985). Th is a very stable element and will not be dissolved and is incorporated in acid to intermediate rocks. It is deposited only with detrital sediments, where it is adsorbed by clay and heavy minerals and never with chemical sediments (e.g. carbonates) due to alteration. Therefore, Th is an important clay indicator in carbonate reservoirs (Schön, 2004) and is also assumed to be a marine element (Baker Atlas, 1985). U also is high in acid rocks with an average of 4.65 ppm but unlike Th it is unstable and forms soluble salts which can be transported due to weathering and alteration. Those can then be incorporated into sediments in three ways (Schön, 2004):

- Precipitation in a reducing environment (pH = 2.5-4.0) in stagnant, anoxic waters forming black shales or "radioactive carbonates" (Baker Atlas, 1985).
- Adsorption by organic matter
- Chemical reaction in phosphorites

	K [%]	U [ppm]	Th [ppm]
Orthoclase	11.8-14.0	0.2-3.0	0.01-7.0
Microcline	10.9	0.2-3.0	0.01-7.0
Muscovite	7.8-9.8	2-8	0-25
Illite	3.5-8.3	1-5	10-25

Tab. 5.2: K-, Th- and U-content of some important minerals for this study. After Schön (2004); data from Baker Atlas (1985); Schlumberger (1982) and Hurst (1990).

A summary of trends concerning K-, Th- and U-content distribution in carbonate rocks with their potential to act as indicators for depositional environment is shown in Fig. 5.6.
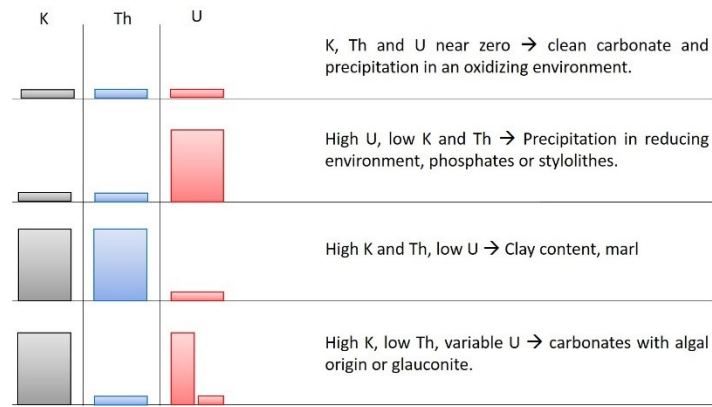
Fig. 5.6: General trends for K-, Th- and U-content distribution in carbonate sediments and their potential indication towards depositional environment. Modified after Schlumberger (1982).

In the Paleozoic basement of the well ILZ Thermal 1 several changes in K-, Th- and U-content distribution can be observed. In the upper part of the upper zone, all three stay low until a depth of about 1,518.5 m with average contents K = 0.86%, U = 3.02 ppm and Th = 3.04 ppm. Because Th content generally can increase to higher values than U (Tab. 5.2), U content can already be seen as slightly enhanced. From 1,518.5 until about 1,536 m an increase of K and Th to 1.6% and 6.75 ppm, respectively together with a slight decrease of U to 2.70 ppm indicates higher clay content and marl. In the lower part of the upper zone until 1,666.0 m, K and Th again decrease to 0.65%/2.5 ppm and stay more or less constant with some fluctuations. U-content, on the other side, first increases downward with maximum values of up to 9 ppm at 1,583.5 m which is followed by a lower U zone with an average of 2.6 ppm. A sudden increase at 1,600 m to 6.5 ppm is then followed by a decreasing downward until 1,655 m. Although fluctuating but this enhanced U-content throughout points to the deposition of the carbonates in a reducing environment, which is confirmed by the high abundance of pyrite found in cuttings.
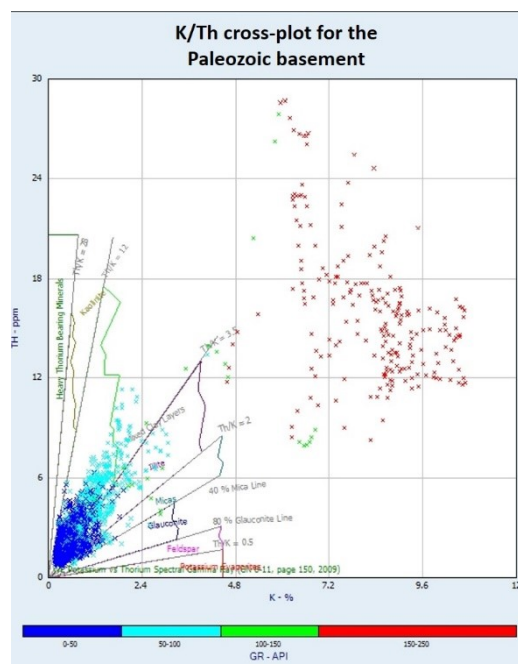
Fig. 5.7: K/Th cross-plot for identification of mineral phases. Red points are those from the high GR phyllitic/faulted zone.

The phyllitic/faulted zone (1,666.0 – 1,703.2 m) is characterized by a strong increase of K and Th to average contents of 8.1% K and 15.8 ppm Th. U-content is with an average of 3.15 ppm comparatively low and therefore again high clay content and marls can be interpreted for this zone from the spectral GR-log. K/Th ratios were be used in a cross-plot for potential identification of K- and Th-bearing mineral phases. Fig. 5.7 shows the K/Th cross-plot for the whole Paleozoic basement, whereas blue and turquoise points represent the upper and lower dolomites with low gamma radiation and the green to mainly red points represent the high GR phyllitic zone.

Th/K ratios range between 1 and 6.3 with an average of 2.15 indicating the dominance of mainly mica and illite with probably subordinate mixed layers and glauconite for K- and Th-bearing minerals.

In the lower dark dolomites, a similar distribution as in the lower part of the upper zone with low K- and Th-contents and varying U-content is reached. Until a depth of about 1,733 m, K and Th vary stronger before they get constant and low until 1,810 m. From there downwards a stronger fluctuation is observed again, but all in all K- and Th-content stays low at average values of 0.5% and 2.0 ppm, respectively. U-content varies strongly throughout the whole lower zone with peak values of up to 7 ppm and a mean value of 2.8 ppm in the upper part. U-peaks together with the constantly low K- and Th-content again indicates deposition in a reducing environment. A 2 m thick horizon, from 1,811.5 – 1,813.5 m with very high U- (13.5 ppm) and a comparatively enhanced K-content (2.9%) might indicate the abundance of glauconite or organic matter. In the lowest part U also fluctuates strongly between 2 and 6 ppm.

As a short conclusion, comparatively high U-contents together with low K- and Th-contents in the upper light to dark grey dolomites and marls and the lower dark grey dolomites point to a deposition of those carbonates in a reducing environment. The strong increase of K and Th in the phyllitic/faulted zone indicates high clay content what is confirmed by the K/Th cross-plot identifying mica and illite as the dominating phases creating the radiation from K and Th.

5.1.2.2 Combined Analysis of PE- and Density-log

<u>Calculations</u>

It was known/assumed from previous studies (e.g. Scheifinger et al., 1999; Goldbrunner et al., 2000), that main lithologies forming the basement are dolomites with calcite fracture fillings apart from the phyllitic/faulted zone. Together with shale, dolomite, calcite and pore space this creates a model describing the basement consisting of four components. Shale content was calculated according to the same models already used for the Neogene basin fill described in section 5.1.1.1. For the remaining three components, a combined quantitative analysis for estimation of percentage of dolomite, calcite and porosity was executed using the PE and density log, whereas the volumetric photoelectric cross section U (b/cm³) must be applied (Schön, 2011):

$$U_{log} = U_{dol} * V_{dol} + U_{cal} * V_{cal} + U_{water} * \emptyset$$

$$\rho_{log} = \rho_{dol} * V_{dol} + \rho_{cal} * V_{cal} + \rho_{water} * \emptyset$$

Where: U = PE * ρ_e; ρ_e = electron density ≈ ρ_{log}, ρ_{dol}, ρ_{cal}, ρ_{water} according to data from Baker Atlas (1985) and Schlumberger (2000) in Schön (2011).
PE$_{log}$, ρ_{log} = PE and density of formation (reading from log)
PE$_{dol}$, PE$_{cal}$, PE$_{water}$, ρ_{dol}, ρ_{cal}, ρ_{water} = PE and density values for dolomite, calcite and water from literature and water analysis (Tab. 5.3)
V$_{dol}$, V$_{cal}$ = fraction of dolomite and calcite
$\emptyset$ = porosity

Those two equations together with the balancing equation

$$1 = V_{dol} + V_{cal} + \emptyset$$

form an equation system, where the three unknowns V_{dol}, V_{cal} and $\emptyset$ can be determined. The solution of the system can either be executed graphically via cross-plots or numerical. After numerical solution for dolomite, calcite and porosity, shale content (V_{sh}) was added and recalculated to 100%.

Both methods were applied for lithological analyses and results are presented in the following.

	PE (b/e)	ρ (g/cm³)	GR (API)	Δt (μs/m)
Quartz	1.81	2.65	0	167
Orthoclase	2.86	2.56	≈ 220	226
Microcline	2.86	2.59	≈ 220	
Albite	1.68	2.62	0	161
Anorthite	3.13	2.76	0	148
Muscovite	2.40	2.83	≈ 270	154-161
Illite	3.45	2.64	250 – 300	211*
Dolomite	3.14	2.87	0	138-144
Calcite	5.08	2.71	0	151-161
(Salt) Water	0.36	Section 5.3.4.2		616*

*Tab. 5.3: Some physical properties for important rock-forming and for this study significant minerals and water used for numerical solution of the equation system and lithological interpretation (modified from Schön, 2011; data after Baker Atlas, 1985; Schlumberger, 2000). For water density see reference. *) Values from www.spec2000.net/12-phidt.htm.*

Numerical solution

Numerical solution of the system was used to construct a lithology log, which is shown in the logs in the appendix. For the upper light to dark grey dolomites and marls, dolomite is again confirmed to be the dominating lithology with an average ratio of 81%. Calcite makes about 8.2% and with the average shale content from 3-6% (Fig. 5.5 d), 5-8% remain for porosity. The zone between 1,510-1,540 m is the only deviation from this trend, where dolomite content decreases slightly to 73.4%, shale content increases to over 10% and porosity also increases slightly to an average of 7.5% but can reach maximal values of over 20% at 1,526 m.

From 1,666-1,703.2 m in the phyllitic/faulted zone, dolomite decreases strongly to about 22% due to the sudden increase in shale and even decreases relative to calcite, which increases to an average of 15%. Porosity also decreases to 3%, whereas in the hanging part at the transition from the upper dolomites and marls to the phyllitic/faulted zone, a zone of higher porosity (≈ 10%) is observed.

The lower dark grey dolomites, are again dominated by 85.3% of dolomite against 7.4% of calcite and 4% of shale. Therefore, porosity is very low with an average of 3.3%. Exceptions from this trend again form the two thin marly intercalations at 1,730 and 1,812 m.

Graphical solution

Graphical solution is shown in Fig. 5.8 and shows the same trends as described above. Dominating lithology is dolomite with porosities ranging between 0 and 10%. Only a few exceptions, where porosity rises to over 20% can be accounted to the high porosity zone at 1,526 m. Even higher values (up to 40%) are interpreted as outliers.
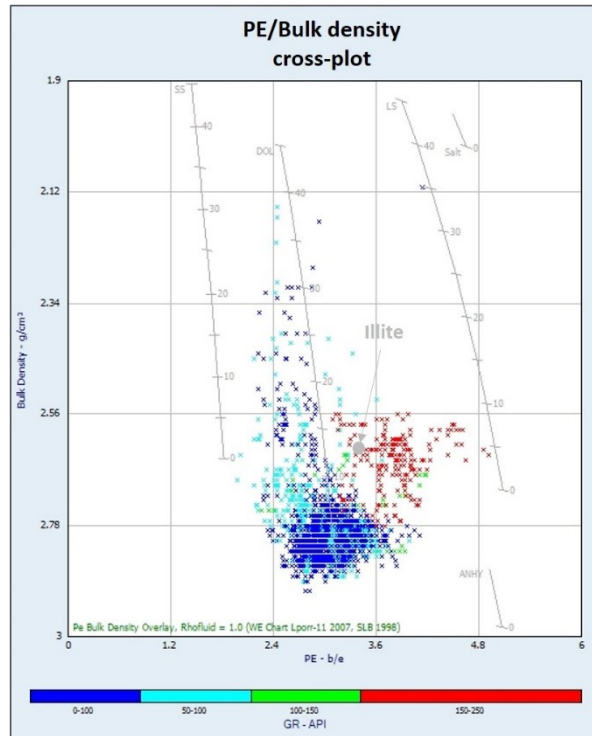
Fig. 5.8: PE/Bulk density cross-plot for graphical solution of combined lithological analyses. Red points represent phyllitic/faulted zone (SS=sandstone, DOL=dolomite, LS=limestone, ANHY=anhydrite).

Points of the phyllitic/faulted zone, indicated by high gamma radiation (red), show a trend towards higher PE and lower bulk density. Some nearly reach the limestone (LS) line which confirms the higher percentage of calcite. Apart from that, the theoretical location of illite is also indicated in the diagram and also confirms the abundance of illitic material in this zone.

5.1.2.3 Cuttings Analyses

Representative cutting samples were taken for the whole basement and lithologies where subdivided according to macroscopic parameters like color and grain size. Macroscopic descriptions of the samples are shown in Tab. 5.4 together with images and depths. For scale, the black line in the images is 2 cm.

	Depth [m]	Image	Macroscopic Description
Karpatian	- 1,466.0		Coarse sandy to fine gravelly dominantly red carbonates showing strong HCl-reaction and subordinate grey dolomites with calcitic joint fillings. Abundant crystalline components from mica schist including mainly quartz and muscovite.
UPPER LIGHT TO DARK GREY DOLOMITES AND MARLS	1,466.0 – 1,472.5		Coarse sandy to medium gravelly light to medium grey dolomites and white calcites with reduced ratio of red carbonates but still abundance of crystalline components. Red oxidation of components suggests Fe-content.
	1,475.0 – 1,500.0		Medium to coarse sandy, light grey, splintered dolomites and fine to medium gravelly white marly components. No red and crystalline components but strong increase of oxidized components and even abundance of pyrite.
	1,502.5 – 1,515.0		Coarse sandy to fine gravelly, light to medium grey, granular dolomites and white calcites. Abundance of brecciated components with dolomitic clasts in a fine grained marly ground mass.
	1,517.5 – 1,520.0		Coarse sandy to fine gravelly dark grey dolomites. Slightly greenish to black color impression suggests abundance of chlorite and other clay minerals. Those also contain small red grains with metallic luster which were identified as rutile with RAMAN.
	1,522.5 – 1,550.0		Medium to coarse sandy, medium grey, splintered and granular dolomites with some oxidation and abundance of pyrite.
	1,540.0		Comparable to 1,571.5-1,520.0 but much finer and splintered throughout, what suggests high clay minerals content.

UPPER LIGHT TO DARK GREY DOLOMITES AND MARLS	1,552.5 – 1572.5		Coarse sandy to fine gravelly, very dark, granular dolomites with calcite joints and some oxidation.
	1,575 – 1,595		Medium to coarse sandy, medium grey, splintered and granular dolomites with brecciated components and some oxidation.
	1,582.5		Medium to coarse sandy, black to greenish, splintered components similar to 1,517.5-1,520.0. Oxidation, pyrite and rutile observable.
	1,597.5 – 1,602.5		Coarse sandy to fine gravelly, medium grey, granular dolomites with brecciated components.
	1,605.0 – 1,642.5		Coarse sandy to medium gravelly, dark grey, granular and clean dolomites with calcite joints.
	1,645.0 – 1,665.0		Medium to coarse sandy, light grey, splintered dolomites with abundance of pyrite and rutile suggesting clay content.
PHYLLITC/FAULTED ZONE	1,665.0 – 1,702.5		Medium sandy, light grey, splintered and granular dolomites with very fine components of phyllitic and probably crystalline phases.
	1,672.5		Coarse sandy to fine gravelly, medium grey, granular dolomites. Content of light splintered components lower.

	1,690.0 – 1,697.5		Medium to coarse sandy, light to medium grey, splintered and granular dolomites and subordinate calcite. Abundance of pyrite and rutile again suggests clay content.
LOWER DARK GREY DOLOMTIES	1,705.0 – 1,737.5		Fine to medium sandy, light grey and dominantly splintered dolomites. High abundance of very fine components indicates clay or marl.
	1,740.0 – 1,790.0		Dominantly fine gravelly medium to dark grey, clean dolomites, getting darker towards base. Content of brecciated components also increases.
	1,792.5		Fine to medium gravelly, light to medium grey, clean dolomites with very high content of brecciated components.
	1,795.0 – 1852.5		Dominantly fine gravelly, medium to dark grey, clean dolomites with still increasing ratio of breccias.
	1,855.0 – 1,905.0		Fine to medium gravelly, dark grey, clean dolomites with very high content of brecciated components.

Tab. 5.4: Macroscopic descriptions of cuttings with images and depths (black lines in images are 2 cm).

Microscopic and XRD investigations of the phyllitic/faulted zone

Because of lithological uncertainties concerning the phyllitic/faulted zone due to heterogeneity and partially very fine grain sizes, thin sections and X-ray diffraction analyses were executed for the samples at 1,672.5, 1,687.5 and 1,697.5 m. For a reference the same was also executed on a clean dark dolomite sample from 1,635.0 m.

i.   ILZ 1,635:

The microphotographs in Fig. 5.9 show the clean massive dolomites with xenomorph grains and grain sizes of a few tenth of millimeters. In most grains, cleavage is well visible and opaque phases are pyrite throughout (Fig. 5.9 a). Breccia content in this sample is very low but is shown here representatively for the lower zone, where brecciated components have the same development but much higher ratio.

Those breccias consist of dolomite clasts (light grey) of up to 1 mm in a very fine grained medium to dark grey marly ground mass, which cannot be resolved more detailed.
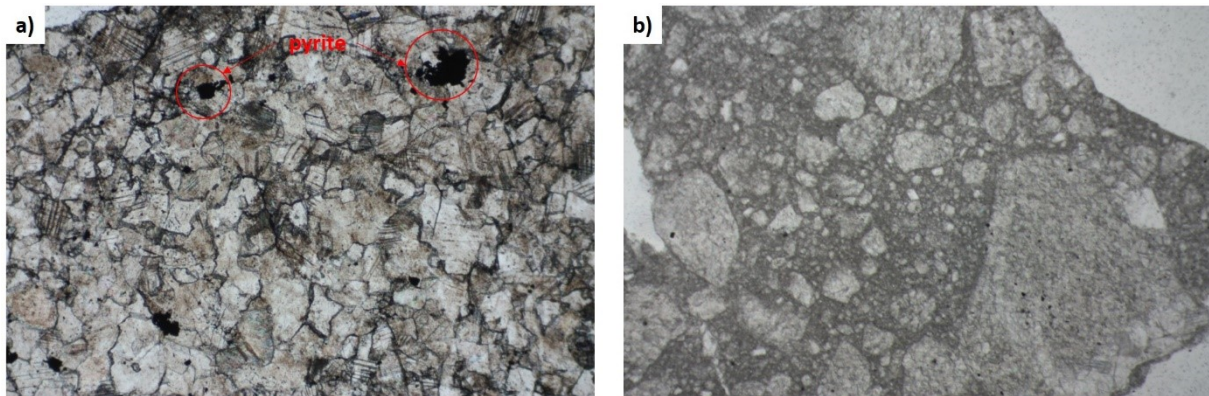

Fig. 5.9: Microphotographs of clean dolomite with some pyrite (a) and breccia (b) from the sample at 1,635 m. Image lengths are 2 mm both.

XRD analyses finally confirmed the mineralogy showing the dominance of dolomite represented by the main peak at d = 2.88 Å. Further dolomite peaks are clearly visible and are indicated in the diffractogram (Fig. 5.10). The marly ground mass of the brecciated components is represented by a small amount of mica/illite at d = 9.96 Å° and calcite at d = 3.03 Å. Additionally, a small amount of quartz at d = 3.33 Å is present. The sample was measured on an aluminum sample holder which can also be seen in the diffractogram with two peaks at d = 2.34 and ≈ 2.03 Å.
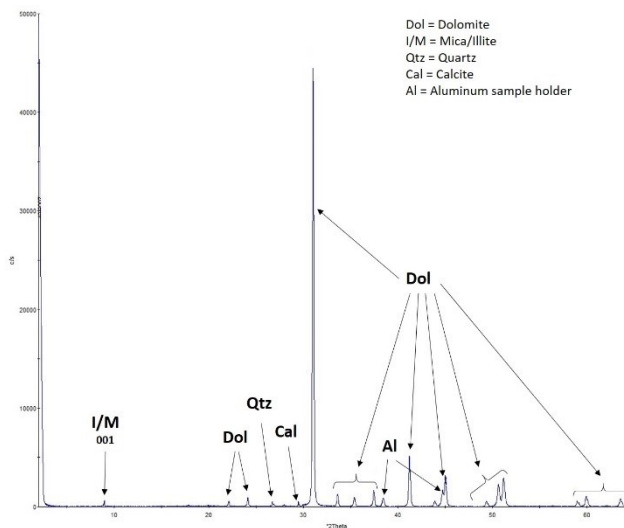
Fig. 5.10: X-ray diffractogram of sample ILZ 1,635.

Comparing those values to literature values, it is evident that the diffractogram is slightly shifted to lower d-values of about 0.01-0.02 Å, what proceeds also in the further diffractograms shown. Hence, only new peaks will be indicated separately in the particular diffractogram. Nevertheless, the peaks fit very well and the investigations give appropriate results for qualitative and quantitative mineralogical composition.

The sample at 1,672.5 m depth is characterized by a first occurrence of micaceous/illitic components of several mm grain size (Fig. 5.11 a, b) derived from a phyllite or mica schist, which also show deformation indicated by the kink bands. Opaque phases in those grains are mainly rutile as identified by RAMAN-spectroscopy.
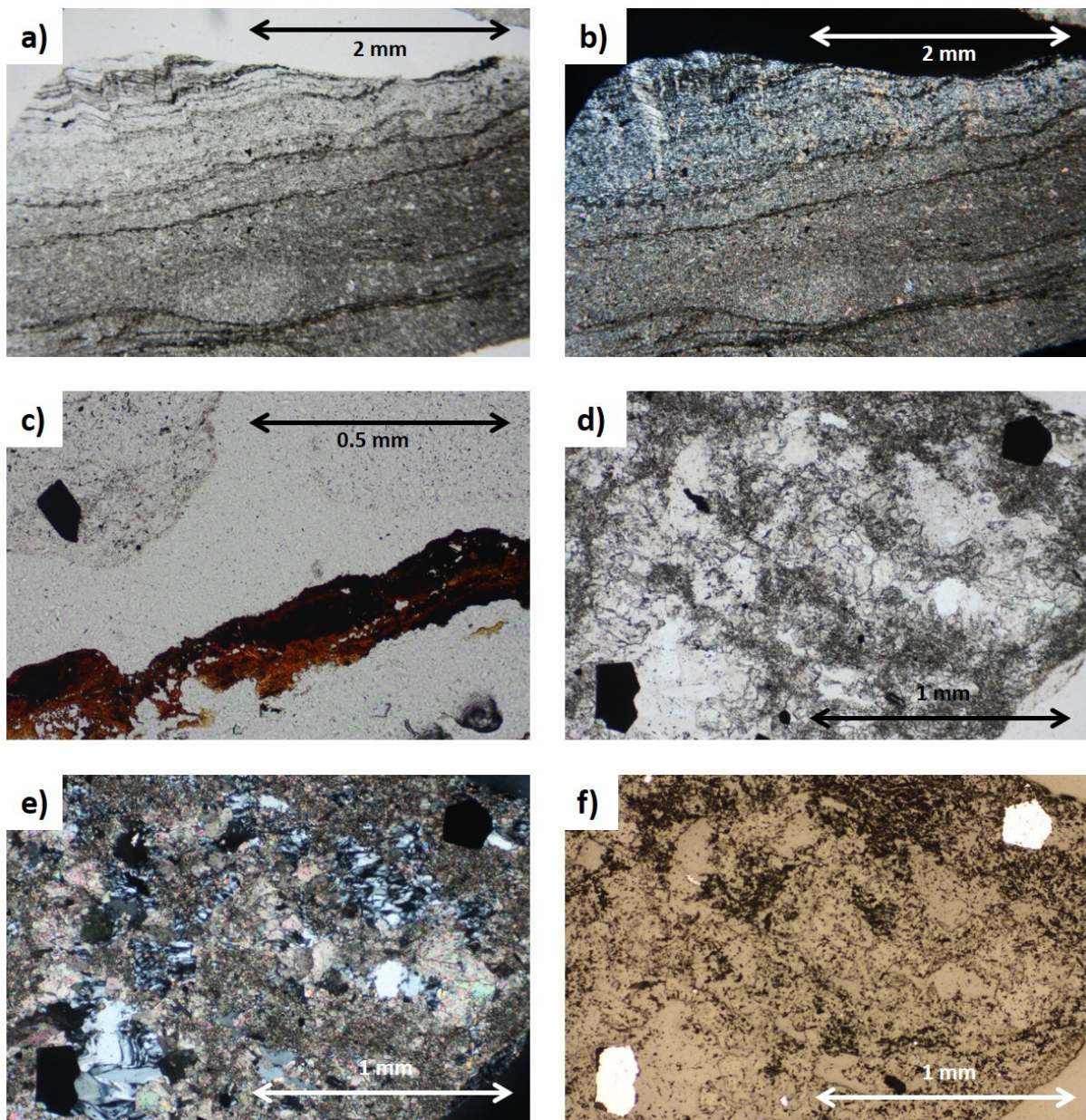

Fig. 5.11: Microphotographs of the sample ILZ 1,672.5 showing representative features. For further explanation, see text.

Oxidation structures, which were already observed macroscopically, form rims of about 0.2 mm thickness around mainly dolomite grains (Fig. 5.11 c). The red color points to the oxidation of Fe from pyrites and is thought to be derived from the storage under atmospheric conditions of the cuttings over the years since drilling. Pyrites in dolomites also seem to form perfectly idiomorph grains of a few tenth of millimeters grain size under transmitted light (Fig. 5.11 d, e) but when observed with reflective

light a slight disintegration on the rims already can be observed (Fig. 5.11 f). Additionally, the undulose extinction of quartz (Fig. 5.11 e) confirms a high degree of deformation.
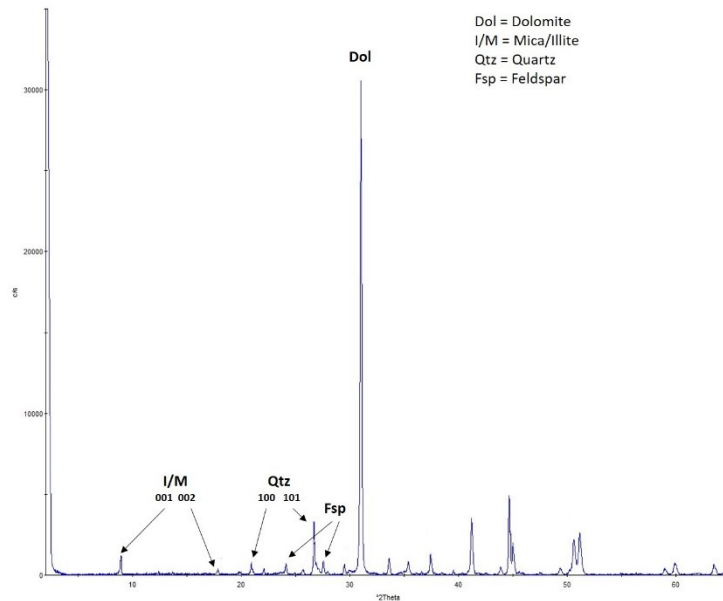

Fig. 5.12: X-ray diffractogram of sample ILZ 1,672.5.

XRD analysis still shows a dominance of dolomite in this sample but illite/mica 001 and 002, quartz 101 and 100 and feldspar, mainly orthoclase or microcline at d = 3.47 and 3.23 Å, peaks are already significantly increased compared to ILZ 1,635 (Fig. 5.12).

iii.   ILZ 1,687.5 and ILZ 1,697.5:

Those two samples show very similar characteristics, both in terms of microscopic features and X-ray diffraction, respectively. Dolomite within these samples mainly occurs subordinate as massive as well as fine grained and in brecciated components as described in Fig. 5.9 b. Major components are clasts from phyllites and mica schists containing crystalline components such as feldspars, mainly orthoclase and microcline, quartz and muscovite.
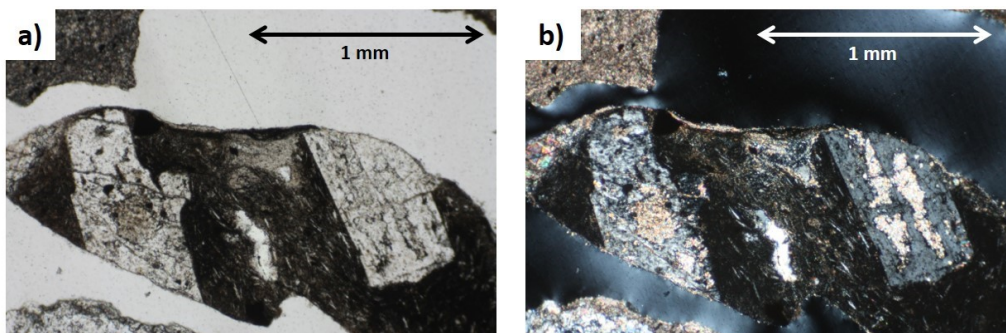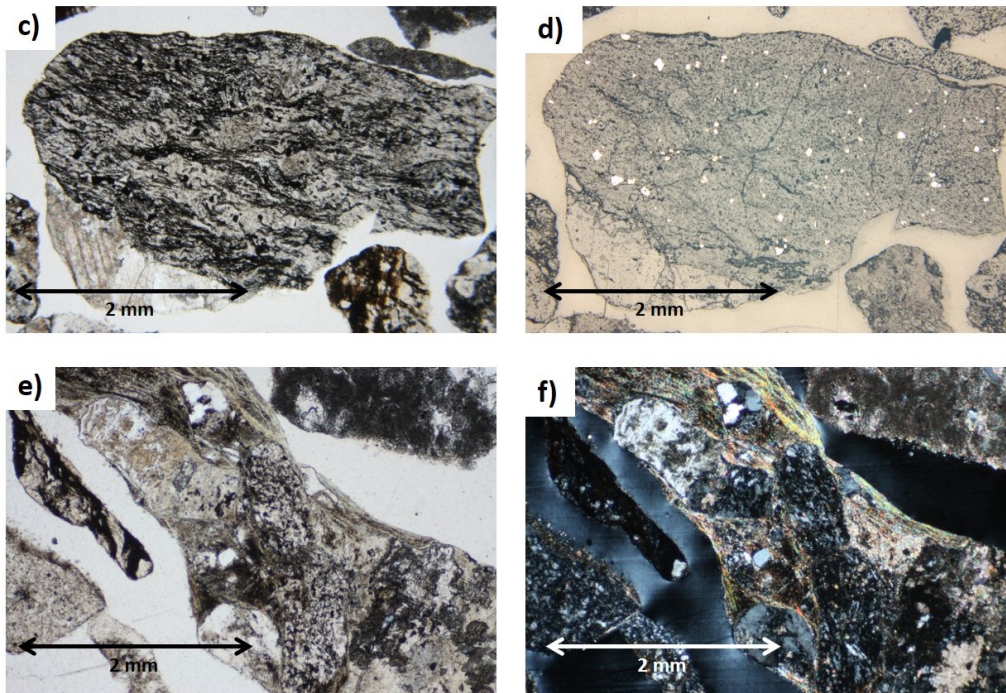
Fig. 5.13: Microphotographs of the samples ILZ 1,687.5 and ILZ 1,697.5 showing characteristic features of the phyllitic/faulted zone.

Feldspars are very well observable in Fig. 5.13 a and b in idiomorph grains of up to 1 mm size. In the center of the grains alteration to maybe kaolinite is evident what also explains the abundance of kaolinite in the X-ray diffractogram. Furthermore, rutile grains are again visible in the phyllitic components (Fig. 5.13 c, d) and a large mica schist clast is shown in Fig. 5.13 e and f, where the porphyryclastic fabric is represented by quartz and feldspars with low interference colors surrounded by muscovite of high interference color.

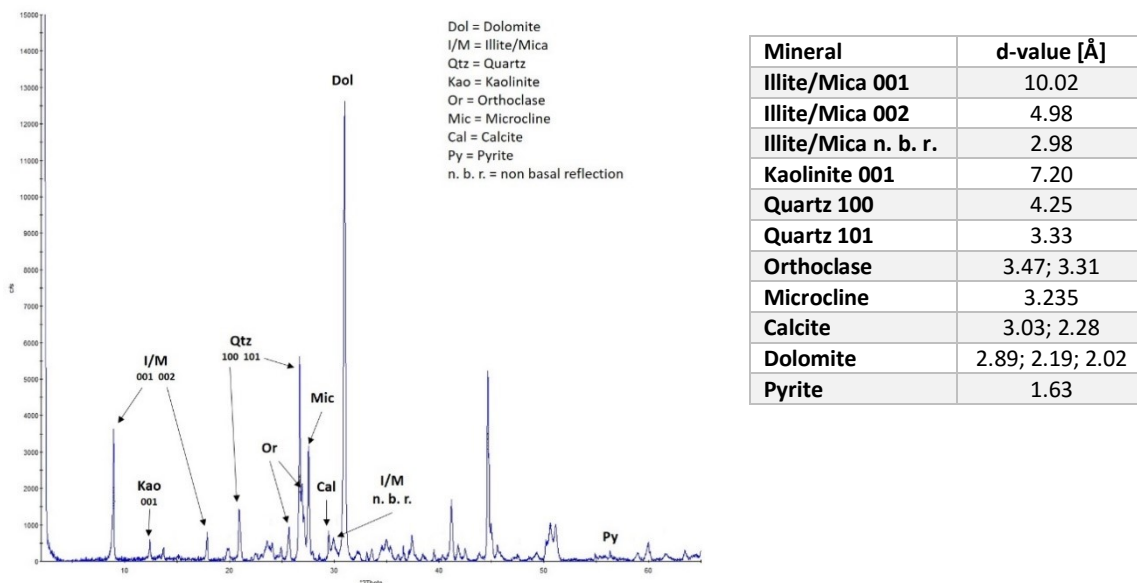| Mineral	d-value [Å]
Illite/Mica 001	10.02
Illite/Mica 002	4.98
Illite/Mica n. b. r.	2.98
Kaolinite 001	7.20
Quartz 100	4.25
Quartz 101	3.33
Orthoclase	3.47; 3.31
Microcline	3.235
Calcite	3.03; 2.28
Dolomite	2.89; 2.19; 2.02
Pyrite	1.63

Fig. 5.14: X-ray diffractogram of sample 1,697.5 representing the lower part of the phyllitic/faulted zone and table of major peak positions (d-values in Å) for the most significant phases.

XRD analysis confirms mineralogical composition with clearly visible illite/mica 001 and 002 peaks, kaolinite 001, quartz 100 and 101, feldspar, calcite, dolomite and even a small pyrite peak (Fig. 5.14). The illite/mica peaks are highly developed suggesting a high content of those phases and high illite crystallinity. The non-basal reflection at 2.98 Å or 29.98° 2Θ identifies the illite as a 2M illite with detrital origin, formed out of mica. Furthermore, high and distinct feldspar peaks give the opportunity to distinguish between different feldspars including most abundant phases orthoclase and microcline with their characteristic peak positions.

As a conclusion, the upper zone of the basement is characterized by an intercalation of light to dark grey dolomites, whereas changes in lithology occur abruptly. Light dolomites generally show a smaller grain size and are rich in splintered and platy components indicating content of clay minerals and therefore marl, whereas dark grey dolomites show a clean development and occur in coarse grains with white calcite joints.

Exceptions are the very dark to greenish horizons at 1,517.5-1,520.0, 1,540.0 and 1,582.5 m, indicating high clay content. Especially the upper two horizons might be influenced by hydrothermal alteration because of their location within the high porosity zone between approximately 1,510 and 1,540 m. The lower horizon at 1,582.5 m also is visible in the logs with slightly enhanced gamma radiation.

The phyllitic/faulted zone is characterized by very fine grained, light grey and splintered components of different origin. Dolomitic components occur together with phyllitic (mica) and crystalline ones containing mainly feldspar and quartz. Microscopic, RAMAN and XRD analyses revealed a more detailed insight into this zone and its mineralogical composition. Dolomites occur as different facies types from fossil-free mudstones to packstones and brecciated components (Goldbrunner et al., 2000). Additional high abundance of mica schist clasts with characteristic fabric elements (kink bands, quartz and feldspar porphyroclasts, undulose quartz extinction) suggests high faulting and deformation especially in the lower part of this zone between 1,687.5-1,702 m and maybe even an influence until 1,737.5 m as indicated by macroscopic description of cuttings.

The lower zone shows a much more homogeneous development than the upper and the phyllitic/ faulted zone consisting of medium to dark grey, granular dolomites with calcite filled fractures. Content of breccias (dolomitic components in a fine mainly calcite to marly ground mass) increase towards the base or the final depth of the well, respectively.

Last but not least, pyrite content throughout the whole basement indicates deposition of those carbonates in a reducing environment.

5.1.2.4 Pore space evaluation

Porosity, hydraulic conductivity and transmissivity of the basement were analyzed using well log data and interpreted with state-of-the-art literature models for the determination of those parameters.

Pore spaces in those carbonates were distinguished into a) total porosity and b) fracture porosity. Total porosity was calculated separately from the density- and sonic-log and from the combined solution of the equation system from density- and PE-log presented in section 5.1.2.2. From those results, a mean value was calculated to represent total porosity.

Effective porosity and subsequent fracture porosity, hydraulic conductivity and transmissivity was derived from the Dual Laterolog after the model presented by Vasvári (2011).

i. *Total porosity*

Total porosity was calculated from porosity logs like density-, sonic- and resistivity-logs. Results are shown in Appendix B. Calculation of porosity from density- ($\emptyset_D$) and sonic ($\emptyset_S$) -log (Wyllie time-average equation; Wyllie et al., 1958) is very similar with utilization of literature values for rock matrix and pore fluid:

$$\text{Sonic-derived porosity (Wyllie equation):} \qquad \emptyset_S = \frac{\Delta t_{log} - \Delta t_{ma}}{\Delta t_{fluid} - \Delta t_{ma}}$$

$$\text{Density-derived porosity:} \qquad \emptyset_D = \frac{\rho_{ma} - \rho_{log}}{\rho_{ma} - \rho_{fluid}}$$

Where: Δt_{log}, ρ_{log} = interval transit time and bulk density reading of the formation (from the log)

$\quad\quad$ Δt_{ma}, ρ_{ma} = interval transit time and density of the matrix (Tab. 5.3).

$\quad\quad$ Δt_{fluid}, ρ_{fluid} = interval transit time and density in the pore fluid (Tab. 5.3)

Resistivity-derived porosity was calculated after the same method as already used for the Neogene basin fill, whereas values within the phyllitic/faulted zone are not thought to be representative because of high shale content.

Separate observation of the porosities derived from the different logs (Fig. 5.15) shows, that the sonic log with an average of 8.2% gives much higher values than the density and the dual laterolog with 3.2% and 1.5%, respectively. Those difference can be explained by methodological reasons. Density is thought to be the most confident model for total porosity, whereas the sonic log depends strongly on compaction, fractures and their orientation what influences matrix slowness (Schön, 2011). The dual laterolog is assumed to be critical because of shale influence, especially in the phyllitic/faulted zone.
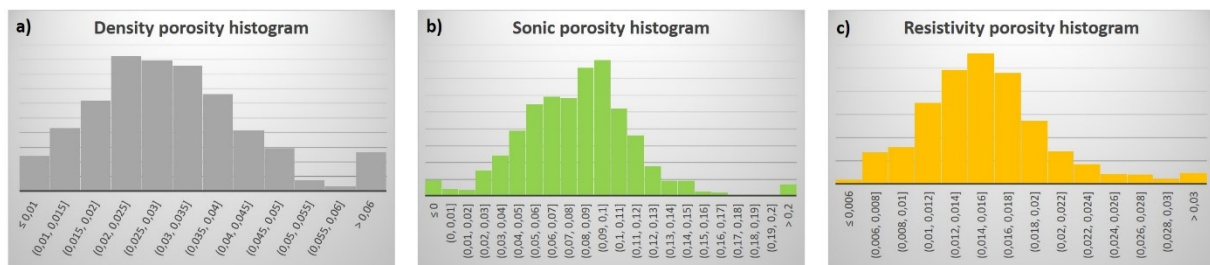

Fig. 5.15: Frequency distribution of porosity values derived from a) density-, b) sonic- and c) resistivity-logs.

However, for the entire basement, averaging all porosity calculations, the mean total porosity is pretty low with 4.2% but can be subdivided into several zones with higher and lower porosity (Appendix B). Starting from 1,468 m high porosity of over 10% might be influenced from the overlying Karpatian conglomerates but decreases to below 5% until 1,475 m. This is followed by an about 10 m thick low porosity zone with a mean value of 4.5%.

An about 8 m thick zone from 1,485 m until 1,493 m shows enhanced porosity, reaching values of over 10%, mainly due to a decrease of density. Afterwards porosity decreases again to below 5% and stays more or less constant with an average of 3.9% until 1,510 m.

Another high porosity zone is observed until about 1,540 m, indicated by drops of density to below 2.5 g/cm³, increases of slowness to nearly 300 μsec/m and even caliper outbursts point to a less consolidated, permeable zone. Porosity fluctuates strongly in this zone with maximal values of over 20% and minimal values of 5-6%. However, a mean porosity of 7.7% for this zone is not too high but

nevertheless regarding the thickness of 30 m, this can be seen as a major potential aquifer for exploration.

From there downwards, porosity decreases and stays more or less constantly low with an average of 4.5% until the transition to the phyllitic/faulted zone at 1,666 m. A sudden increase in slowness at around 1,666 m to over 260 µsec/m results in a very high sonic porosity of about 20% but is decreased to an average of 7.5% when taking into account other porosity calculations, what can be compared to the upper highly porous zone. With a thickness of only about 6.5 m, this zone is much thinner and is assumed to be formed by the accumulation of water above the upper impermeable part of the low porosity phyllitic/faulted zone.

The phyllitic/faulted zone as well as the lower dark grey dolomites are evolved very homogeneously in terms of porosity. Porosity is very low throughout the rest of the well with averages of 2.3% in the phyllitic/faulted zone and 3.3% in the lower dark grey dolomites.

ii.   *Fracture porosity after Boyeldieu & Winchester (1982):*

Fracture porosity in hard rocks such as the present basement carbonates, is in most cases significantly contributing to effective porosity and hence to hydraulic conductivity and transmissivity of an aquifer. Total porosities calculated before also include isolated intergranular pores, which do not contribute to effective porosity.

Two methods were used to investigate fracture parameters to determine fracture porosity: Utilization of a) the Dual Laterolog together with the model presented in Vasvári (2011) and b) the Schlumberger Log interpretation charts.

With the help of the Dual Laterolog (deep (RD) and shallow (RS) looking resistivity) together with drilling mud conductivity, water-filled fracture zones in a non-conductive massive rock can be investigated. Beside fracture porosity, aperture of horizontal and vertical fractures, fracture density and furthermore hydraulic conductivity and transmissivity can be estimated (Vasvári, 2011). Results are presented in the fracture porosity log in Appendix C.

In order to apply this method, first of all, resistivity (RS, RD, R_{mud}) must be transformed to conductivity (C_{LLs}, C_{LLd}, C_{mud}):

$$C_{LLs}\ [S/m] = {}^1\!/_{RS}\quad ;\quad C_{LLd}\ [S/m] = {}^1\!/_{RD}\quad ;\quad C_{mud}\ [S/m] = {}^1\!/_{R_{mud}}$$

Fracture porosity can then be estimated using the equation after Boyeldieu & Winchester (1982):

$$\emptyset_{frac} = \sqrt[m]{\frac{C_{LLs} - C_{LLd}}{C_{mud}}}$$

Where: m = cementation exponent (Tab. 5.5; John, 1999).

Results (appendix C) show, that fracture porosity follows the trend of resistivity-derived porosity in major parts throughout the basement indicating a high contribution of fracture porosity if compared to resistivity-derived porosity and even to total porosity (Tab. 5.6).

Pore System	m
Inter-granular/inter-crystalline	2.0
Fractures	1.4
Vugs	2.3
Moldic	> 3

Tab. 5.5: Cementation exponents m commonly used for different pore systems (after John, 1999).

One exception from this trend is observed in the upper high porosity horizon between 1,510 and 1,530 m where fracture porosity drops to below 0.5% whereas total porosity, as already mentioned above, increases strongly resulting in a $\emptyset_{frac}/\emptyset_{total}$-ratio of only about 10% (Tab. 5.6). This leads to the assumption, that intergranular pores dominate rather than fractures, maybe partly due to slightly enhanced shale content.

The same trend is observed in the upper part of the phyllitic/faulted zone from 1,666-1,682 m, but here the lithological change to phyllite and fine grained faulted material is thought to be responsible for the dominance of intergranular porosity. But because of generally low total porosity in this interval, fractures get a significant contribution of about 25%. High fracture porosity with a ratio of 68% in the lower part of this zone between 1,682 and 1,700 m (Tab. 5.6) is thought to represent especially a high fracture density and large apertures of vertical fractures due to intensive faulting and even indicating a sub-vertical fault.

Depth [m]	$\emptyset_{frac}$ [%]	$\emptyset_{resistivity}$ [%]	$\emptyset_{frac}/\emptyset_{resistivity}$	$\emptyset_{total}$ [%]	$\emptyset_{frac}/\emptyset_{total}$
1,470 – 1,510	1.6	1.7	0.94	5.9	0.27
1,510 – 1,530	0.8	2.3	0.35	8.0	0.1
1,530 – 1,598	1.4	1.5	0.93	4.3	0.33
1,598 – 1,666	1.3	1.8	0.72	4.8	0.27
1,666 – 1,682	0.6	2.2	0.27	2.4	0.25
1,682 – 1,700	1.5	2.1	0.71	2.2	0.68
1,700 – 1,885	1.2	1.2	0.99	3.3	0.36

Tab. 5.6: Intervals of homogeneous fracture porosities compared to resistivity-derived porosity and total porosity. Values are arithmetic means.

iii.   *Fracture porosity after Schlumberger (2000):*

Using the Schlumberger Log Interpretation Charts more or less same results for fracture porosity, assuming a cementation exponent m of 1.4, are obtained.
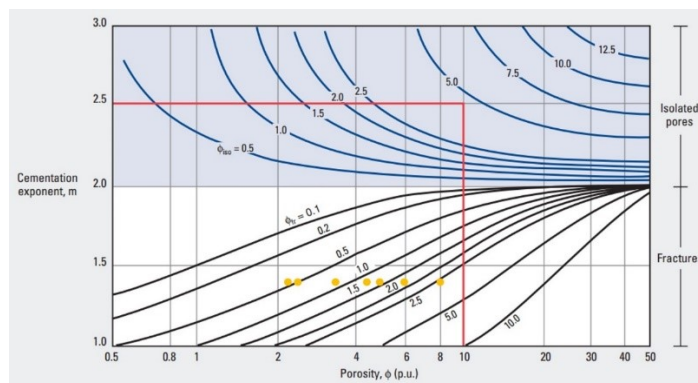
Fig. 5.16: Evaluation of fracture porosity using the Schlumberger Log Interpretation Charts.

Fracture porosity after Schlumberger (2000) ranges between about 0.5 and 1.8%, except the 2.5% for the high porosity interval 2, which is thought to be overestimated. Reasons therefore might be a possible influence of inter-granular or inter-crystalline porosity or other pore structures like vugs or moldic, what would change the cementation exponent (Tab. 5.5). However, other values fit well with little deviations if compared to fracture porosity after Boyeldieu & Winchester (1982) and therefore can be interpreted as representative.

iv. *Fracture apertures after Sibbit & Faivre (1985) and fracture densities:*

Sibbit & Faivre (1985) developed a model for estimating the aperture of horizontal (ε_h) and vertical (ε_v) fractures from parameters gained by the Dual Laterolog:

Vertical fracture aperture: $\qquad \varepsilon_v = \frac{C_{LLs} - C_{LLd}}{4*10^{-4}*C_m}$

Horizontal fracture aperture: $\qquad \varepsilon_h = \frac{C_{LLs} - C_b}{1.2*10^{-4}*C_m}$

Where: C_b = conductivity of non-fractured host rock in S/m.

For determination of C_b, the lowest measured values from the Dual Laterolog were used and subdivided into four zones (Tab. 5.7; Appendix C). For using this model, a conductivity contrast of C_m/C_b > 10^4 is assumed for the calculation of horizontal fracture apertures. To reach this contrast and to yield reasonable results, the constant in the formula for ε_h had to be increased by two magnitudes from $1.2*10^{-4}$ to $1.2*10^{-2}$.

Zone	Depth	C_b [S/m]
1	1,469.0 – 1,667.0	0.0035
2	1,667.0 – 1,695.0	0.013
3	1,695.0 – 1,797.5	0.0025
4	1,797.5 – 1,890.0	0.0043

Tab. 5.7: Subdivision of basement for determination of C_b.

To get an idea of dominating fracture orientation, Shaogui et al. (2006) defined a parameter Y, determining the dip of fractures based on a three-dimensional model. If Y is greater than 0.1, sub-vertical fractures dominate, if Y is between 0 and 0.1, inclined fractures dominate and if Y is negative, sub-horizontal fractures dominate (Vasvári, 2011):

$$Y = \frac{R_D - R_S}{\sqrt{R_D * R_S}}$$

Furthermore, fracture densities (d_{frac}) i.e. number of fractures per meter, was estimated using the equation from Vasvári (2011):

$$d_{frac} = \frac{1000 * \emptyset_{frac}}{\bar{\varepsilon}}$$

Where: $\bar{\varepsilon}$ = mean fracture apertures

Results (appendix C; Tab. 5.8) show, that vertical fractures generally have a higher aperture than horizontal fractures, whereas exceptions are again observed in the high porosity zone and in the phyllitic/faulted zone. Furthermore, vertical fractures with apertures ranging from 1 to 8 mm show a much more heterogeneous distribution than horizontal ones with apertures between 1 and 2 mm throughout. In the uppermost part, between 1,530 – 1,667 and in the lower zone, where clean dolomites are the dominating lithology, fracture structure is characterized by many small sub-horizontal fractures and few but larger vertical fractures, whereas sub-horizontal fractures dominate as indicated by the highly negative Y-value.

Depth [m]	$\overline{\varepsilon_v}$ [mm]	$\overline{\varepsilon_h}$ [mm]	$d_{frac,v}$ [m^{-1}]	$d_{frac,h}$ [m^{-1}]	Y
1,470 – 1,510	7.32	1.55	2.2	10.3	-0.12
1,510 – 1,530	1.82	3.81	4.4	2.1	-0.02
1,530 – 1,666	5.90	1.75	2.3	7.7	-0.09
1,666 – 1,682	2.11	1.10	2.8	5.5	0.02
1,682 – 1,700	7.95	1.87	1.9	8.0	0.07
1,700 – 1,885	5.00	1.06	2.4	11.3	-0.11

Tab. 5.8: Calculated mean fracture apertures, densities and estimation of fracture orientation for homogeneous intervals.

In the high porosity zone between 1,510 – 1,530 m, horizontal fractures show their largest apertures with close to 4 mm throughout the whole basement. High abundance of small vertical fractures results in a Y-value close to zero but still negative pointing to a slight dominance of sub-horizontal fractures (Tab. 5.8).

In the upper part of the phyllitic/faulted zone, fracture porosity as already indicated does not play a significant role, what is confirmed by both, small horizontal and vertical fractures. An increased vertical fracture density and a slightly positive Y-value assumes a higher influence of dipping fractures. In the lower part, vertical fractures reach apertures of nearly 30 mm, especially between 1,691 – 1,696 m and Y-values also increase to over 0.1, indicating large sub-vertical fractures, what confirms the assumption of a steep to sub-vertical fault in this zone. Goldbrunner et al. (2000) estimated the angle of this fault to 75°, resulting in a net thickness of around 5 m of this fault, if it is assumed to stretch from 1,682 – 1,702 m.

v.   *Hydraulic conductivity and transmissivity*

Hydraulic conductivity of fractures can easily be estimated by the "cubic law for fluid flow in a rock fracture", assuming ideal fractures with flat, smooth surfaces of uniform aperture and of infinitive length for laminar flow of a viscous, incompressible liquid (Witherspoon et al., 1980; Bear, 1993). Hydraulic single fracture conductivity k_f in m/s then is calculated with the following equation:

$$k_f = \frac{\rho * g}{\eta} * \frac{\overline{\varepsilon}^2}{12}$$

Where: ρ = water density (kg/m³)

g = gravitational acceleration = 9.81 m/s²

η = dynamic viscosity of water (Pa*s)

With this hydraulic fracture conductivity, the effective hydraulic conductivity k (m/s) of a formation and furthermore the transmissivity T (m²/s) can be calculated including the hydraulic conductivity of the hard rock k_r, which was assumed to be very weakly to non-conductive after classification DIN 18130-1 (Hölting & Coldewey, 2013) with a value of 10^{-9} m/s:

$$k = k_f * \frac{b}{l} + k_r$$

Where: l = mean fracture spacing (m) = 1/d_{frac}

First of all, hydraulic fracture conductivities were calculated separately for horizontal and vertical fractures but then a vector sum of both was formed to determine total effective hydraulic conductivity and transmissivity with thicknesses of the separate intervals in m:

$$T = thickness * k$$

Depth [m]	Thickness [m]	$k_{f,v}$ [x 10^{-5} m/s]	$k_{f,h}$ [x 10^{-5} m/s]	k [x 10^{-6} m/s]	T [x 10^{-5} m²/s]
1,470 – 1,510	40	15.7	0.5	2.8	11.2
1,510 – 1,530	20	3.8	1.8	0.5	1.0
1,530 – 1,666	136	10.4	1.1	1.6	21.8
1,666 – 1,682	16	3.1	1.6	0.6	0.96
1,682 – 1,702	20	31.6	1.3	9.4	18.8
1,702 – 1,885	183	8.6	0.5	1.2	22.0

Tab. 5.9: Calculations of hydraulic conductivity and transmissivity of the basement carbonates in homogeneous intervals.

Due to generally larger apertures, vertical fractures also show much higher hydraulic conductivities than horizontal ones (Tab. 5.9), especially in the faulted zone. However, fracture conductivities are in the range of 10^{-4} to 10^{-5} m/s resulting in total effective hydraulic conductivities of 10^{-6} m/s which is classified as permeable to weakly permeable after DIN 18130-1. Transmissivities also follow this trend with values of 10^{-4} to 10^{-5} m²/s, whereas highest transmissivities are reached in the clean carbonate horizons and in the faulted zone. For comparison, Goldbrunner et al. (2010) determined the transmissivity of the basement carbonates to be $4*10^{-5}$ m²/s and Vasvári (2011) to $7.3*10^{-5}$ m²/s. Hence, calculating a mean value for the whole basement from the results above yields an average transmissivity of $12.6*10^{-5}$ m²/s, what fits very well to those literature values.

Conclusively, if fractures are assumed to be the determining permeable structures for aquifer potential, according to this analysis, the whole basement can be seen as an interesting aquifer, although only showing permeable to weakly permeable conductivities.

The so-called "high porosity zone" from 1,510-1,530 or even 1,540 m is one of two exceptions and high total porosity is thought to be due to the increased shale/marl content bearing a large amount of capillary-bound water, which is not contributing to effective porosity (cf. section 2.1.2).

The second exception is the upper part of the phyllitic/faulted zone between 1,666 and 1,682 m, where both fracture porosity and total porosity is low and therefore can be interpreted as an impermeable horizon.

5.2   The Thermal Regime

Within a geothermal environment, two major parts are distinguished to describe the thermal regime:

a)   Heat sources
b)   Heat transport

5.2.1 Heat Sources

As already described in section 2.1.1, two principal sources of heat can be distinguished: a) the residual heat from the Earth's interior and b) radiogenic heat production mainly in the crust.

In the Pannonian Basin and especially in the Eastern Styrian Basin elevated geothermal gradients and high heat fluxes are thought to result from a high level of the Earth's mantle, which was actually proved geophysically by deep seismics by Schmöller (1991), who determined the location of the Mohorovicic-discontinuity at 19 km depth. This crustal thinning is due to the extensional regime resulting from the continental escape tectonics. Heat flux within the Styrian Basin is the highest in all Austria reaching values of > 100 mW/m² (Fig. 5.17).
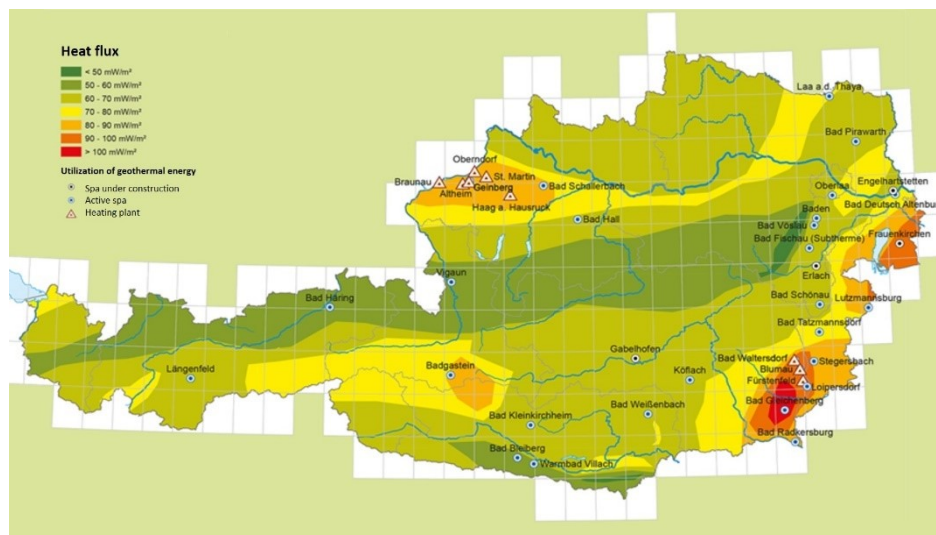
Fig. 5.17: Terrestrial heat flux in Austria (modified after GBA, 2016).

Geothermal gradient:

The geothermal gradient in the Eastern Styrian Basin is also elevated and ranges between 4-5 K/100 m (Goldbrunner et al., 2010). For the well ILZ Thermal 1, the geothermal gradient was calculated from data provided by Goldbrunner et al. (2010) from borehole temperature measurements. Mean annual surface temperature according to ZAMG (2015). Those data then were inter- and extrapolated until the final depth assuming a linear increase of temperature with depth (Tab. 5.10; Fig. 5.18).

Results gave a geothermal gradient of **45.54 °C/km**, what fits very well to literature values.

Depth [m]	Temperature [°C]	Formation
0	8.7	Surface
764 ± 43	46.0	Sandschaler Zone
1,004.5 ± 24.5	56.0	Lageniden Zone
1,778	89.7	Graz Paleozoic/Basement
1,906	96.5	Graz Paleozoic/Final depth

Tab. 5.10: Temperature data of borehole measurements used for calculation of the geothermal gradient. Temperature at final depth is already extrapolated.
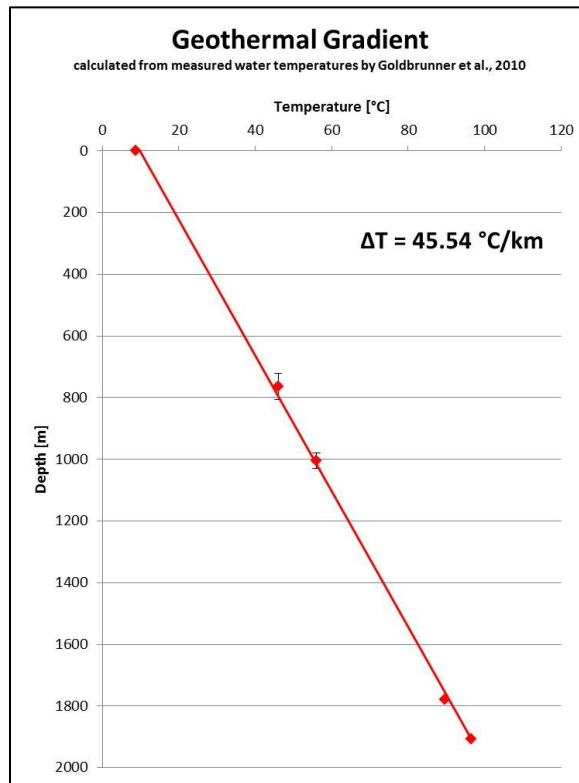
Fig. 5.18: Geothermal gradient interpolated from borehole measurements.

<u>*Radiogenic heat production:*</u>

A second heat source is the heat produced by the radiogenic decay of K, Th and U, which occurs mainly in crust. The amount of heat produced can be determined in the laboratory by time consuming methods such as XRF or gamma-ray spectrometry (Bücker & Rybach, 1996) but Rybach (1986) developed a formula to calculate the amount of heat A in µW/m³ produced in the subsurface by radioactive decay from the spectral gamma ray log measuring the contributions of those isotopes to total gamma activity:

$$A \ (\mu W/m^3) = 10^{-5} * \rho * (9.52 \ c_U + 2.56 \ c_{Th} + 3.48 \ c_K)$$

Where: ρ = rock density in kg/m³

c_U = concentration of uranium in ppm

c_{Th} = concentration of thorium in ppm

c_K = concentration of potassium in %.

Results (Fig. 5.19; appendix D) show what can be expected from the basement: Low radiogenic heat production in the upper light to dark grey dolomites and in the lower dark grey dolomites with values of around 0.8 – 1.1 µW/m³. In the phyllitic/faulted zone, because of high abundance of crystalline components bearing especially K and Th, radiogenic heat production increases to over 2.0 µW/m³, whereas highest values of up to 3.5 µW/m³ are reached around 1,675 m and at 1,691 m.
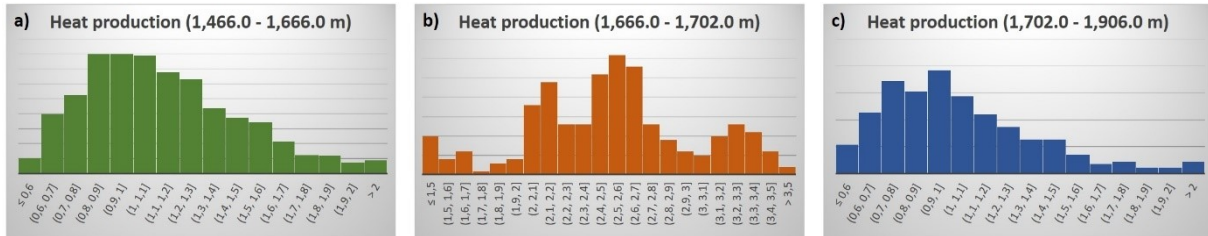
Fig. 5.19: Frequency distribution of heat production values in µW/m³ for the upper light to dark grey dolomites and marls (a), the phyllitic/faulted zone (b) and the lower dark grey dolomites (c).

5.2.2 Heat Transport – Thermal Conductivity

Heat can be transported in the subsurface in two ways: a) Through convection by fluid flow and b) through conduction based on the thermal conductivity of rocks.

Concerning convective heat transport, it cannot be quantified how much heat is transported by the water circulating through the rocks, what is dependent on the permeable zones described in section 5.1.2.4. Generally, convective heat transport is significant because of the very high heat capacity c_P of water. Hence it is assumed, that heat is in fact transported to a certain degree in the clean carbonates and especially in the lower phyllitic/faulted zone, where the fault might form a major pathway for fluid flow.

Heat transported by conduction through the rocks, on the other hand, can be quantified and results in specific thermal conductivity λ of rocks. For comparison, a compilation of thermal properties of significant rocks, minerals and water from literature is given in Tab. 5.11.

Mineral/Rock/Fluid	λ [W/m K]	c_P [kJ/kg K]
Dolomite	5.5	0.93
Dolomite (rock)	4.38; 4.68	1.0
Calcite	3.59	0.79
Limestone	2.29	0.93
Quartz	6.5	0.70
Sandstone/Conglomerate	2.47	1.64
Muscovite	2.28 ± 0.07	0.76
Illite	1.9	
Kaolinite	2.6	0.93
Orthoclase	2.31	0.61
Microcline	2.49	0.68
Shale	2.07	1.18
Marl	2.21	1.15
Water	0.50-0.59	4.2

Tab. 5.11: Thermal properties of significant minerals, rocks and water. Data taken from Schön (2004) after Cermak & Rybach (1982), Brigaud et al. (1989, 1992), Jessop (1990), Clauser & Huenges (1995), Clauser (2006).

Thermal conductivity can be examined on rock samples by laboratory experiments, but also equations for estimating this parameter on carbonate rocks based on formation factor F, calculated from the resistivity log, were introduced by Gegenhuber (2013) and Gegenhuber & Schreilechner (2014):

a) Dolomite: $\lambda\,[Wm^{-1}K^{-1}] = 11.10 * \frac{1}{F} - 56.68 * \left(\frac{1}{F}\right)^{1/2} + 7.21$

b) Limestone: $\lambda\,[Wm^{-1}K^{-1}] = 32.29 * \frac{1}{F} - 28.65 * \left(\frac{1}{F}\right)^{1/2} + 4.04$

Where: $F = R_D/R_W$

In this thesis, equation (a) was used for estimating thermal conductivity conditions in the basement. Results in form of a log are shown in appendix D and in Fig. 5.20.
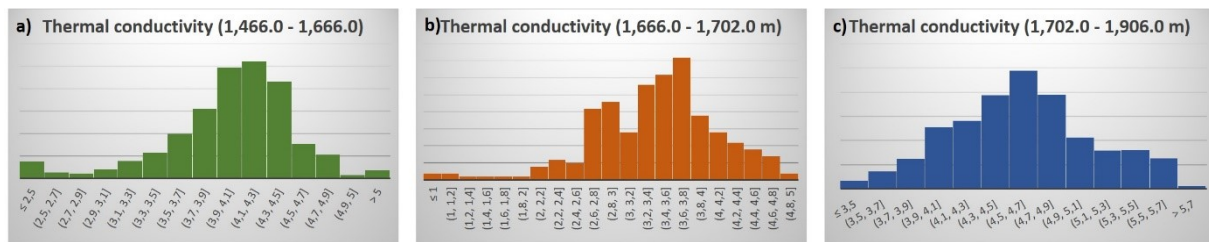
Fig. 5.20: Frequency distribution of thermal conductivity in W/m K for the upper light to dark grey dolomites and marls (a), the phyllitic/faulted zone (b) and the lower dark grey dolomites (c).

In the upper light to dark grey dolomite and marl series, thermal conductivity ranges between 3.9 and 4.5 W/m K, which fits with literature values of dolomite, whereas zones of lower conductivity are found in marly and water rich horizons e.g. around 1,525 m. A very low thermal conductivity zone from 1,603 – 1,605 m can be correlated with an enhanced electrical conductivity and therefore fracture porosity zone (appendix C) with low shale content and hence indicates a water-bearing horizon in clean medium to dark grey dolomites (Tab. 5.4).

The phyllitic/faulted zone is characterized by a generally lower thermal conductivity. At the transition to the upper dolomites (1,666-1,668 m) values of below 1 W/m K confirm a water-bearing highly porous and permeable zone, which was already indicated by high fracture porosity, electrical conductivity and slowness. Below this, thermal conductivity increases again to an average of 3.2-3.8 W/m K but then decreases in the lower part to below 3.0 W/m K, pointing to a higher abundance of low conductivity phases such as feldspar or mica, which were also proven already by optical microscopy and XRD (section 5.1.2.3).

The lower dark grey dolomites show a more or less constant thermal conductivity, what would be expected from clean dolomites, ranging between 4.3 and 4.9 W/m K. Exceptions are observed between 1,727 – 1,731 m and around 1,812.5 m where low conductivity can be correlated with high radiogenic heat production in shale-rich, marly intercalations.

5.2.3 Estimation of Geothermal Resources

For quantification of heat and energy resources available in geothermal reservoirs, the USGS volumetric model "Heat in Place" (Muffler & Cataldi, 1978) was used. First of all, potential aquifers in the well ILZ Thermal 1, based on reservoir characterization, were identified:

- Sandschaler Zone (702.5 – 807.3 m)

- Base Conglomerate of the Lageniden Zone (966.1 – 1,240.0 m)
- Karpatian "Conglomerate-rich Series" (1,240.0 – 1,466.0 m)
- Upper clean dolomites (1,530.0 – 1,666.0 m)
- Lower dark grey dolomites (1,702 – 1,906.0 m)

The USGS "Heat in Place" model estimates the amount of heat or energy H stored in a porous reservoir i.e. rock matrix and in the pores filled with water after the following relation (Muffler & Cataldi, 1978; Hurter & Schellschmidt, 2003):

$$H = \left((1 - \emptyset) * \rho_m * c_m + \emptyset * \rho_w * c_w\right) * (T_1 - T_0) * A * \Delta z$$

Where: $\emptyset$ = porosity (section 5.1)

ρ_m, ρ_w = density of rock matrix and water in kg/m³ (section 5.1.2.2)

c_m, c_w = specific heat capacity of rock matrix and water in J/(kg K); (Tab. 5.11)

T_1 = temperature at top of aquifer in °C (section 5.2.1; Appendix A)

T_0 = surface temperature in °C = 8.7°C (section 5.2.1)

A = area under consideration in m²

Δz = net aquifer thickness in m (Appendix A)

For this calculations, an area A of 500x500 m with the well in the center is considered with the assumption, that lateral extent of homogeneous formations is constant in terms of thickness. Net aquifer thicknesses were derived by summing up the thicknesses of potential water-bearing horizons shown in appendix A. To calculate the total resource Q, the heat H stored in the reservoir is multiplied with a geothermal recovery factor R depending on parameters derived from production and reinjection technology i.e. reinjection temperature T_r of water in a reinjection well. Assuming a reinjection temperature of 25°C (Hurter & Schellschmidt, 2003), the recovery factor is calculated after Lavigne (1978):

$$R = 0.33 * \frac{(T_1 - T_r)}{(T_1 - T_0)}$$

and finally

$$Q\,[J] = H * R$$

Aquifer	Δz [m]	$\emptyset$ [-]	ρ_m [kg/m³]	ρ_w [kg/m³]	c_m [J/kg K]	c_w [J/kg K]	T_1 [°C]	H [x10¹⁵ J]	R [-]	Q [x10¹⁴ J]
Sandschaler Zone	46.0	0.22	2650	993.9	1640	4182	41.7	1.6	0.17	**2.7**
Base Conglomerate	199.5	0.11	2650	1002.8	1640	4187	53.7	9.7	0.21	**20.5**
Karpatian	185.5	0.15	2650	1002.8	1640	4192	66.2	11.5	0.24	**27.3**
Upper basement dolomites	136.0	0.045	2870	980.3	1000	4200	79.4	7.0	0.25	**17.9**
Lower basement dolomites	204.0	0.033	2870	980.3	1000	4200	87.2	11.7	0.26	**30.5**

Tab. 5.12: Estimation of geothermal resources stored in potential aquifers of the well ILZ Thermal 1.

According to the results shown in Tab. 5.12 a total heat content of nearly 10^{10} MJ or converted $2.8*10^9$ kWh is stored in the considered aquifers. This only represents a very rough estimate of producible energy, because especially values for the thermal recovery factor are influenced by much more parameters and therefore can only be conjectured in this stage. Furthermore, if it comes to utilization of a geothermal resource, further engineering parameters like conversion efficiency, plant life or plant load factor (Garg & Combs, 2010; 2011) get important. However, a first estimation of geothermal resources can be done and roughly assuming a project life of 50 years this results in a capacity of 6.3 MW.

5.3   Thermal Water Characterization

In this last chapter, the results of the analyses of available data concerning the thermal waters investigated are presented. Chemical and physical data of the waters of the Sandschaler Zone, the Base Conglomerate of the Lageniden Zone and the Paleozoic basement are available and discussed in the following. Data of the thermal water from the Paleozoic basement from the well Bad Blumau 2 used for indirect purposes and electricity production are also available for comparison.

5.3.1 Data Presentation and Reliability Check

The base of all calculations and investigations within this chapter are thermal water analyses concerning mainly electrolyte content and other physical parameters presented in Goldbrunner et al. (2010) for the waters of the Lageniden Zone, the Paleozoic basement and Bad Blumau and from Arsenal Research (2000) for the water of the Sandschaler Zone. A compilation of those data is shown in Tab. 5.13:

		Sandschaler Zone	Lageniden Zone	Graz Paleozoic	Bad Blumau
Cations (mg/l)	NH_4^+	4.6	9.1	6.9	30.0
	Na^+	1,400.0	5,560.0	5,380.0	5,570.0
	K^+	36.0	174.0	170.0	138.6
	Mg^{2+}	3.0	12.6	7.5	4.6
	Ca^{2+}	10.0	43.0	31.5	30.2
Σ Cations		1,453.6	5,798.7	5,595.9	5,773.4
Anions (mg/l)	HCO_3^-	3,243.8	7,505.1	8,786.5	8,090.0
	Cl^-	313.6	4,320.0	3,000.0	3,620.0
	SO_4^{2-}	0.31	284.0	230.0	506.4
Σ Anions		3,557.7	12,109.1	12,016.5	12,216.4
TDS (mg/l)		5,011.3	17,907.8	17,612.4	17,989.8
K (mS/cm)	25°C	5.2	20.0	18.18	20.07

Tab. 5.13: Electrolyte composition (TDS = Total Dissolved Solids) of major cations and anions of thermal waters from the well ILZ Thermal 1 and Blumau 2 and electrical conductivity K measured at 25°C.

A first look on the data already reveals the similarity of the deeper waters of the well ILZ Thermal 1 with the water from Bad Blumau in terms of mineralization with a TDS content of nearly 18 g/l. Only the water from the Sandschaler Zone shows a much lower mineralization with around 5 g/l, what confirms the Lower Badenian "Tonmergel Series" to act as a major separating, impermeable layer between deeper and shallower groundwater, preventing mixing of them.

Before start of work and calculations, the reliability of these data was checked based on the principle of electro-neutrality, where positive charges of cations (meq/l) must compensate negative ones of anions (meq/l):

$$\sum {meq}/{_l}(+) = \sum {meq}/{_l}(-)$$

Therefore, a balancing error is calculated to verify this electro-neutrality after the following equation:

$$Error\ (\%) = \frac{\sum \, ^{meq}/_l\,(+) - \sum \, ^{meq}/_l\,(-)}{\sum \, ^{meq}/_l\,(+) + \sum \, ^{meq}/_l\,(-)} * 100$$

	MM [g/mol]	z	MMeq [g/eq]	Sandschaler Zone c [mmol/l]	Sandschaler Zone m [meq/l]	Lageniden Zone c [mmol/l]	Lageniden Zone m [meq/l]	Graz Paleozoic c [mmol/l]	Graz Paleozoic m [meq/l]	Bad Blumau 2 c [mmol/l]	Bad Blumau 2 m [meq/l]
NH_4^+	18.04	1	18.04	0.26	0.26	0.50	0.50	0.38	0.38	1.66	1.66
Na^+	22.99	1	22.99	60.90	60.90	241.85	241.85	234.02	234.02	242.28	242.28
K^+	39.10	1	39.10	0.92	0.92	4.45	4.45	4.35	4.35	3.54	3.54
Mg^{2+}	24.31	2	12.15	0.12	0.25	0.52	1.04	0.31	0.62	0.19	0.38
Ca^{2+}	40.08	2	20.04	0.25	0.50	1.07	2.15	0.79	1.57	0.75	1.51
Σ Cations				**62.45**	**62.82**	**248.39**	**249.98**	**239.84**	**240.94**	**248.43**	**249.37**
HCO_3^-	61.02	1	61.02	53.16	53.16	123.00	123.00	144.00	144.00	132.59	132.59
Cl^-	35.45	1	35.45	8.85	8.85	121.86	121.86	84.63	84.63	102.12	102.12
SO_4^{2-}	96.06	2	48.03	$3.23*10^{-3}$	$6.45*10^{-3}$	2.96	5.91	2.39	4.79	5.27	10.54
Σ Anions				**62.01**	**62.02**	**247.82**	**250.78**	**231.02**	**233.42**	**239.98**	**245.25**
Error [%]					**0.64**		**-0.16**		**1.59**		**0.83**

Tab. 5.14: Reliability check of data by calculating a balancing error based on electro-neutrality.

For this calculation, the concentration of electrolytes must be transformed from mass concentration w in mg/l to equivalent concentration m in meq/l. An error of ± 2% is accounted as acceptable for amount of substance concentrations c of > 2 mmol/l (DVWK, 1979; 1992).

$$c \left[{}^{mol}/_l \right] = \frac{w \left[{}^{g}/_l \right]}{MM \left[{}^{g}/_{mol} \right]} \; ; \qquad m \left[{}^{eq}/_l \right] = \frac{w \left[{}^{g}/_l \right]}{MM_{eq} \left[{}^{g}/_{eq} \right]} \text{ with } \quad MM_{eq} = \frac{MM}{z}$$

Where: MM = mole mass

MM$_{eq}$ = equivalent mole mass

z = charge of ion

Deviations from perfect electro-neutrality i.e. an error of 0.0% might be due to inability of quantitative analyses to reach perfectly exact results or presence of trace substances which were not included into the analyses or cations in chemical complexes, which were not dissolved during sample preparation and analyses (Hölting & Coldewey, 2013).

Nevertheless, results in Tab. 5.14 show, that even with the very high mineralization of deeper groundwater with nearly 250 mmol/l, balancing errors stay below ± 2% and therefore data are accounted as reliable and further investigations can be executed.

5.3.2 Classification of Thermal Waters

Groundwater, no matter if deep or shallow, are generally classified based on their ionic composition. For this purpose, several graphical solutions are available:

- PIPER-diagram
- SCHOELLER-diagram
- GIGGENBACH-diagram

i. *Classification after the PIPER-diagram (Piper, 1953):*

The PIPER-diagram uses cationic and anionic composition separately, plotted in two ternary diagrams, to be finally combined in a diamond diagram to give a specific water type (Fig. 5.21). For this solution, equivalent concentrations of main cations (Na^+, K^+, Mg^{2+}, Ca^{2+}) and anions (HCO_3^-, Cl^-, SO_4^{2-}) are recalculated to 100% (Tab. 5.15) and then plotted in the diagrams.

	Sandschaler Zone		Lageniden Zone		Graz Paleozoic		Bad Blumau 2	
	meq/l	%	meq/l	%	meq/l	%	meq/l	%
$Na^+ + K^+$	61.82	98.81	246.30	98.72	238.37	99.09	245.83	99.24
Mg^{2+}	0.25	0.39	1.04	0.42	0.62	0.26	0.38	0.15
Ca^{2+}	0.50	0.80	2.15	0.86	1.57	0.65	1.51	0.61
Σ Cations	62.56	100.00	249.48	100.00	240.55	100.00	247.71	100.00
HCO_3^-	53.16	85.73	123.00	49.05	144.00	61.69	132.59	54.06
Cl^-	8.85	14.26	121.86	48.59	84.63	36.26	102.12	41.64
SO_4^{2-}	0.01	0.01	5.91	2.36	4.79	2.05	10.54	4.30
Σ Anions	62.02	100.00	250.78	100.00	233.42	100.00	245.25	100.00

Tab. 5.15: Recalculation of equivalent concentration to percentage for use in the PIPER-diagram.

In terms of relative composition, all waters show similar characteristics concerning cation with a dominance of sodium and potassium of over 98% and very low calcium and magnesium (Tab. 5.15).

Concerning anions, chloride and especially bicarbonate (85% in the Sandschaler Zone) dominate but with varying ratios. Sulfate only plays a subordinate role with highest content in the water from Bad Blumau with over 4%. In the water from ILZ, sulfate is slightly above 2% (Tab. 5.15). This elevated sulfate content in deeper waters points to a stronger magmatic or juvenile influence.
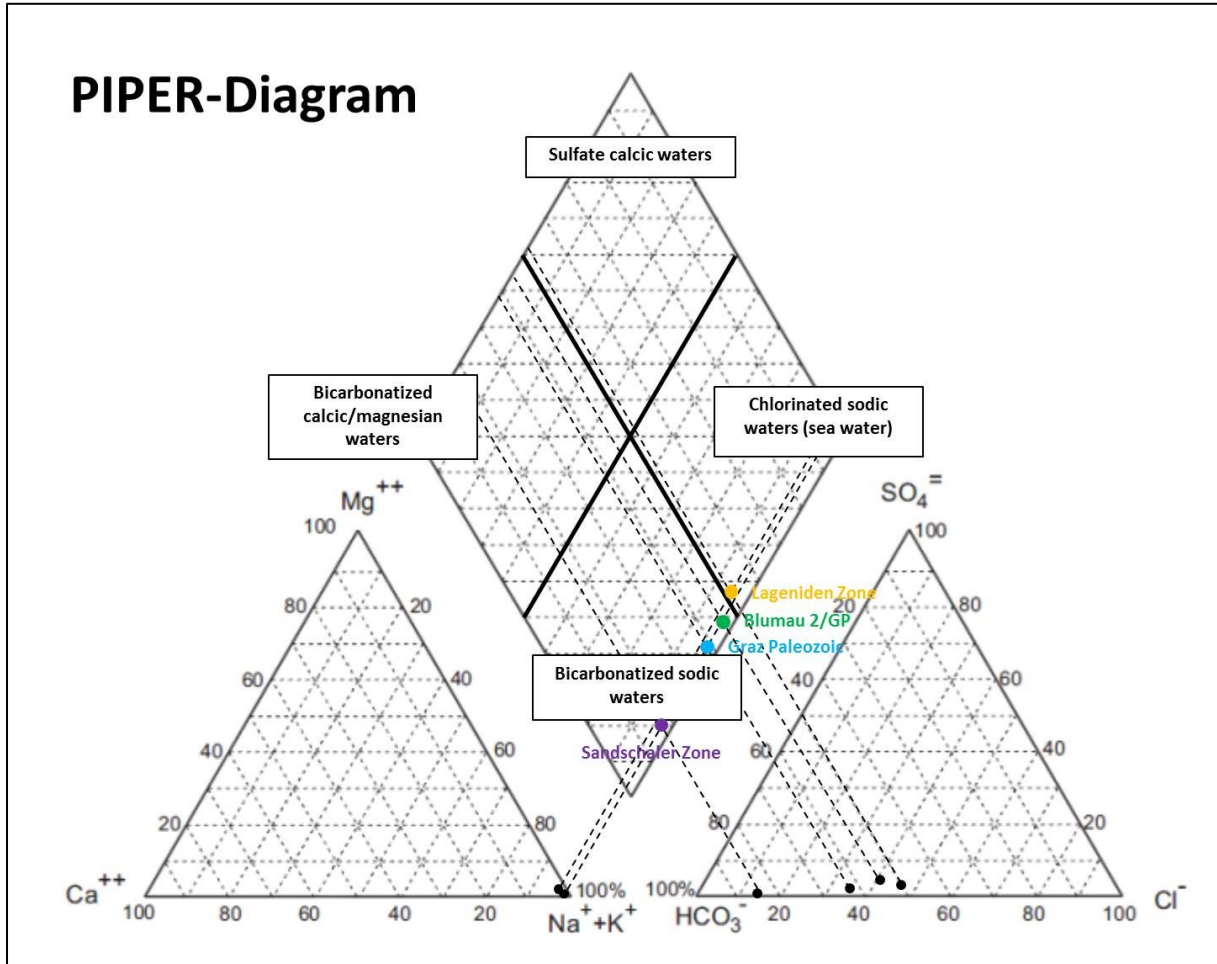
Fig. 5.21: Graphical classification of deep groundwaters of the well ILZ Thermal 1 and Bad Blumau 2 in the PIPER-diagram.

Graphical solution in the PIPER-diagram (Fig. 5.21) again shows the dominance of sodium, potassium and bicarbonate and chloride, respectively and therefore the waters are classified as indicated in Tab. 5.16.

Water	Type
Sandschaler Zone	**Na-HCO$_3$ - water**
Lageniden Zone	**Na-Cl-HCO$_3$ - water**
Graz Paleozoic	**Na-HCO$_3$ - water**
Bad Blumau 2	**Na-HCO$_3$-Cl - water**

Tab. 5.16: Water classification based on ionic composition after Piper (1953).

ii.   *Classification after the SCHOELLER-diagram:*

In contrast to the PIPER-diagram, the SCHOELLER-diagram plots absolute equivalent concentrations of different components and component pairs on a logarithmic scale. The purpose of this diagram is more to illustrate similarities of compositions between several waters rather than to classify waters (Fig. 5.22).
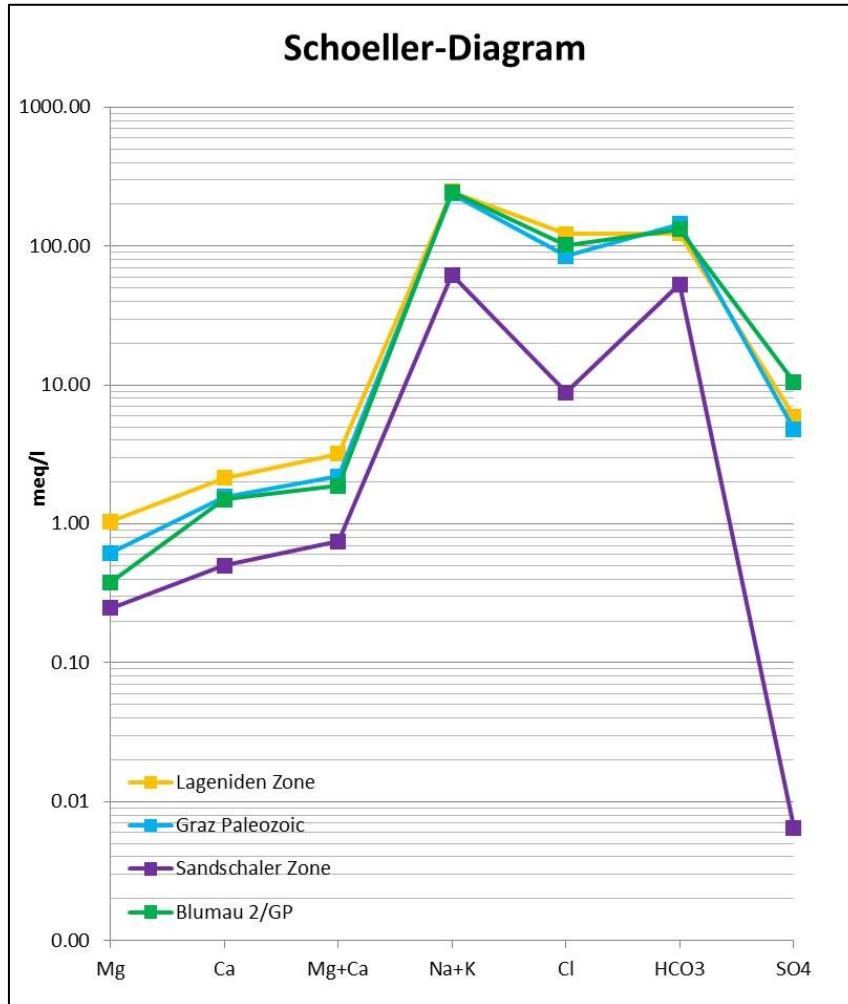
Fig. 5.22: Illustration of the waters in the SCHOELLER-diagram.

Fig. 5.22 shows, that especially the water from the Lageniden Zone, the basement and from Bad Blumau are very similar both, in terms of composition pattern and even in absolute equivalent concentration. Therefore, it is assumed, that this water is related to each other in terms of composition, physical and chemical properties and probably even in origin.

The water from the Sandschaler Zone also shows a similar composition pattern but is lower mineralized than the other ones.

iii.   *Classification after the GIGGENBACH-diagram (Giggenbach, 1988):*

The GIGGENBACH-diagram is a ternary diagram, classifying thermal water based on their anionic composition using mass concentrations in mg/kg. The main purpose of this diagram is to identify possible origins and other influencing processes like mixture with magmatic/juvenile waters, steam heated waters, influence of groundwater and maturity of waters.

Waters rich in sulfate are thought to be highly influenced by mixtures with magmatic/juvenile waters or heated by steam rich in H_2S resulting in very acid waters due to oxidation of H_2S. Deep thermal groundwater or peripheral waters are indicated by a high content in HCO_3^-, whereas maturity of water or water in equilibrium with the environment is indicated by dominance of chloride, because chloride is the anion with greatest solubility i.e. remains in the water when all other constituents have been precipitated resulting in more or less pure "mature" water.
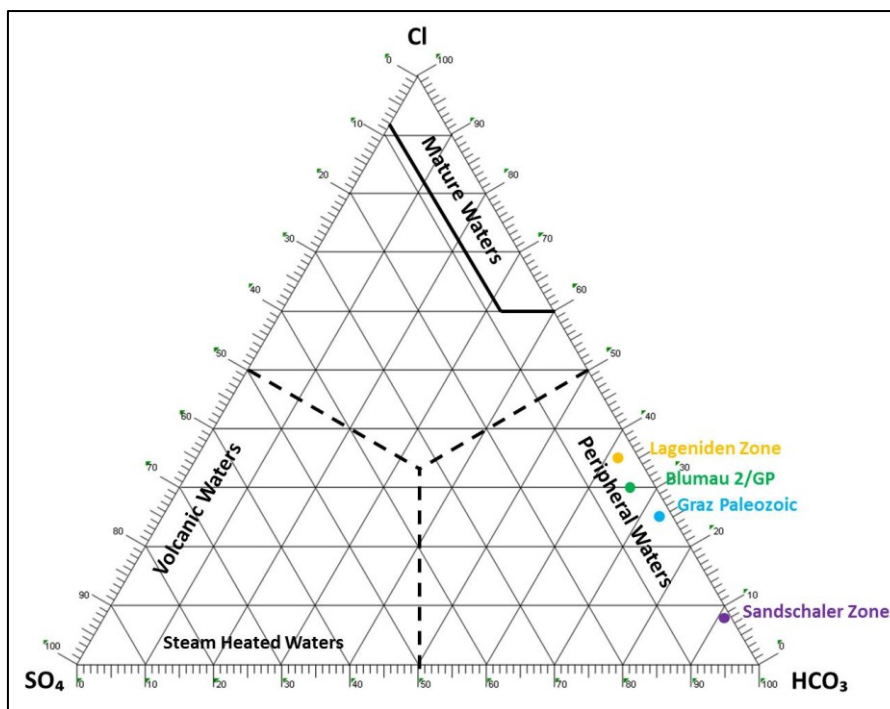
Fig. 5.23: Classification of waters in the GIGGENBACH-diagram.

Results in Fig. 5.23 show, that all waters plot in the field of peripheral waters, confirming those as deep thermal groundwater, non-influenced by magmatic waters or steam and also not mature.

For "quantification" of maturity, Giggenbach (1988) also introduced a maturity index I calculated from cation composition in order to apply cation geothermometers for the estimation of the temperature in the reservoir.

$$I = 0.315 * \log\left(\frac{K}{Mg}\right) - \log\left(\frac{K}{Na}\right)$$

Where: K, Mg, Na are mass concentrations in mg/l.

Generally, a maturity index of ≥ 2.66 define a mature water in equilibrium and cation geothermo-meters can be applied giving reliable results. If I is between 2.0 and 2.66, the water is in partial equilibrium, cation geothermometers can be applied but further methods for confirmation should be

used. If I < 2.0, the water is termed as immature and cation geothermometers do not give reliable results.

For the waters from ILZ and Bad Blumau the following maturity indexes were obtained (Tab. 5.17):

	I
Sandschaler Zone	1.93
Lageniden Zone	1.86
Graz Paleozoic	1.93
Bad Blumau 2	2.07

Tab. 5.17: Maturity indexes of the waters from ILZ and Bad Blumau.

Maturity indexes of the waters from ILZ all lie below 2.0 and therefore cation geothermometers were not applied. Furthermore, equilibria for cation geothermometers are thought to be reached only at temperatures > 150°C (Fournier, 1981) and hence application at temperatures below 100°C is not recommended. Temperatures at Bad Blumau reach 110°C (Legmann, 2003), what is thought to be the reason for the slightly enhanced maturity index indicating water in partial equilibrium.

Because other data were not available for the waters, other geothermometers, e.g. SiO_2 – geothermometer, also were not applied.

5.3.3 Isotope Hydrochemistry

Isotope data (δD, $\delta^{18}O$) are available for the water of the Sandschaler Zone from Arsenal Research (2000) and for the Paleozoic water from Goldbrunner (1999; Tab. 5.18):

	δD [‰]	$\delta^{18}O$ [‰]
Sandschaler Zone	-69.50 ± 1.0	-10.19 ± 0.1
Graz Paleozoic	-62.78	-8.18

Tab. 5.18: Isotope analyses for the Sandschaler Zone and the Graz Paleozoic. Data from Arsenal Research (2000) and Goldbrunner (1999).

The water from the Sandschaler Zone plots on the global meteoric water line (MWL, Fig. 5.24) together with other shallow water samples from the Eastern Styrian Basin, e.g. Bad Waltersdorf or Bad Blumau indicating a meteoric water influence.

The water from the Paleozoic basement, on the other side, plots below the meteoric water line indicating a non-meteoric influence or at least altered groundwater by water-rock interactions. The water from the basement together with other deep thermal water samples of the region (e.g. Fürstenfeld, Bad Blumau 1 and 2) lies on a mixing line intersecting the MWL at the point cloud of the shallow water samples.

Isotope composition also seems to be independent from lithology at least in the shallow waters. At Bad Waltersdorf shallow waters are also derived from carbonates of the Graz Paleozoic from 1,100-1,300 m depth, whereas in the well Bad Blumau 3, the water comes from the Sarmatian at 650-1,000 m (Goldbrunner et al., 2010).
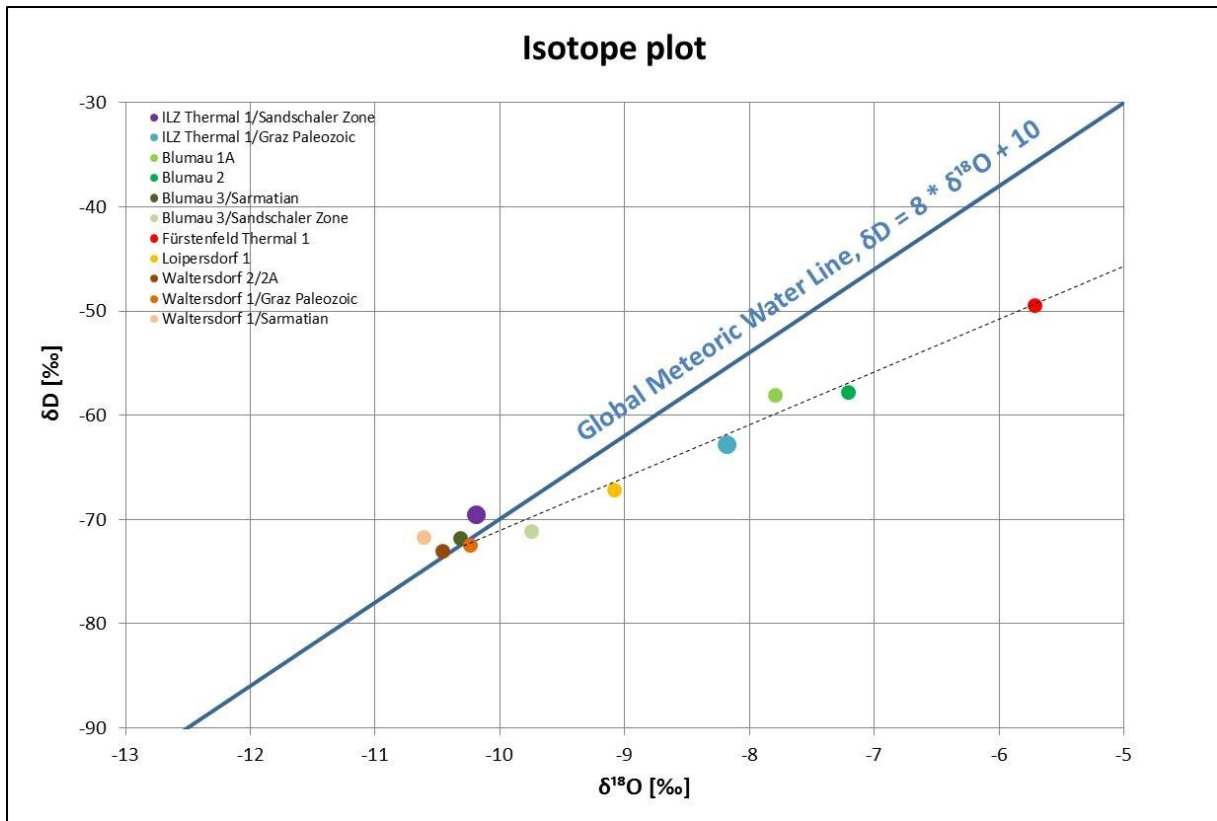
Fig. 5.24: Isotope plot of the waters of ILZ Thermal 1 relative to the global meteoric water line and compared to other waters of the Eastern Styrian Basin. Modified after Goldbrunner (1999).

On the other hand, the deeper water from the Fürstenfeld well comes from the Sandschaler Zone between 1,650 and 1,900 m and the water from Bad Blumau 2 and 1A from Paleozoic carbonates in 2,360-3,000 m depth. Here, probably a slight lithological influence is evident because the shallower water from Fürstenfeld in the sandstones shows far higher isotopic ratios than the carbonate hosted waters from ILZ and Bad Blumau.

The interpretation therefore is, that isotope composition is mainly a result of water-rock reactions increasing with temperature and depth and deeper thermal waters are more or less closed off from meteoric influence.

5.3.4 Physical Properties

Physical properties of the waters are results from laboratory and in field measurements executed by Arsenal Research (2000), especially for the Sandschaler Zone water. Results obtained are presented here. Further important physical properties (density, electrical conductivity, pH, hardness), especially for the Lageniden Zone and the Paleozoic were estimated and calculated from electrolyte content using models presented in literature, because analyses data were not available. Those results were also important for porosity calculations which use water properties, e.g. resistivity- (ARCHIE-equation), density-derived porosity.

5.3.4.1 Electrical Conductivity

Electrical conductivity of the waters was measured and presented at 25°C (Tab. 5.13) by Arsenal Research (2000) and Goldbrunner et al. (2010), but because of temperature dependence, it is important to use resistivity values (R_w) at formation temperatures for porosity calculations.

Electrical conductivity at formation temperatures T_f (Tab. 5.10; Goldbrunner et al., 2010), therefore was calculated using the model presented by McCleskey et al. (2012), but first of all the viability of this model was checked by comparing results with measured values.

After McCleskey et al. (2012), electrical conductivity (κ) can be calculated using the following relation:

$$\kappa = \sum \lambda_i * m_i$$

Where: λ_i = ionic molal conductivity of the ith ion
m_i = molality (mol/kg) of the ith ion

Molality was calculated using amount of substance c (Tab. 5.14) and water densities from section 5.3.4.2. Ionic molal conductivities of the several ions are also presented in McCleskey et al. (2012):

$$\lambda = \lambda^0(T) - \frac{A(T) * \sqrt{I}}{1 + B * \sqrt{I}}$$

Where: λ^0, A = temperature-dependent functions (Tab. 5.19)
B = empirical constant (Tab. 5.19)
I = Ionic strength of water
z_i = ionic charge of the ith ion (Tab. 5.14)

$$I = \frac{1}{2} * \sum m_i * z_i^2$$

Ion	λ^0 (T in °C)	A (T in °C)	B
NH_4^+	$0.003342\ T^2 + 1.285\ T + 39.04$	$0.00132\ T^2 + 0.6070\ T + 11.19$	0.3
Na^+	$0.003763\ T^2 + 0.8770\ T + 26.23$	$0.00027\ T^2 + 1.141\ T + 32.07$	1.7
K^+	$0.003046\ T^2 + 1.261\ T + 40.70$	$0.00535\ T^2 + 0.9316\ T + 22.59$	1.5
Mg^{2+}	$0.01068\ T^2 + 1.695\ T + 57.16$	$0.02453\ T^2 + 1.915\ T + 80.50$	2.1
Ca^{2+}	$0.009645\ T^2 + 1.984\ T + 62.28$	$0.03174\ T^2 + 2.334\ T + 132.3$	2.8
HCO_3^-	$0.000614\ T^2 + 0.9048\ T + 21.14$	$-0.00503\ T^2 + 0.8957\ T + 10.97$	0.1
Cl^-	$0.003817\ T^2 + 1.337\ T + 40.99$	$0.00613\ T^2 + 0.9469T + 22.01$	1.5
SO_4^{2-}	$0.01037\ T^2 + 2.838\ T + 82.37$	$0.03324\ T^2 + 5.889\ T + 193.5$	2.6

Tab. 5.19: λ^0, A and B parameters for calculation of electrical conductivity after McCleskey et al. (2012).

	$\kappa_{measured}$ (25°C) [mS/cm]	$\kappa_{calculated}$ (25°C) [mS/cm]	T_f [°C]	$\kappa_{calculated}$ (T_f) [mS/cm]	R_w (T_f) [Ohmm]
Sandschaler Zone	5.2	5.12	45.2	**7.49**	**1.33**
Lageniden Zone	20.0	19.98	56.0	**34.37**	**0.29**
Graz Paleozoic	18.18	18.06	89.7	**49.81**	**0.20**

Tab. 5.20: Calculated electrical conductivity and resistivity of waters at formation temperatures.

Results presented in Tab. 5.20 were the basal resistivity values for interpolation of water resistivity for all temperatures and depths using the following equation after Arps (1953):

$$R_w(T_2) = R_w(T_1) * \frac{T_1 + 21.5}{T_2 + 21.5}$$

Those results, finally were used in the Archie equation for obtaining resistivity-derived porosity.

5.3.4.2 Density

Density measurements of the waters were not available at all, but are important for the calculation of density-derived porosity apart from consistent literature values. Hence, the density of the three different waters were also calculated based on the salt content after Aeschbach-Hertig:

$$\rho(T, m_i) = \rho(T) * \left(1 + \sum \beta_i * m_i\right)$$

Where: $\rho(T, m_i)$ = temperature-/substance-dependent density
$\rho(T)$ = density of pure water at temperature T
β_i = specific contraction coefficient (Tab. 5.21)
m_i = mass concentration (mg/l)

Salt	β_i [10^{-6} l/mg]	MM_{eq} [mg/meq]
NaCl	0.719	58.44
Na(HCO$_3$)	0.728	84.01

Tab. 5.21: Specific contraction coefficients and equivalent mole masses for the different salts (after Aeschbach-Hertig).

Because of dominance of Na$^+$, Cl$^-$ and HCO$_3^-$ in the waters, only NaCl and Na(HCO$_3$) were regarded as the salts dissolved in the water. Hence, Cl$^-$ and HCO$_3^-$ were apportioned to Na$^+$ according to their equivalent concentration to gain 100% and then were recalculated to mass concentration using the equivalent mole mass of the salts.

	$\rho(T_f)$ [kg/l]	NaCl : Na(HCO$_3$)		$\rho(T_f, m_i)$ [kg/l]
		m_i [mg/l]	[%]	
Sandschaler Zone	0.990	498.2 : 4399.5	14 : 86	**0.9935**
Lageniden Zone	0.985	7,066.7 : 10,158.3	50 : 50	**0.9974**
Graz Paleozoic	0.965	5,128.5 : 12,286.7	37.5 : 62.5	**0.9775**

Tab. 5.22: Calculated densities for the waters at formation temperatures.

The density and viscosity estimates for the Paleozoic water (Tab. 5.22) finally was used for the calculation of density-derived porosity, hydraulic conductivity and in the combined lithological analysis.

5.3.4.3 pH-Value

Data of measurements of the pH of the water were only available for the Sandschaler Zone from Arsenal Research (2000), who determined a field pH of **6.98**.

The pH of the deeper thermal waters can only be estimated using the fact, that carbonate is dissolved as the bicarbonate (HCO_3^-) ion indicating a pH between around 6.5 and 10.5 (Fig. 5.25). But this, of course, is just a very rough estimate.
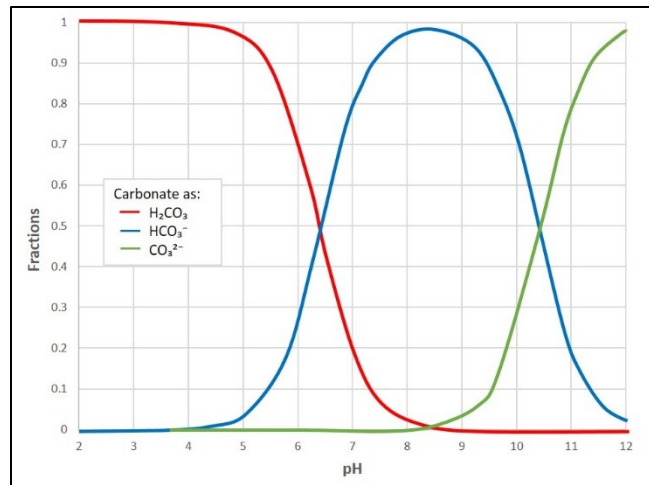
Fig. 5.25: Diagram for the estimation of the pH from carbonate fractions.

5.3.4.4 Hardness

Concerning hardness, again only data from the water of the Sandschaler Zone was available from Arsenal Research (2000), who determined the hardness of the water to be 2.09 °dH.

Hardness can be calculated from the concentration of Mg^{2+} and Ca^{2+}, which is available for all waters. Hence, hardness was calculated after the equation presented in Hölting & Coldewey (2013):

$$Hardness\ (°dH) = \frac{m_{CaO} + 1.4 * m_{MgO}}{10}$$

Whereas:

$$m_{CaO} = m_{Ca^{2+}} * 1.4 \quad ; \quad m_{MgO} = m_{Mg^{2+}} * 1.643$$

Mass concentrations m_i are in mg/l and coefficients are obtained from the proportions of the mole masses between Ca^{2+}/Mg^{2+} and CaO/MgO, respectively.

	Hardness (°dH)	Classification
Sandschaler Zone	2.09	Very soft
Lageniden Zone	8.95	Middle hard
Graz Paleozoic	6.15	Soft

Tab. 5.23: Calculation of hardness after Hölting & Coldewey (2013) and classification after Klut & Olszewski (1945).

First of all, results in Tab. 5.23 show that calculations fit perfectly with data gained from Arsenal Research (2000) and therefore results for the deeper waters are assumed to be reliable. Furthermore, as expected, hardness of the deeper waters is much higher than from the Sandschaler Zone, whereas

the water from the Lageniden Zone is with 8.95 °dH the hardest, due to highest Ca and Mg-concentration.

5.3.5 Gas content

Gas analyses were also executed by Arsenal Research (2000) for the water of the Sandschaler Zone. Results of this analysis is shown in Tab. 5.24 with a dominance of nitrogen, methane and carbon dioxide. Especially the high concentration of methane indicates contact with organic matter.

Gas	mg/l	mmol/l	Vol.-%
CO_2 (dissolved)	386.7	8.786	
CO_2	204	4.64	19.4
N_2	292	10.4	43.9
H_2			< 0.05
CH_4	139	8.64	36.3
O_2			< 0.05
He			< 0.05
Ar	2.82	0.088	0.37
Σ	638	23.8	100.0

Tab. 5.24: Gas analysis for the water of the Sandschaler Zone. Data from Arsenal Research (2000).

For the deeper thermal waters, no gas analyses were executed but carbonate precipitation during degassing due to pressure drop indicates a very high CO_2 content, what could represent a problem during production and utilization (Eisner & Goldbrunner, 1999). Therefore, further investigations would be necessary.

6   Interpretation

Final interpretation of results comprises two major parts:

1. Introduction of the well ILZ Thermal 1 to regional geology and stratigraphic correlation by comparison with nearby wells and regional geological considerations.
2. Hydrogeological and geothermal interpretation, showing major potential aquifers for drinking water or even thermal water utilization.

6.1   Stratigraphic Correlation and Regional Geology

For stratigraphic correlation and introduction of the well into regional geology, available data from wells in the vicinity (Tab. 6.1) and descriptions of formations from literature were used.

Well	Distance [km]	Source
Arnwiesen 1	10.8	Ebner (1988)
Walkersdorf 1	4.4	RAG (1965)
Ottendorf Thermal 1	4.4	Eisner & Goldbrunner (2003)
Fürstenfeld Thermal 1	14.3	Goldbrunner (1988)
FF 1	18.0	Böchzelt & Goldbrunner (2000)
FF 2	16.9	Böchzelt & Goldbrunner (2000)

Tab. 6.1: Nearby wells used for stratigraphic correlation and introduction into regional geology with distance to the well ILZ Thermal 1 and reference of data.

Using lithological and stratigraphic profiles from those different wells, a geological W-E profile was compiled from Arnwiesen 1 to Fürstenfeld, introducing the well ILZ Thermal 1 into regional geology (Appendix E).

6.1.1 Basement

Starting with the basement, carbonate lithologies are assigned to the Graz Paleozoic according to regional geological considerations and literature. Dolomites of the Graz Paleozoic were also hit in the wells Arnwiesen 1, Walkersdorf 1 and Fürstenfeld Thermal 1, making up the basement of the Fürstenfeld subbasin (Ebner, 1988; RAG, 1965; Goldbrunner, 1988). Distinction between different units within the Paleozoic basement were only reported from Arnwiesen 1 by Ebner (1988), who distinguished an Upper to Middle Devonian hanging zone, correlated with limestones from the Rannach Nappe (340.6 – 409 m below surface), against black schists ("*Arzberg Series*"; 409 – 497.5 m) and dolomites (497.5 – 951.7 m) possibly from the Schöckl Nappe in the lower part. The wells Walkersdorf 1 and Fürstenfeld Thermal 1 only hit the uppermost part of those carbonates and also were assigned to the Rannach Nappe (RAG, 1965; Goldbrunner, 1988).

Therefore, the upper light to dark grey dolomites and marls from ILZ Thermal 1 are also assigned to the Rannach Facies of the upper nappe system, using the recently introduced facies concept by Gasser et al. (2010). Based on lithological descriptions therein, the upper dolomites and marls possibly can be correlated with the Dolomite Member of the Dolomite-Sandstone Series (Flügel & Neubauer, 1984) or the Flösserkogel Formation (Flügel & Hubmann, 2000) consisting of early diagenetic, yellow dolomites, limestones and sandstones (Gasser et al., 2010).

The great differences and lithological change from light to dark grey dolomites and marls in the upper zone to very homogeneous, dark grey brecciated dolomites in the lower zone also suggests a stratigraphic change. Therefore, the lower zone is assigned to the Schöckl Facies, described as dark gray carbonates and black schists, deposited in an euxinic environment by Gasser et al. (2010). Maybe those dolomites can be correlated with the dark brecciated lower dolomites from Arnwiesen 1, which were described and assigned to the Raasberg Formation by Ebner (1988). The only vagueness remains, to which extent, a separating phyllitic or schist horizon between the upper and the lower zone as described in Arnwiesen 1 or also in Blumau 1a (Ebner, 1988) plays a role. It is suggested, due to very high gamma radiation and high abundance of crystalline components resulting from cuttings analyses, that those were introduced by faulting activity from a crystalline basement below the dolomites especially between 1,682 and 1,702 m. The total thickness of the Graz Paleozoic, i.e. the depth where this crystalline (probably Austro-Alpine) basement might start, cannot be estimated because it was not hit any other well below the dolomites.

The light color of cuttings from the phyllitic/faulted zone could be due to bleaching or argillitization (illite from mica and kaolinite from feldspar) by high hydrothermal activity within the fault, whereas a hydrothermal aureole might extend even from 1,645 until 1,737.5 m. However, with this interpretation the age of the basement dolomites is assumed to be Lower to Middle Devonian with parts reaching maybe Upper Devonian introducing ILZ Thermal 1 into the dolomite complex of the interpretation from Ebner (1988).

6.1.2 Neogene Basin Fill

Karpatian

Neogene basin fill in the well ILZ Thermal 1 starts with a 226 m thick homogeneous succession of clean sandstone/conglomerate with few thin shaly/marly intercalations, which can be correlated with the "Conglomerate-rich Group" of Piller et al. (2004). Those conglomerates also were described in all wells east of ILZ with increasing thickness from west to east. Karpatian sediments are missing in Arnwiesen 1 at all. This confirms the location of this area in a marginal facies of the basin during Karpatian times with fluvial sedimentation (Ebner & Sachsenhofer, 1995). Fine-grained calcareous mud- and siltstones with sandy, turbiditic intercalations termed the "Styrian Schlier" (Ebner & Sachsenhofer, 1995) was perforated only in Walkersdorf 1. The "Styrian Schlier" neither was hit in ILZ nor in the other wells indicating a very local distribution. Sea-level low-stand and tectonic events ("Styrian phase") finally caused the formation of the "Styrian Unconformity" separating Karpatian from Badenian sediments (Friebe, 1991).

Badenian

The Karpatian "Conglomerate-rich Group" is overlain by Badenian sediments with a total thickness of nearly 670 m. The whole succession starts with a coarse conglomeratic development, which is correlated to the "Base Conglomerate" of the Lageniden Zone, also reported from the wells in Fürstenfeld. Formation terms in the Styrian Basin follow the biostratigraphic subdivision from the Vienna Basin based on foraminiferan ecostratigraphy (*Lagenidae, Bulimina/Bolivina Zone;* Gross et al., 2007). This confirms again the marginal position with a fluvial environment in the Fürstenfeld subbasin (Ebner, 1988), whereas major parts of the Styrian Basin were occupied by a shallow marine environment after an eustatic sea level rise in the Early Badenian (Friebe, 1990; Rögl, 1998; Kovac et al., 2004). Andesitic volcanism also occurred in the area of Walkersdorf/Ilz at this time and Flügel (1988) even postulated the dimensions of this volcanite body in his underground map of the basement of the Styrian Basin. However, volcanites were not hit in ILZ and therefore the extent of Badenian volcanites, which were only hit in Walkersdorf 1, is thought to be smaller than postulated.

Deposition of nearly 160 m thick fine-grained shales, silts and marls are correlated with the "Tonmergel Series" and already indicate a sea level rise with the shift of the depocentre into the Fürstenfeld subbasin with marine conditions (Ebner & Sachsenhofer, 1995). Sea level fluctuations and diverging subsidence (Friebe, 1990) during the Middle Badenian then led to the deposition of dominantly coarse sandstones intercalating with fine-grained sediments summarized in the "Sandschaler Zone". The Late Badenian again was affected by a sea level rise resulting in an off-shore, fine-grained sedimentation represented by the "Bulimina-Bolivina/Rotalia-Cibicides Zone". Correlation of the Miocene from the Sandschaler Zone upwards was possible by using Gamma Ray data from nearby wells (Ottendorf Th1, FF 1 and FF 2; data from Geoteam Ges.m.b.H.) showing very good accordance especially between ILZ and Walkersdorf (Fig. 6.1).
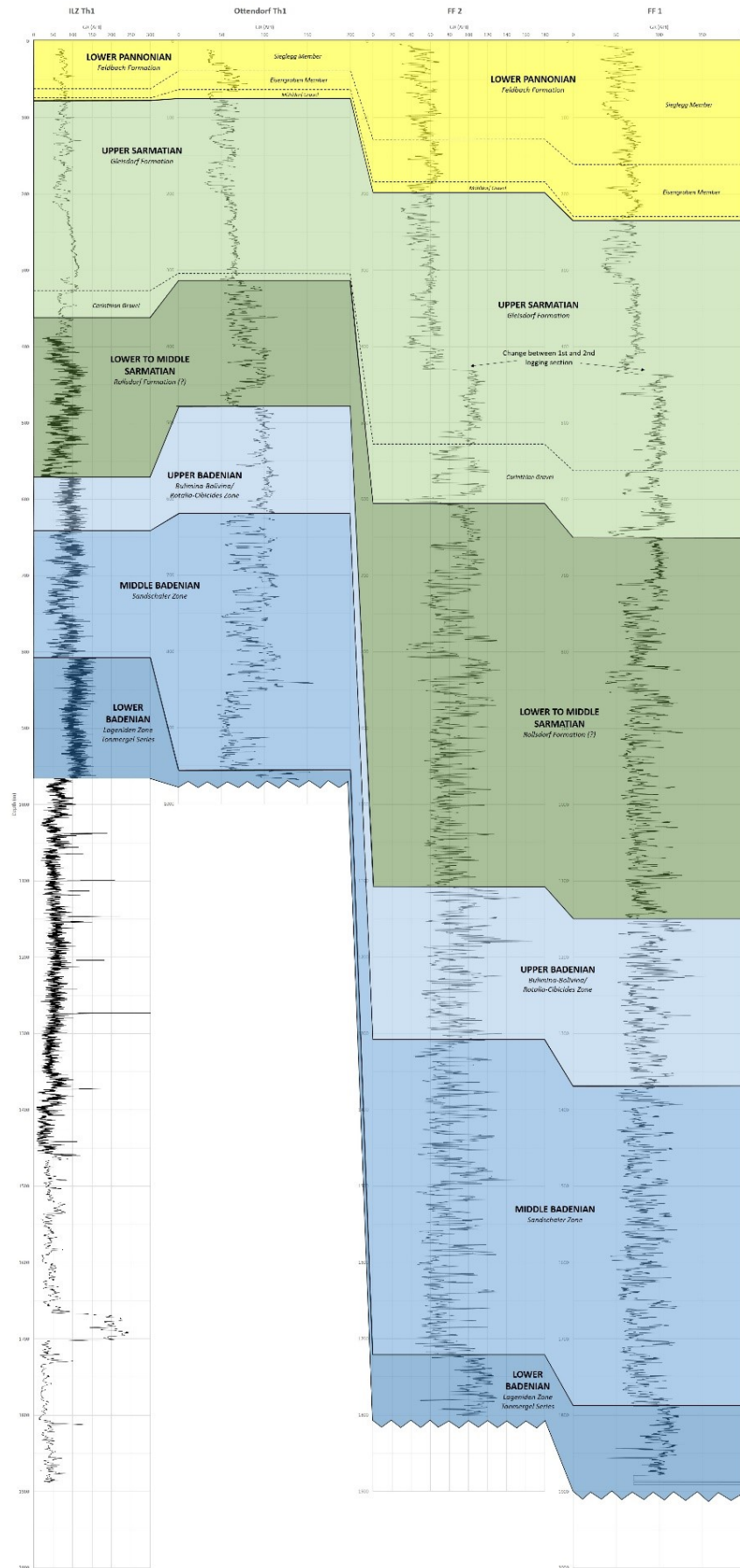
Fig. 6.1: Correlation of GR-logs between ILZ Thermal 1, Ottendorf Thermal 1, FF 1 and FF 2 from the Middle Badenian upwards, for introduction of ILZ Thermal 1 into regional geology (data from Geoteam Ges.m.b.H.).

However, the whole Badenian succession can be assigned to that what was termed as "marl, silt/sand, gravel" by Piller et al. (2004).

Sarmatian

After a sea level lowstand and erosional phase at the Badenian/Sarmatian boundary, Lower Sarmatian sediments start with the intercalation of coarse sandy and fine-grained sediments, whereas cylinder shape of the GR indicates a beach sand environment. From that upward, the whole Lower to Middle Sarmatian is dominated by an oscillating sea level indicated by deposition of fine-grained to coarse sediments in overall shallow marine conditions (Ebner & Sachsenhofer, 1995). If this succession can be correlated with the Rollsdorf or the Grafendorf Formation as described by Krainer (1984; 1987) or if it should be termed separately, remains elusive.

Nevertheless, the Lower to Middle Sarmatian succession is terminated by a 32.7 m thick sand/gravel package which can definitely be assigned to the "Carinthian Gravel" deposited from fluvial environment due to a marine regression (Winkler, 1927; Skala, 1967). The Upper Sarmatian starts with a large coarsening upward cycle, terminated by an oolitic horizon, which is also observable very well in the other wells and hence was used as a marker for correlation. Cycles like this, but in a smaller extent, dominate the Upper Sarmatian indicating a strongly fluctuating sea level and are summarized in the "Gleisdorf Formation" (Friebe, 1994). Coaly strata occur throughout the Sarmatian especially in fine-grained horizons separating coarse gravels and sands.

Pannonian

The base of Pannonian sediments is formed by a 3 m thick sand/gravel horizon, which can be correlated with the "Mühldorf Gravel" and also is well visible in the GR-logs of the other wells. This gravel is overlain by a dominantly pelitic succession with coal assigned to the limnic-brackish "Eisengraben Member", which in turn is overlain by a succession of dominantly shale, silt and sand with coal seams forming the limnic-deltaic "Sieglegg Member", both part of the "Feldbach Formation" (Gross, 2000; 2003).

6.2 Hydrogeological and Geothermal Interpretation

For the identification of potential water-bearing horizons, geophysical well logging measurements were used. Therefore, straight forward trends of logs defining water-bearing horizons are a decrease in gamma activity, a decrease in the SP-log and the splitting of shallow and deep resistivity.

Furthermore, horizons until the top of the Badenian (571.6 m) were declared as potential horizons for drinking water, whereas depths of more than 300 m are very rare for drinking water exploration.

Water-bearing horizons starting from the Sandschaler Zone (637.4 m), on the other side, were declared as potential deep-seated aquifers for thermal water exploration and utilization.

6.2.1 Drinking Water Potential

Based geophysical logging measurements, 10 aquifers for drinking water potential were identified until a depth of 571.6 m, whereas aquifers with thicknesses of < 2 m were not considered in Tab. 6.2 (Appendix A).

Horizon N°	Depth (m)	Net thickness (m)	Lithology	Porosity (%)
1	48.0 - 52.1	4.1	Sand	22.6
2	76.2-78.5	2.3	Gravel/Sand	21.7
3	133.4-135.7	2.3	Sand	22.6
4	150.0-155.7	5.7	Sand/Gravel	21.1
5	184.2-193.8 199.7-204.6 209.5-212.4	17.4	Sand/Gravel	21.2
6	308.6-318.6	10.0	Shaly sand	22.8
7	330.0-417.3	60.3	Gravel/Sand	20.8
8	466.6-476.5	9.9	Sand/Silt	30.4
9	491.1-515.9	24.8	Sand/Silt	31.9
10	546.6-549.5 552.3-556.6 559.4-564.3 566.7-571.6	17.0	Sand	28.3

Tab. 6.2: Potential aquifers for drinking water exploration in the well ILZ Thermal 1. Porosities are calculated after Archie (1942). See also section 5.1 and appendix A.

Those 10 aquifers with a total net thickness of 153.8 m were identified showing drinking water potential, whereas aquifers below 300-350 m are thought to be too deep for economic drinking water production. Therefore, the most interesting aquifers are especially those which lie above the Upper Sarmatian large coarsening upward sequence (< 212.4 m; aquifers 1-5) and maybe to a certain degree the aquifers of the "Carinthian Gravel" (308.6-362.7 m; aquifers 6 and partly 7). Archie (1942) porosities of deeper horizons of up to 32% are thought to be overestimated because of higher shale content and might lie in the same range as upper horizons.

6.2.2 Potential for Geothermal Energy

Major sequences for the utilization of geothermal waters are in the lower part of the Sandschaler Zone, the Base Conglomerate of the Lageniden Zone, the Karpatian Conglomerate-rich Group and in the Paleozoic Basement.

From all reservoirs, the Sandschaler Zone, although with lowest temperatures, is probably the one with highest potential for geothermal utilization due to water characteristics. Production of the waters from the Lageniden Zone and from the Paleozoic basement would require special treatment because of very high mineralization with a content of total dissolved solids of up to 18 g/l and a very high CO_2 content.

Nevertheless, a transmissivity of $3.15*10^{-6}$ m²/s (Tab. 6.3; Eisner & Goldbrunner, 2000) in the Sandschaler Zone is by a magnitude lower than most of the other reservoirs in the Lageniden Zone, the Karpatian and in the basement and already mentioned, temperature is also far lower with about 42-46.5°C.

The "Base Conglomerate" of the Lageniden Zone and the Karpatian "Conglomerate-rich Group" show very similar reservoir characteristics, both consisting of coarse conglomerates and sandstones regarding lithology with porosities ranging between 11 and 15 % (Tab. 6.3). Transmissivity was determined by Eisner & Goldbrunner (2000) only for the Lageniden Zone with $6.61*10^{-5}$ m²/s, what is thought to be similar in the Karpatian. Temperatures in those reservoirs reach 54°C at the top of the Lageniden Zone and up to 76.5°C at the base of the Karpatian (1,240.0 m).

The Paleozoic basement is more complex in terms of identifying potential geothermal reservoir zones because of the development of several lithofacies with different reservoir characteristics. In Tab. 6.3,

a compilation of all lithofacies is shown, trying to summarize those to four different facies based on color impression, grain size and grain habitus:

- Light (to medium) gray, fine-grained dolomites with splintered habitus (often rich in clay/marl)
- Medium gray, fine- to medium-grained dolomites with splintered or granular habitus
- Dark gray, coarse dolomites with granular habitus
- Very dark gray to black and very coarse dolomites with granular habitus

Stratigraphy		Depth [m]	Net thickness [m]		Lithology	Geophysics		Temperature [°C]	Porosity [%]	Hydraulic Conductivity [m/s]	Permeability [mD]	Transmissivity [m²/s]
						PE [b/e]	Density [g/cm³]					
Neogene	Sandschaler Zone	707.6 - 807.3	47.3		Intercalation of coarse to fine sandstones with fine silty to shaly sandstones and marls	n.a.	n.a.	42-46.5	22-25	n.a.	n.a.	$3.15*10^{-5}$
	Lageniden Zone/ Base Conglomerate	973.9 - 1,240.0	199.3		Coarse sandstones to conglomerates with thin silty to shaly intercalations decreasing towards the base	n.a.	n.a.	54-66.1	11-15	n.a.	n.a.	$6.61*10^{-5}$
	Karpatian	1,240.0 - 1,466.0	186.3		Coarse sandstones to conglomerates with few thin silty to shaly intercalations	n.a.	n.a.	66.1-76.5	15	n.a.	n.a.	n.a.
Graz Paleozoic	Upper light to dark grey dolomites and marls	1,466.0 - 1,475.0	9		Light to medium gray dolomites with subordinate red limestone, marl and crystalline components	2.62	2.48	76.7	10.2	$4.09*10^{-6}$	136.7	$3.7*10^{-5}$
		1,475.0 - 1,500.0	25		Light gray, finer, splintered dolomites with coarse marl grains and pyrite	2.98	2.74	76.9-78.0	5.5	$3.16*10^{-6}$	104.4	$7.3*10^{-5}$
		1,500.0 - 1,516.0	16		Coarse, medium gray, granular dolomites with white calcites and breccias (dolomitic clasts in marly ground mass)	2.96	2.73	78.4	5.9	$1.36*10^{-6}$	44.4	$2.2*10^{-5}$
		1,516.0 - 1,520.0	4		Coarse, dark grey dolomites with breccias and marl/clay containing rutile; greenish color impression	2.96	2.73	78.8	5.9	$3.60*10^{-7}$	11.7	$1.4*10^{-6}$
		1,520.0 - 1,552.5	32.5		Medium gray, splintered and granular dolomites with pyrite; very fine, greenish horizon at 1,540.0 with splintered dolomites and high clay content	3.00	2.72	79.0-80.4	6.2	$8.17*10^{-7}$	26.0	$2.6*10^{-5}$
		1,552.5 - 1,575.0	22.5		Coarse, very dark, granular, clean dolomites with calcite joints	3.08	2.79	80.4-81.5	4.3	$1.44*10^{-6}$	45.3	$3.24*10^{-5}$
		1,575.0 - 1,595.0	20		Medium to coarse grained, medium gray, splintered and granular dolomites with breccias; black to greenish splintered horizon at 1,582.5 containing pyrite and rutile similar to 1,540 and 1,516-1,520	3.18	2.80	81.5-82.4	3.8	$1.81*10^{-6}$	55.9	$3.62*10^{-5}$
		1,595.0 - 1,602.5	7.5		Coarse, medium gray, granular dolomites with breccias	3.10	2.78	82.6	5.0	$2.00*10^{-6}$	61.2	$1.50*10^{-5}$
		1,602.5 - 1,645.0	42.5		Very coarse, very dark, clean, granular dolomites with calcite joints	3.01	2.78	82.7-84.6	4.8	$1.71*10^{-6}$	51.7	$7.27*10^{-5}$
		1,645.0 - 1,665.0	20		Fine-grained, light gray, splintered dolomites with clay/marl containing pyrite and rutile	2.98	2.78	84.6-85.6	4.8	$1.48*10^{-6}$	43.8	$2.96*10^{-5}$
	Phyllitic/faulted Zone	1,665.0 - 1,670.0	5		Fine-grained, light gray, splintered and granular dolomites with abundance of clay/marl and crystalline components (mica, feldspar, quartz) containing pyrite and rutile	3.17	2.68	85.7	8.4	$1.20*10^{-6}$	35.2	$6.00*10^{-6}$
		1,670.0 - 1,682.0	12		Fine-grained, light gray, splintered and granular dolomites with abundance of clay/marl and crystalline components (mica, feldspar, quartz) containing pyrite and rutile; coarse, medium gray dolomites at 1,672.5 m	3.80	2.64	86.1	2.8	$6.23*10^{-8}$	1.9	$7.48*10^{-7}$
		1,682.0 - 1,702.0	20		Medium gray dolomites, coarser with very high abundance of crystalline components containing pyrite and rutile	3.83	2.67	86.3-87.2	2.2	$9.15*10^{-6}$	263.1	$1.83*10^{-4}$
	Lower dark gray dolomites	1,702.0 - 1,737.5	35.5		Very fine, light gray, splintered dolomites with probably high clay/marl content	3.11	2.81	87.2-88.8	3.4	$9.08*10^{-7}$	25.6	$3.22*10^{-5}$
		1,737.5 - 1,790.0	52.5		Coarse, dark gray, granular, clean dolomites with increasing brecciated components	3.15	2.82	88.8-91.2	3	$1.71*10^{-6}$	46.7	$8.95*10^{-5}$
		1,790.0 - 1,795.0	5		Coarse, medium gray, granular, dolomites with high content of breccias	2.85	2.82	91.4	3.6	$6.40*10^{-7}$	19.5	$3.20*10^{-6}$
		1,795.0 - 1,855.0	60		Coarse, medium to dark gray, granular dolomites with high breccia content	3.07	2.81	91.5-94.2	3.5	$1.21*10^{-6}$	32.2	$7.26*10^{-5}$
		1,855.0 - 1,906.0	51		Coarse, dark gray, granular, clean dolomites with high breccia content	2.98	2.80	94.2-96.5	3.6	$5.79*10^{-7}$	14.9	$2.95*10^{-5}$

Tab. 6.3: Summarizing table showing geothermal aquifer potential of the Neogene sequences (Sandschaler Zone, Lageniden Zone and Karpatian) and of the Paleozoic basement with net thicknesses, lithological descriptions, geophysical data and amongst all, hydrogeological and reservoir characteristics.

Concerning hydrogeological characteristics, total porosity (including intergranular porosity) is shown but also hydraulic conductivities calculated from fracture porosities representing effective porosity. Additionally, formation permeability was tried to calculate for better interpretation using the following equation:

$$\kappa = k * \frac{\eta}{\rho * g}$$

Where: κ = permeability (m²)

k = hydraulic conductivity (m/s)

η = dynamic viscosity of water (Pa s)

ρ = density of water (kg/m³)

g = gravitational acceleration = 9.81 m²/s

Dynamic viscosity is temperature dependent and was estimated using the Andrade-equation (Raman, 1923; Andrade, 1934):

$$\eta \ (Pa \ s) = A * e^{b/T}$$

Where: A, b = empirical constants (A = 9.64*10^{-4} Pa s; b = 2036.8 K
T = absolute temperature (K)

For getting the permeability in mD, the simple conversion 1 D ≈ 10^{-12} m² was used.

Results reveal, that most promising horizons for geothermal production are especially in the upper part of the basement in the light to medium gray dolomites between 1,466 and 1,500 m with permeabilities over 100 mD and temperatures of up to 78°C. A second potential zone occurs between 1,575 and 1,645 m in medium to very dark gray, clean dolomites comprising permeabilites between 50 and 60 mD and total porosities of up to 5 %. Temperature here already reach nearly 85°C.

High total porosity zones occur between 1,520 and 1,552.5 m with 6.2 % and at the transition from the phyllitic/faulted zone to the upper zone from 1,665-1,670 m with even 8.4 %. Both zones show generally low permeabilities and transmissivities compared to the other zones and therefore are interpreted to be characterized by high contribution of intergranular porosity and probably also clay/marl content.

Probably the most promising horizon is the fault zone itself from 1,682-1,702 m with a permeability of 263.1 mD and an expected temperature of around 87°C. Therefore, the fault zone also represents the major structure in the subsurface permitting fluid flow and contributing to convective heat transport.

The lower dark dolomites of the Schöckl Facies show a homogeneous development at all with lower permeabilities between 20 and 46 mD and porosities of 3.0 to 3.6 % and therefore are not interpreted as major reservoirs.

7   Conclusions and Discussion

The well ILZ Thermal 1, located on the western margin of the Fürstenfeld subbasin of the Eastern Styrian Neogene Basin, was drilled until a final depth of 1,906.0 m perforating Miocene sediments as basin fill until 1,466.0 m and dolomites of the Graz Paleozoic as basement until final depth. A summarizing litho-stratigraphic chart with net thicknesses and regional geological correlation is shown in Tab. 7.1.

	Litho-stratigraphy	Depth	Net thickness
	Pannonian	**0 – 79 m**	**79 m**
	Lower Pannonian		
	Feldbach-Formation	- 76 m	76 m
	Sieglegg-Member	- 65 m	65 m
	Eisengraben-Member	65 – 76 m	11 m
	Mühldorf Gravel	76 – 79 m	3 m
	Sarmatian	**79 – 571.6 m**	**492.6 m**
	Upper Sarmatian		
	Gleisdorf-Formation	79 – 330 m	251 m
	Carinthian Gravel	330 – 362.7 m	32.7 m
	Lower to Middle Sarmatian		
	Rollsdorf-Formation (?)	362.7 – 571.6 m	208.9 m
	--Transgression --		
	Badenian	**571.6 – 1,240 m**	**668.4 m**
	Upper Badenian		
	Bulimina-Bolivina/		
	Rotalia-Cibicdes Zone	571.6 – 637.4 m	65.8 m
	Middle Badenian		
	Sandschaler Zone	637.4 – 807.3 m	169.9 m
	Lower Badenian		
	Lageniden Zone		
	Tonmergel Series	807.3 – 966.1 m	158.8 m
	Base Conglomerate	966.1 – 1,240 m	273.9 m
	--- Transgression – Styrian Unconformity ------------------------------------		
	Karpatian	**1,240 – 1,466 m**	**226 m**
	Conglomerate-rich Group		
	--Transgression --		
	Rannach Facies	**1,466 – 1,668 m**	**202 m**
	Upper light to dark gray dolomites and marls		
	Phyllitic/faulted Zone	**1,668 – 1,702 m**	**34 m**
	Schöckl Facies	**1,702 – 1,906 m (F.D.)**	**204 m**
	Lower dark gray dolomites		

Tab. 7.1: Summarizing litho-stratigraphic table with depths and net thicknesses of formations in the well ILZ Thermal 1 (F.D.=Final Depth).

The Neogene sedimentary basin fill comprises depositions from the Lower Pannonian until Karpatian. In the Lower Pannonian "Feldbach-Formation" shaly sands dominate with minor shale as well as coarse sand to gravel intercalations. A 3 m thick coarse gravel horizon (76-79 m; "Mühldorf Gravel") forms the transition to the Sarmatian. Sarmatian deposits are characterized by an interlayering of shales to shaly sands and coarse sands to gravels, which is an expression of a highly oscillating Sarmatian sea level indicated by distinctive bell- and egg-shaped pattern of the GR-log. The only interruption of those cycles is the 32.7 m thick "Carinthian Gravel" (330-362.7 m) separating Upper Sarmatian from Lower to Middle Sarmatian sediments. Due to regional considerations, the Upper Sarmatian can be assigned to the "Feldbach-Formation", whereas the Lower to Middle Sarmatian maybe to the "Rollsdorf-" or "Grafendorf-Formation" strictly following the stratigraphic chart of Piller et al. (2004). But to clarify this question, further lithological investigations and comparisons with outcrops or similar successions of other wells are necessary. Minor oolites and coal seams also occur throughout the Sarmatian succession.

Several potential water-bearing horizons were identified for drinking water supply within the Lower Pannonian and Sarmatian with a total net thickness of 153.8 m. Most promising horizons are thick and clean sand/gravel packages with porosities ranging between 19-22%.

The Badenian succession consists of four formations starting with the Bulimina-Bolivina/Rotalia-Cibicides Zone showing a finer development comprising shales and marls, siltstones and shaly sands. This zone is interpreted as a major impermeable horizon separating Lower Pannonian and Sarmatian aquifers from Middle Badenian aquifers of the Sandschaler Zone underlying the BB/RC-Zone. The Sandschaler Zone shows a much coarser development of coarse sandstones with porosities ranging between 22-25% and minor fine, shaly intercalations. Transmissivity was determined to $3.15*10^{-6}$ m²/s (Eisner & Goldbrunner, 2000). The geothermal gradient within the well was calculated to be 45.5°C/km from measured water temperatures and is thought to be representative for the immediate area. Hence, temperatures reach 46.5°C in the lowest parts (about 800 m) and therefore this zone already shows a certain potential for geothermal energy production as a "very" low enthalpy resource with possible applications in balneology, snow melting, heat pumps, green houses, soil warming, fish farming, food processing amongst others after the Lindal-Diagram (see section 2.4). Total heat in place was estimated to $2.7*10^{8}$ MJ and water was classified as sodium-bicarbonate water after the PIPER-diagram with a content of TDS of 5.01 g/l.

The Sandschaler Zone is underlain by the shale- and marl-dominated "Tonmergel Series", part of the Lower Badenian "Lageniden Zone". Due to this development, this zone again is interpreted as an impermeable zone separating the aquifers from the "Sandschaler Zone" from the underlying "Base Conglomerate" and Karpatian "Conglomerate-rich Group". Both are characterized by a more or less homogeneous very coarse, conglomeratic development with minor shaly to marly intercalations and therefore can be seen as one aquifer. Porosities are also pretty homogeneous ranging between 11-15% throughout and transmissivity was determined to $6.61*10^{-5}$ m²/s. A major difference to the water of the Sandschaler Zone is water mineralization: With a content of TDS of 17.9 g/l, the waters from the Lageniden Zone and probably also from the Karpatian are much higher mineralized and can be classified as sodium-chloride-bicarbonate water. Additionally, a very high CO_2- and [226]Ra-content might lead to problems in production and especially utilization, unless treated specially what would produce additional costs. However, temperatures are around 54°C at the top of the "Base Conglomerate" (970 m) and reach 76.5°C at the base of the Karpatian (1,466 m). This temperature range, still in the area of a low enthalpy resource, allows applications in domestic hot water supply, green houses, radiators, snow melting, sludge digestion, wool washing amongst others. Total heat in place for the "Base Conglomerate" and the Karpatian was estimated to $4.78*10^{9}$ MJ.

Finally, the basement underlying the Neogene sedimentary basin fill can be assigned to the Graz Paleozoic due to the dolomitic development throughout. The thickness cannot be estimated, because the well ends at a depth of 1,906 m in those dolomites. It is suggested, that those are underlain by an Austro-Alpine crystalline basement but further investigations, e.g. seismics, deeper exploration wells,

could reveal the answer to this question. Nevertheless, the dolomitic basement of the well ILZ Thermal 1 can be subdivided into three successions:

    i)   Upper light to dark gray dolomites and marls – Rannach Facies
    ii)   Phyllitic/faulted zone
    iii)   Lower dark gray, brecciated dolomites – Schöckl Facies

The upper succession shows a very heterogeneous development consisting of light to dark gray, fine to coarse, marly to clean dolomites. Marl and clay mineral (mainly illite containing rutile as accessory phase) content generally is higher in light, fine-grained dolomites. Abundance of pyrite throughout the basement suggests deposition in an euxinic environment. Due to this development, the upper succession can be correlated with the Dolomite Member of the Dolomite-Sandstone-Series of Flügel & Neubauer (1984) or with the Treffenberg Subformation of the Flösserkogel Formation of the Rannach Facies using the newer classification of Flügel & Hubmann (2000) and Hubmann & Messner (2007). This interpretation reveals the age of those dolomites to Lower to Middle Devonian and deposition in a peritidal facies (Fenninger & Holzer, 1978).

Regarding geothermal potential, the same problem as in the Lageniden Zone with a very high water mineralization of 17.6 g/l TDS and a very high CO_2- and ^{226}Ra-content is present. The Paleozoic waters, in contrast, are classified as sodium-bicarbonate waters. Nevertheless, highest permeabilities are reached in the uppermost part with > 100 mD and around 1,600 m with 60 mD, what represent the most promising horizons. Temperatures there reach 76-83°C and total heat in place was estimated to $1.8 \ast 10^9$ MJ permitting application in chemical extraction, food processing, green houses, radiators amongst others.

The lower succession, in contrast, shows a much more homogeneous development consisting of dark gray, coarse dolomites with brecciated components increasing towards the base, i.e. the final depth of the well. Therefore, a stratigraphic change is proposed and correlation of those dolomites with the dark, brecciated dolomites of the Schöckl Facies described in the well Arnwiesen 1 by Ebner (1988) seems possible. A further correlation with the Raasberg or Schönberg Formation can only be suggested based on lithological descriptions in Ebner et al. (2001).

Concerning geothermal potential, the lower zone is also developed very homogeneously in terms of hydraulic conductivity/permeability with values ranging between 20-46 mD, what is considered to be too low for economic production and therefore is not regarded as a potential geothermal aquifer. Total heat in place, however is $3.1 \ast 10^9$ MJ and temperatures reach 96.5°C in the lowermost part what would already be suitable for application in a binary power plant for electricity production.

The upper and the lower successions are separated by a phyllitic and faulted zone indicated by very high gamma activity, whereas the major fault stretches from 1,682-1,702 m as indicated by microscopic cuttings and hydrogeological analyses. Within the fault, crystalline mineral phases such as mica, feldspar and quartz as shown in thin sections and XRD are highly abundant and are thought to have been introduced from a crystalline basement below. High fracture porosity and subsequent hydraulic conductivity/permeability of > 260 mD also defines the fault as a major pathway for fluid flow and hydrothermal activity.

References

Literature

Andrade, E. N. da C. (1934): A Theory of the Viscosity of Liquids. – Part I. London, Edinburgh and Dublin Philosophical Magazine and Journal of Sciences 17 (112), 497-511.

Archie, G. E. (1942): The electrical resistivity log as an aid in determining some reservoir characteristics. Journal of Petroleum Technology 5, 54-62.

Armstead, H. C. H. (1983): Geothermal Energy. E. & F. N. Spon, London, 404 p.

Arps, J. J. (1953): The effect of temperature on the density and electrical resistivity of sodium chloride solutions. Journal of Petroleum Technology 195, 17-20.

Asquith, G. & Krygowsik, D. (2004): Basic Well Log Analysis. Second Edition. AAPG Methods in Exploration Series 16, 244 p.

Axelsson, G. & Gunnlaugsson, E. (2000): Background: Geothermal utilization, management and monitoring. In: Long-term monitoring of high- and low enthalpy fields under exploitation. WGC 2000 Short Courses, Japan, 3-10.

Baker Atlas/Baker Hughes (1985): Log Interpretation Charts. Baker Hughes Inc., Houston, TX.

Balogh, K., Ebner, F. & Ravasz, C. (1994): K/Ar-Alter tertiärer Vulkanite der südöstlichen Steiermark und des südlichen Burgenlandes. In: Lobitzer, H., Csaszar, G. & Daurer, A. (eds.): Jubiläums-schrift 20 Jahre geologische Zusammenarbeit Österreich-Ungarn 2. Geologische Bundes-anstalt, Wien, 55-72.

Bear, J. (1993): Modeling Flow and Contaminant Transport in Fractured Rocks. In: *Bear, J., Tsang, C.-F. & Marsily, G. (eds.):* Flow and Contaminant Transport in Fractured Rock. 1-37.

Benderitter, Y & Cormy, G. (1990): Possible approach to geothermal research and relative costs. *In: Dickson, M. H. & Fanelli, M. (Eds.):* Small Geothermal Resources: A Guide to Development and Utilization. UNITAR, New York, 59-69.

Bertrani, R. (2015): Geothermal Power Generation in the World 2010-2014 Update Report. Proceedings World Geothermal Congress 2015, Melbourne, Australia, 19 p.

Boyeldieu, C. & Winchester, A. (1982): Use of the Dual Laterolog for the Evaluation of the Fracture Porosity in Hard Carbonate Formations. Offshore South East Asia Conference, Singapore, 1-11.

Brigaud, F., Vasseur, G. & Caillet, G. (1989): Use of well log data for predicting detailed in situ thermal conductivity profiles at well sites and estimation of lateral changes in main sedimentary units at basin scale. In: *Maury, V. & Fourmaintraux, D. (eds.):* Rock at Great Depth. Balkema, Rotterdam.

Brigaud, F., Vasseur, G. & Caillet, G. (1992): Thermal state in the north Viking Graben (North Sea) determined from oil exploration well data. Geophysics 57 (1), 69-88.

Bücker, C. & Rybach, L. (1996): A simple method to determine heat production from gamma-ray logs. Marine and Petroleum Geology 13 (4), 373-375.

Cermak, V. & Rybach, L. (1982): Thermal Properties. In: *Hellwege, K.-H. (ed.):* Landolt-Börnstein Numerical Data and Functional Relationships in Science and Technology, New Series, Group V. Geophysics and Space Research 1, Physical Properties of Rocks, subvol. A. Springer-Verlag, Berlin, 305-371.

Clauser, C. (2006): Geothermal Energy. In: *Heinloth, von K. (ed.):* Landolt-Börnstein Numerical Data and Functional Relationships in Science and Technology, New Series, Group VIII. Advanced Materials and Technologies 3, Energy Technologies, subvol. C: Renewable Energies. Springer-Verlag, Berlin, 493-604.

Clauser, C. & Huenges, E. (1995): Thermal conductivity of rocks and minerals. In: Rock Physics and Phase Relations – A Handbook of Physical Constants. AGU Reference Shelf 3, American Geohysical Union.

Clavier, C., Hoyle, W. R. & Meunier, D. (1971): Quantitative interpretation of thermal neutron decay time logs. Part 1. Fundamentals and techniques. Journal of Petroleum Technology 23, 743-755.

Craig, H. (1963): The isotopic geochemistry of water and carbon in geothermal areas. In: *Tongiogi, E. (Ed.):* Nuclear geology in geothermal areas. Spoleto, 17-53.

Dickson, M. & Fanelli, M. (2004): What is geothermal energy. Instituto di Geoscienze e Georisorse, CNR, Pisa, Italy.

Drever, J. I. (2005): Water, weathering, and soil. Elsevier, Oxford, UK, 626 p.

Duffield, W. A. & Sass, J. H. (2003): Geothermal Energy – Clean Power From the Earth's Heat. USGS Circular 1249, 36 p.

DVWK (1979): Empfehlungen zu Umfang, Inhalt und Genauigkeitsanforderungen bei chemischen Grundwasseruntersuchungen. DVWK-Regel 111, Hamburg, 6 p.

DVWK (1992): Entnahme und Untersuchungsumfang von Grundwasserproben. DVWK-Regel 128, Hamburg, 36 p.

Dziewonski, A. M. & Anderson, D. L. (1981): Preliminary reference Earth model. Physics of the Earth and Planetary Interiors, 25, 297-356.

Ebner, F. (1981): Vulkanische Tuffe im Miozän der Steiermark. Mitteilungen des Naturwissen-schaftlichen Vereines für Steiermark 111, 39-45.

Ebner, F. (1988): Das Paläozoikum in den RAG-Bohrungen Blumau 1, 1a und Arnwiesen 1 (Oststeirisches Tertiärbecken). Jahrbuch der Geologischen Bundesanstalt 131, 563-573.

Ebner, F. & Gräf, W. (1977): Die Bentonitvorkommen der Nordoststeiermark. Mitteilungen der Abteilung Geologie, Paläontologie und Bergbau am Landesmuseum Joanneum 38, 9-30.

Ebner, F. & Gräf, W. (1979): Bemerkungen zur Faziesverteilung im Badenien des Reiner Beckens. Mitteilungen der Abteilung Geologie, Paläontologie und Bergbau am Landesmuseum Joanneum 47, 11-17.

Ebner, F. & Gräf, W. (1982): Bentonite und Glastuffe der Steiermark. Archiv für Lagerstättenforschung der Geologischen Bundesanstalt 2, 31-45.

Ebner, F. & Sachsenhofer, R. F. (1991): Die Entwicklungsgeschichte des Steirischen Tertiärbeckens. Mitteilungen der Abteilung Geologischie und Paläontologie am Landesmuseum Joanneum 49, 1-96.

Ebner, F. & Sachsenhofer, R. F. (1995): Palaeogeography, subsidence and thermal history of the Neogene Styrian Basin (Pannonian basin system, Austria). Tectonophysics 242, 133-150.

Ebner, F., Fritz, H. & Hubmann, B. (2001): Das Grazer Paläozoikum: Ein Überblick. Bericht des Instituts für Geologie und Paläontologie der Karl-Franzens-Universität Graz 3, 34-58.

Ellis, A. J. & Mahon, W. A. J. (1967): Natural hydrothermal systems and experimental hot-water/rock interactions (Part II). Geochimica et Cosmochimica Acta 31, 519-538.

Fenninger, A. & Holzer, H.-L. (1978): Die Genese der Dolomit-Sandstein-Folge des Grazer Paläozoikums. Mitteilungen der Österreichischen Geologischen Gesellschaft 69, 109-162.

Flügel, H. W. & Neubauer, F. (1984): Steiermark – Erläuterungen zur Geologischen Karte der Steiermark 1:200.000. Geologische Bundesanstalt, Vienna, 127 p.

Flügel, H. W. (1988): Geologische Karte des prätertiären Untergrundes. In: *Kröll, A., Flügel, H. W., Seiberl, W., Weber, F., Walach, G. & Zych, D. (eds.):* Erläuterungen zu den Karten über den prätertiären Untergrund des Steirischen Beckens und der Südburgenländischen Schwelle. Geologische Bundesanstalt, Vienna, 21-49.

Flügel, H. & Hubmann, B. (2000): Das Paläozoikum von Graz: Stratigraphie und Bibliographie. Österreichische Akademie der Wissenschaften, Schriftenreihe der Erdwissenschaftlichen Kommune 13, 118.

Fournier, R. O. & Truesdell, A. H. (1973): An empirical Na-K-Ca geothermometer for natural waters. Geochimica et Cosmochimica Acta 37, 1255-1275.

Fournier, R. O., White, T. E. & Truesdell, A. H. (1974): Geochemical indicators of subsurface temperature – Part 1. Basic Assumptions. Journal of Research of the U.S. Geological Survey 2 (3), 259-262.

Fournier, R. O. (1977): Chemical geothermometers and mixing models for geothermal systems. Geothermics 5, 41-50.

Fournier, R. O. (1981): Application of water geochemistry to geothermal exploration and reservoir engineering. In: *Rybach, L. & Muffler, L. J. G. (Eds.):* Geothermal systems: principles and case histories. Wiley & Sons, New York, 109-143.

Fridleifsson, I. B. (2001): Geothermal energy for the benefit of the people. Renewable and Sustainable Energy Reviews 5, 299-312.

Friebe, J. G. (1990): Lithostratigraphische Neugliederung und Sedimentologie der Ablagerungen des Badeniens (Miozän) um die Mittelsteirische Schwelle (Steirisches Becken, Österreich). Jahrbuch der Geologischen Bundesanstalt 133 (2), Wien, 223-257.

Friebe, J. G. (1991): Neotektonik an der Mittelsteirischen Schwelle (Österreich): die „Steirische Phase". Zentralblatt für Geologie und Paläontologie, Teil I, 41-54.

Friebe, J. G. (1993): Sequence stratigraphy in a mixed carbonate-siliciclastic depositional system (Middle Miocene; Styrian Basin, Austria). Geologische Rundschau 82, 281-294.

Friebe, J. G. (1994): Gemischt siliziklastisch-karbonatische Abfolgen aus dem Oberen Sarmatium (Mittleres Miozän) des Steirischen Beckens. Jahrbuch der Geologischen Bundesanstalt 137 (2), 245-274.

Garg, S. K. & Combs, J. (2010): Appropriate use of USGS volumetric "Heat in Place" method and Monte Carlo calculations. Proceedings of 34th Workshop on Geothermal Reservoir Engineering, Stanford University, California, February 1-3, 2010.

Garg, S. K. & Combs, J. (2011): A reexamination of USGS volumetric "Heat in Place" method. Proceedings of 36th Workshop on Geothermal Reservoir Engineering, Stanford University, California, January 31 – February 2, 2011.

Garnish, J. D. (Ed., 1987): Proceedings of the first EEC/US Workshop on Geothermal Hot-Dry Rock Technology. Geothermics 16, 323-461.

Gasser, D., Stüwe, K. & Fritz, H. (2010): Internal structural geometry of the Paleozoic of Graz. International Journal of Earth Sciences (Geologische Rundschau) 99, 1067-1081.

Gegenhuber, N. (2013): Correlation of thermal conductivity and resistivity of carbonates from Austria. Austrian Journal of Earth Science 106 (2), 37-44.

Gegenhuber, N. & Schreilechner, M. (2014): Thermal Conductivity Log out of Correlation for Carbonates from Austria. 76th EAGE Conference & Exhibition 2014, Amsterdam RAI, The Netherlands.

Genser, J. & Neubauer, F. (1989): Low angle normal faults at the eastern margin of the Tauern Window (Eastern Alps). Mitteilungen der Österreichischen Geologischen Gesellschaft 81, 233-243.

Giggenbach, W. F. (1988): Geothermal solute equilibria. Derivation of Na-K-Mg-Ca geoindicators. Geochimica et Cosmochimica Acta 52, 2749-2765.

Goldbrunner, J. E. (1988): Tiefengrundwässer im Oberösterreichischen Molassebecken und im Steirischen Becken. Steirische Beiträge zur Hydrogeologie 39, 5-94.

Goldbrunner, J. E. & Zötl, J. (1993): Die Mineral- und Heilwässer Österreichs. Geologische Grundlagen und Spurenelemente. Springer-Verlag Wien New York, 324 p.

Goldbrunner, J. E. (1999): Hydrogeology of Deep Groundwaters in Austria. Mitteilungen der Österreichischen Geologischen Gesellschaft 92, 281-294.

Goldbrunner, J. E. (2015): Austria – Country Update. Proceedings World Geothermal Congress 2015, Melbourne, Australia, 13 p.

Goldbrunner, J. E., Kriegl, C. & Eisner, M. (2010): Die Geothermiebohrungen im Steirischen Becken. bbr-Sonderheft 2010, 2-9.

Gross, M. (1998): Faziesanalyse fluviatiler Sedimente (Obermiozän, Südoststeiermark, Österreich). Mitteilungen Geologie und Paläontologie am Landesmuseum Joanneum 56, 131-164, 367-371.

Gross, M. (2000): Das Pannonium im Oststeirischen Becken. Berichte des Institutes für Geologie und Paläontologie der Karl-Franzens-Universität Graz 2, 47-86.

Gross, M. (2003): Beitrag zur Lithostratigraphie des Oststeirischen Beckens (Neogen/Pannonium; Österreich). Österreichische Akademie der Wissenschaften, Schriftenreihe der Erdwissen-schaftlichen Kommissionen 16, 11-62.

Gross, M., Fritz, I., Piller, W. E., Soliman, A., Harzhauser, M., Hubmann, B., Moser, B., Scholger, R., Suttner, T. J. & Bojar H.-P. (2007): The Neogene of the Styrian Basin – Guide to Excursions. Joannea Geologie und Paläontologie 9, 117-193.

Gudmundsson, J. S. (1988): The elements of direct uses. Geothermics 17, 119-136.

Harzhauser, M. & Piller, W. E. (2004a): The Early Sarmatian – hidden seesaw changes. Courier Forschungsinstitut Senckenberg 246, 89-111.

Harzhauser, M. & Piller, W. E. (2004b): Integrated stratigraphy of the Sarmatian (Upper Middle Miocene) in the western Central Paratethys. Stratigraphy 1 (1), 65-86.

Harzhauser, M., *Daxner-Höck, G. & Piller, W. E. (2004):* An integrated stratigraphy of the Pannonian (late Miocene) in the Vienna Basin. Austrian Journal of Earth Sciences 95/96, 6-19.

Hochstein, M. P. (1990): Classification and assessment of geothermal resoures. In: *Dickson, M. & Fanelli, M. (Eds.):* Small Geothermal Resources: A Guide to Development and Utilization. UNITAR, New York, 31-57.

Hölting, B. & Coldewey, W. G. (2013): Hydrogeologie. Einführung in die Allgemeine und Angewandte Hydrogeologie (8. Auflage). Springer-Verlag, Berlin Heidelberg, 438 p.

Hubmann, B. & Messner, F. (2007): „Stein im Bild". Die fazielle Entwicklung der Rannachdecke (Grazer Paläozoikum). Jahrbuch der Geologischen Bundesanstalt 147 (1+2), 277-299.

Hurst, A. (1990): Natural gamma-ray spectrometry in hydrocarbon-bearing sandstones from the Norwegian Continental Shelf. Geological Society Special Publication 48, London, p. 211-222.

Hurter, S. & Schellschmidt, R. (2003): Atlas of geothermal resources in Europe. Geothermics 32, 779-787.

Jessop, A. M. (1990): Thermal Geophysics. Elsevier, Amsterdam.

John, H. (1999): Basics of Oil and Gas Log Analysis. Kansas Geological Survey, Doveton.

Kappelmeyer O. & Haenel, R. (1974): Geothermics with special reference to application. E. Schweizerbart Science Publishers, Stuttgart, 238 p.

Kazmer, M. (1990): Birth, life and death of the Pannonian Lake. Palaeogeography, Palaeoclimatology, Palaeoecology 79, 171-188.

Klut, H. & Olszewski, W. (1945): Untersuchungen des Wassers an Ort und Stelle, seine Beurteilung und Aufbereitung. 9. Auflage, Springer-Verlag Berlin, 281 S.

Kollmann, K. (1965): Jungtertiär im Steirischen Becken. Mitteilungen der Geologischen Gesellschaft in Wien 57, 2, 479-632.

Kosi, W., Sachsenhofer, R. F. & Schreilechner, M. G. (2003): High Resolution Sequence Stratigraphy of Upper Sarmatian and Pannonian Units in the Styrian Basin, Austria. Österreichische Akademie der Wissenschaften, Schriftenreihe der Erdwissenschaftlichen Kommissionen 16, 63-86.

Kovac, M., Barath, I., Harzhauser, M., Hlavaty, I. & Hudackova, I. (2004): Miocene depositional systems and sequence stratigraphy of the Vienna Basin. Courier Forschungsinstitut Senckenberg 246, Frankfurt am Main, 187-212.

Krainer, B. (1984): Zur zeitlichen Einstufung, Stratigraphie und Tektonik im Nordteil des Gleisdorfer Sarmatsporns (Oststeiermark). Mitteilungen des Naturwissenschaftlichen Vereines für Steiermark 114, 95-106.

Krainer, B. (1987a): Das Tertiär der Weizer Bucht, Steirisches Becken. PhD Thesis, University of Graz, 327 p.

Krainer, B. (1987b): Fluviatile Faziesentwicklung im Unterpannonien des steirischen Beckens (Zentrale Paratethys, Österreich). Facies 17, 141-148.

Kröll, A. (1988): Steirisches Becken-Südburgenländische Schwelle. Reliefkarte des prätertiären Untergrundes. Geologische Bundesanstalt, Vienna.

Kröll, A., Flügel, H. W., Seiberl, W., Weber, F., Walach, G. & Zych, D. (1988): Erläuterungen zu den Karten über den prätertiären Untergrund des Steirischen Beckens und der Südburgenländischen Schwelle. Geologische Bundesanstalt, Vienna, 49 p.

Landolt-Börnstein (1992): Numerical data and functional relationships in science and technology, Vol. 1 Physical properties of rocks. Springer-Verlag Berlin-Heidelberg-New York.

Larionov, V. V. (1969): Borehole Radiometry. Moscow, U.S.S.R., Nedra.

Lavigne, J. (1978): Les resources geothérmiques francaises – possibilités de mise en valeur. Annuales des Mines, 1-16.

Legmann, H. (2003): The Bad Blumau geothermal project: a low temperature, sustainable and environmentally benign power plant. Geothermics 32, 497-503.

Lindal, B. (1973): Industrial and other applications of geothermal energy. In: *Armstead, H. C. H. (ed.):* Geothermal Energy. UNESCO, Paris, 135-148.

Lucia, F. J. (1999): Carbonate Reservoir Characterization. Springer-Verlag, Berlin Heidelberg, 226 p.

Lund, J. W. & Boyd, T. L. (2015): Direct Utilization of Geothermal Energy 2015 Wolrdwide Review. Proceedings World Geothermal Congress 2015, Melbourne, Australia, 31 p.

Lunis, B. & Breckenridge, R. (1991): Environmental considerations. In: *Lienau, P. J. & Lunis, B. C. (eds.):* Geothermal Direct Use. Engineering and Design Guidebook. Geo-Heat Center, Klamath Falls, Oregon, 437-445.

Magyar, I., Geary, D. H. & Müller, P. (1999): Paleogeographic evolution of the Late Miocene Lake Pannon in Central Europe. Palaeogeography, Palaeoclimatology, Palaeoecology 147, 151-167.

Marini, L. (2000): Geochemical techniques for the exploration and exploitation of geothermal energy. Dipartimento per lo studio del Territorio e delle sue Risorse, Università degli Studi di Genova, Italy, 82 p.

Mburu, M. (2010): Geothermal Energy Utilisation. Short Course V on Exploration for Geothermal Energy 2010, Kenya, 1-11.

McCleskey, R. B., Nordstrom, D. K., Ryan, J. N. & Ball, J. W. (2012): A new method of calculating electrical conductivity with applications to natural waters. Geochimica et Cosmochimica Acta 77, 369-382.

Muffler, P. & Cataldi, R. (1978): Methods for regional assessment of geothermal resources. Geothermics 7, 53–89.

Neubauer, F. & Genser, J. (1990): Architektur und Kinematik der östlichen Zentralalpen – Eine Übersicht. Mitteilungen des Naturwissenschaftlichen Vereins Steiermark 120, 203-219.

Nicholson, K. (1993): Geothermal Fluids. Springer Verlag, Berlin, XVIII, 264 p.

Piller, W. E., Egger, H., Erhart, C. W., Gross, M., Harzhauser, M., Hubmann, B., van Husen, D., Krenmayer, H.-G., Krystyn, L., Lein, R., Lukeneder, A., Mandl, G. W., Rögl, F., Roetzel, R., Rupp, C., Schnabel, W., Schönlaub, H. P., Summesberger, H., Wagreich, M. & Wessely, G. (2004): Die stratigraphische Tabelle von Österreich (sedimentäre Schichtfolgen). Kommission für die paläontologische und stratigraphische Erforschung Österreichs der Österreichischen Akademie der Wissenschaften und Österreichische Stratigraphische Kommission, Vienna.

Piper, A. M. (1953): A graphic procedure in the geochemical interpretation of water analyses. USGS, Washington D.C., Ground water notes 12.

Polesny, H. (2003): The Karpatian in the Styrian Basin. In: Brzobohatý, R. & Adámek, J. (eds.): The Karpatian (A lower Miocene stage of the central Paratethys). Masaryk University, Brno, 360 p.

Pollack, H. N., Hurter, S. J. & Johnson, J. R. (1993): Heat flow from the earth's interior: analysis of the global data set. Reviews of Geophysics 31 (3), 267–280.

Raman, C. V. (1923): A Theory of the viscosity of liquids. Nature 111, 532-533.

Ratschbacher, L., Merle, O., Davy, Ph. & Cobbold, P. (1991a): Lateral extrusion in the Eastern Alps, 1. Boundary conditions and experiments scaled for gravity. Tectonics 10, 245-256.

Ratschbacher, L., Frisch, W., Linzer, H.-G. & Merle, O. (1991b): Lateral extrusion in the Eastern Alps, 2. Structural analysis. Tectonics 10, 257-271.

Reyes, A. G. (1990): Petrology of Philippine geothermal system and the application of alteration mineralogy to their assessment. Journal of Volcanology and Geothermal Research 43, 279-304.

Rögl, F. (1998): Palaeogeographic Considerations for Mediterranean and Paratethys Seaways (Oligocene to Miocene). Annalen des Naturhistorischen Museums Wien 99, 279-310.

Rögl, F. (1999): Mediterranean and Paratethys. Facts and hypothesis of an Oligocene to Miocene paleogeography (short overview). Geologica Carpathica 50 (4), 339-349.

Rögl, F. & Steininger, F. F. (1984): Neogene Paratethys, Mediterranean and Indo-Pacific seaways. Implications for the paleobiogeography of marine and terrestrial biotas. In: *Brenchly, P. (ed.):* Fossils and Climate. Wiley, New York, 171-200.

Royden, L. H. (1988): Late Cenozoic tectonics of the Pannonian Basin System. In: Royden, L. H. & Horvath, F. (eds.): The Pannonian Basin. A Study in Basin Evolution. AAPG Memoirs 45, 27-48.

Rybach, L. (1986): Amount and significance of radioactive heat sources in sediments. In*: Burrus, E. J. (Ed.):* Thermal Modelling in Sedimentary Basins, Collections Colloques et Seminaires 44. Edition Technip, Paris.

Sacchi, M. & Horvath, F. (2002): Towards a new time scale for the Upper Miocene continental series of the Pannonian Basin (Central Paratethys). European Geosciences Union, Stephan Mueller Special Publication Series 3, 79-94.

Sachsenhofer, R. F. & Littke R. (1993): Characterization of organic matter in the Styrian basin (Austria, Pannonian basin system). In: *Oygard, K. (ed.):* Organic Geochemistry. Proceedings of the 16th International Meeting on Organic Geochemistry, Stavanger, 26-29.

Sachsenhofer, R. F., Sperl, H. & Wagini, A. (1996): Structure, development and hydrocarbon potential of the Styrian Basin (Pannonian Basin system, Austria). In: *Wessely, G. & Liebl, W. (eds.):* Oil and Gas in Alpidic Thrustbelts and Basins of Central and Eastern Europe. EAGE Special Publication 5, 393-414.

Sanner, B., Karytsas, C., Mendrinos, D. & Rybach, L. (2003): Current status of ground source heat pumps and underground thermal energy storage in Europe. Geothermics 32, 579-588.

Scheifinger, M., Eisner, M., Gross, M. & Hubmann, B. (1999): Die Thermalwasserbohrung Ilz 1 – Ein weiterer Einblick in die Füllungsgeschichte des Oststeirischen Beckens. Mitteilungen der Geologie- und Bergbaustudenten in Österreich 42, 220-221.

Schlumberger (1982): Natural Gamma Ray Spectrometry. Essentials of N.G.S. Interpretation.

Schlumberger (2000): Log Interpretation Charts. Schlumberger Ed. Serv.

Schön, J. (2004): Physical properties of rocks. Elsevier, 600 p.

Schön, J. H. (2011): Physical Properties of Rocks. A workbook. *In: Cubitt, J. (ed.):* Handbook of Petroleum Exploration and Production, Volume 8. Elsevier, Oxford, UK, 481 p.

Schmöller, R. (1991): Forschungsschwerpunkt Tiefenseismik. Berichte über eigenfinanzierte Projekte der Joanneum Research, Graz, 32-35.

Schreilechner, M. G. (2007): Hochauflösende Seismostratigraphie des Oststeirischen Beckens und der Senke von Weichselbaum unter besonderer Betrachtung der Hydrogeologie (Miozän, Österreich). PhD Thesis, University of Leoben, 154 p.

Shaogui, D., Xiaochang, W., Dejiang, Z., Yiren, F. & Zhen, Y. (2006): Interpreting Dual Laterolog Fracture Data in Fractured Carbonate Formation. Journal of China University of Geosciences 17 (2), 168-172.

Sibbit, A. M. & Faivre, O. (1985): The Dual Laterolog Response in Fractured Rocks. Trans., paper T, SPWLA 26th Annual Logging Symposium, 1-34.

Skala, W. (1967): Kurzbericht über die Untersuchung von Fließrichtungen in den Basisschottern des Obersarmats im Steirischen Becken. Mitteilungen des Naturwissenschaftlichen Vereines für Steiermark 97, 28-31.

Stacey, F. D. & Loper, D. E. (1988): Thermal history of the Earth: a corollary concerning non-linear mantle rheology. Physics of the Earth and Planetary Interiors 53, 167-174.

Stefansson V. & Fridleifsson, I. B. (1998): Geothermal energy European and worldwide perspective. Expert hearing on ''Assessments and Prospects for Geothermal Energy in Europe'' in the framework of Sub-Committee on Technology Policy and Energy of the Parliamentary Assembly of the Council of Europe, Strasbourg.

Stieber, S. J. (1970): Pulsed neutron capture log evaluation in the Louisiana Gulf Coast. Society of Petroleum Engineers, 47th Annual Meeting, paper SPE-2961.

Stiny, J. (1918): Die Lignite in der Umgebung von Feldbach in Steiermark. Bergbau und Hütte 10/11, 171-180, 193-196.

Stober, I. (1995): Die Wasserführung des kristallinen Grundgebirges. Ferdinand Enke Verlag, Stuttgart, 191 p.

Stober, I. & Bucher, K. (1999): Origin of salinity of deep groundwater in Crystalline rocks. Terra Nova 11 (4), 181-185.

Stober, I. & Bucher, K. (2012): Geothermie. Springer-Verlag, Heidelberg, 287 p.

Taylor, H. P. Jr. (1967): Oxygen isotope studies of hydrothermal mineral deposits. In: *Barnes, H. L. (Ed.):* Geochemistry of hydrothermal ore deposits. Holt, Rinehart and Winston, 670 p.

Tenzer, H. (2001): Development of hot dry rock technology. Bulletin Geo-Heat Center 32 (4), 14-22.

Turcotte, D. L. & Schubert, G. (2002): Geodynamics (2nd edition). Cambridge University Press, Cambrige, UK, 456 p.

Vacquier, V. (1991): The origin of terrestrial heat flow. Geophysical Journal International 106, 199-202.

Vasvári, V. (2011): On the applicability of Dual Laterolog for the determination of fracture parameters in hard rock aquifers. Austrian Journal of Earth Sciences 104 (2), 80-89.

Von Zabeltitz, C. (1986): Gewächshäuser: Planung und Bau. Handbuch des Erwerbsgärtners. E. Ulmer, Stuttgart, 284 p.

WEC (2013): World Energy Perspective. Cost of Energy Technologies. World Energy Council, London, 48 p.

White, D. E. (1973): Characteristics of geothermal resources. In: *Kruger, P. & Otte, C. (Eds.):* Geothermal Energy. Stanford University Press, Stanford, 69-94.

Winkler, A. (1927a): Erläuterungen zur geologischen Spezialkarte der Republik Österreich. Blatt Gleichenberg. Geologische Bundesanstalt, Wien, 164 p.

Winkler, A. (1927b): Über die sarmatischen und pontischen Ablagerungen im Südostteil des Steirischen Beckens. Jahrbuch der Geologischen Bundesanstalt 77, 393-456.

Winkler-Hermaden, A. & Rittler, W. (1949): Erhebungen über artesische Wasserbohrungen im steirischen Becken, unter Berücksichtigung ihrer Bedeutung für die Tertiärgeologie. Geologie und Bauwesen 17 (2-3), 33-96.

Winkler-Hermaden, A. (1957): Geologisches Kräftespiel und Landformung. Springer Verlag, Wien, 822 p.

Witherspoon, P. A., Wang, J. S. Y., Iwai, K. & Gale, J. E. (1980): Validity of cubic law for fluid flow in a deformable rock fracture. Water Resources Research 16 (6), 1016-1024.

Wyllie, M., R., J., Gregory, A. R. & Gardner, G. H. F. (1958): An experimental investigation of the factors affecting elastic wave velocities in porous media. Geophysics 23, 459-493.

Web sources

Aeschbach-Hertig, W.: Dichte des Wassers. http://www.iup.uni-heidelberg.de/institut/studium/lehre/AquaPhys/docMVEnv3_12/AqSysSkript_Kap2.pdf

GBA, 2016: https://www.geologie.ac.at/forschung-entwicklung/kartierung-landesaufnahme/energie/ geothermie/

ZAMG, 2015: https://www.zamg.ac.at/cms/de/klima/klimauebersichten/klimamittel-1971-2000

Unpublished references

Aguilera, F. (2014): Geotermía – Prospección Geoquímica. Lecture notes. Departamento de Geología, Universidad de Chile, Santiago de Chile, unpublished.

Arsenal Research (2000): Große Heilwasseranalyse für die Anerkennung als Heilquelle – Sonde Ilz Thermal 1. Arsenal Research unpublished report, 10 p.

Böchzelt, B. & Goldbrunner, J. E. (2000): Bohrungen Geothermie FF 1 und 2. Bohr- und Testphase – Abschlussbericht. Geoteam unpublished report, Gleisdorf, 34 p.

Eisner, M. & Goldbrunner, J. (1999): Sonde Ilz Thermal 1. Perforation höherliegender Horizonte – Hydraulische und hydrochemische Auswertung. Geoteam unpublished report, Gleisdorf.

Eisner, M. & Goldbrunner, J. (2000): Sonde Ilz Thermal 1. Hydrogeologisch-technischer Abschlussbericht. Geoteam unpublished report, Gleisdorf, 11 p.

Eisner, M. & Goldbrunner, J. E. (2003): Tiefbohrung Ottendorf Thermal 1. Geologisch-technischer Abschlussbericht. Geoteam unpublished report, Gleisdorf, 24 p.

Goldbrunner, J., Eisner, M., Scheifinger, M. & Vasvári, V. (2000): Pilotprojekt „Thermalbohrung Ilz". Wissenschaftliche Auswertung der geophysikalischen Bohrlochmessungen. Geoteam unpublished report, Gleisdorf, 25 p.

RAG (1965): Walkersdorf 1. Completionlog. Unpublished Report.

List of Figures

List of Tables